THE UNIVERSITY OF HULL

Liquid Crystals for Light Emitting Diodes

being a Thesis submitted for the Degree of

Doctor of Philosophy (PhD)

in the University of Hull

by

Alicia Liedtke, Dipl.-Ing. (FH)

May 2009

Abstract

In this work a series of new semiconducting liquid crystals (LCs), which are applicable for organic light emitting diodes (OLEDs), were investigated. Semiempirical calculations were carried out on monomers and anti-cofacial dimers built from our molecules, representing molecules in solution and thin film respectively. Compared to the monomer a doubling of the oscillator strength in the dimer was found for longitudinal offsets larger than 20 Å. Smaller shifts showed a forbidden absorption transition from ground to the lowest excited state. Assuming that the absorption transition is equivalent to the emissive transition, this might explain the reduced optical quantum efficiency observed for all of our materials in the solid state.

OLEDs made from blends of three different blue/green emitters with a red component showed white light emission with voltage independent CIE coordinates close to the ideal white. With polarised microscopy nematic phases frozen in a glassy state at room temperature were observed for all blends. Thus the blends were homogeneous and no phase separation occurred. This is important for homogeneous white emission and the alignment of the LCs due to a rubbed alignment layer below. Polarised white electroluminescence with an average polarisation ratio of 8:1 was shown from an OLED made with a blend deposited onto an alignment layer. Polarised background light for LC displays is desirable as this minimises the losses at the polarisers in the display and thus increases its brightness or lowers the power consumption. The low efficiency of the red emitter however limited the OLED performance.

Surface relief gratings (SRGs) with periods of a few hundred nm and a maximum depth of 66 nm and periods in the µm-range with a depth of 140 nm were spontaneously induced on our films. They were formed through molecular mass transport from the dark to bright regions during crosslinking by irradiation with a sinusoidal light pattern created by a phase mask. The anisotropic properties of LCs are shown to enhance transport. SRGs were formed at room temperature and an elevated sample temperature of 65°. They are suitable feedback structures for optically pumped organic lasers and can also be employed to enhance the outcoupling of OLEDs.

Acknowledgements

First of all I would like to thank Prof. Mary O'Neill for giving me the opportunity to carry out a PhD under her supervision at the University of Hull. Her advice, never ending enthusiasm and support concerning my research, as well as her participation in my personal life, cannot be valued enough.

I would like to thank my colleagues and the staff at the University of Hull for the wonderful working atmosphere and especially Gordon Sowersby, whose help and technical advice was most valuable. Prof. Pete Dyer I would like to thank for his advice and help with the phase mask simulations. I also would like to acknowledge the University of Hull for the financial support of my PhD thesis.
For the synthesis of the liquid crystals investigated in this work I would like to thank Panos Vlachos, Matthew P. Aldred, Anke Werthmöller, Adrian Fries and especially Stuart P. Kitney, who with Steve Kelly was a most inspiring participant in our group meetings.

I am grateful to the members of the Materia Nova research group and in particular David Beljonne, Jérôme Cornil and Bernard Van Averbeke for giving me the opportunity to carry out simulations on our molecules at their research facility in Mons, Belgium. Particularly I would like express my gratitude towards Bernard Van Averbeke, for his help conducting and evaluating the simulations.

To my parents I am deeply thankful to for encouraging me to follow my own path and for being always there to help and support me in every aspect of my life.

Finally I would like to thank my partner Stefan for his strength and support over the last years. His optimism and belief in me never failed to encourage me.

Table of Contents

1 Introduction

Organic semiconductors have become a matter of great interest over the last years as they offer several advantages to conventional semiconductors. They are first of all cheaper to synthesize, can be applied to flexible substrates, are extremely thin with film thicknesses of less than 1 μm, have low power consumption and offer band gap tailoring. This makes them highly suitable for portable devices. Two types of organic semiconductors are mainly investigated, polymers and small molecules. The latter is applied by vacuum deposition, which allows only a limited substrate size and is also much more expensive than solution processing.[1] Polymers are solution processable so that the coating of large substrates with cheap application techniques like ink-jet printing and spin coating is realisable.[2] The cathode however still needs to be applied by vacuum deposition so that the substrate size is still limited and flexible substrates might get damaged due to the high temperatures. Organic semiconductors have found their first application as OLEDs in commercial devices like mobile phones and MP3 player displays. The field of application for organic semiconductors is large, for example they also can be used for transistor and solar cells. This work deals with liquid crystals for light emitting diodes.

LEDs made from inorganic semiconductors are now available for the most important colours red, green and blue, so that even white light for room lighting and background sources in LC displays (LCDs) is realisable through colour mixing. Inorganic semiconductors however are expensive in production compared to e.g. fluorescence tubes so that their low power consumption does not make up for the higher price.[3] White OLEDs (WOLEDs) are a cheap potential alternative. They also offer the possibility to create polarised emission, which is especially useful for the background light in LCDs since the loss at the polarisers is minimised and thus the power consumption reduced. Organic layers are also patternable for example by photolithography or corrugated layers below. Patterned structures can be used as feedback structures for laser emission or to enhance the outcoupling efficiency.[4] Through extensive research for example on the device layout OLED performance has

improved over the last years, but the best device structure is useless if charge transport in the organic material is low. It has therefore become more and more of interest to investigate the intra- and intermolecular interactions by quantum mechanical means.

The University of Hull is well known for its research in liquid crystals (LCs). Our approach to organic semiconductors is to incorporate a semiconducting and emissive core in the liquid crystal molecules. Typical liquid crystal properties like parallel alignment of the molecules in the nematic phase are maintained so that polarised emission is obtainable when the films are deposited on an alignment layer. Crosslinkable end groups are attached to the LCs so that a LC polymer network is formed when irradiated with ultra violet light. This renders the films insoluble so that multilayered devices are realisable. Using lasers as crosslinking sources also allows small feature pixelation. The alignment properties also ensure a higher order in the molecular arrangement, which can improve carrier mobility.[5]

In this work we model some of our semiconducting LCs in terms of their transition dipole densities between HOMO (highest occupied molecular orbital) and LUMO (lowest unoccupied molecular orbital), transition energies and oscillator strengths in a monomer. Semiempirical calculations using ZINDO (Zerner's intermediate neglect of differential overlap) coupled to a single configuration interaction (S.C.I.) scheme involving singly excited configurations, was performed on AM1 (Austin Model 1) optimised geometries. Two compounds are also modelled in a dimer configuration with longitudinal shift along the long axis to simulate the interaction of the molecules in nematic thin films and investigate the effect on the transition dipoles and energies as well as oscillator strengths. For the dimers the strength of different coupling interactions are computed with varying offset. The modelled results are placed into context with experimental results. The simulations were carried out under the supervision of David Beljonne, Bernard Van Averbeke and Jérôme Cornil at the Materia Nova research group from the the University of Mons-Hainaut, in Mons, Belgium. An introduction to the modelling of molecules and the experimental description are given in section 2.4 and 3.4 respectively. The results are presented and discussed in Chapter 4.

LCs form homogenous blends when mixed. This makes them suitable candidates to create white light by blending emitters of different colours with each other. We investigate three different blue/green emitters mixed with a red emitter to achieve white light emission. The blends are examined with respect to their transition temperatures and LC phases at room temperature with differential scanning calorimetry (DSC) and polarisation microscopy to ensure that a nematic order is maintained and no phase

separation occurs. OLEDs built from these blends are characterised in terms of their brightness, efficiency, CIE coordinates and I-V response. The blend with the best performance is then investigated for polarised electroluminescence through molecular alignment from a rubbed PEDOT layer below. An introduction to OLEDs and LCs is given in sections 2.1 and 2.2 respectively. The experimental description for DSC, polarisation microscopy and OLEDs production are given in Chapter 3. The results on the white OLEDs are presented and discussed in Chapter 5.

We also investigate whether surface relief gratings (SRGs) can be introduced on our LC films by exposing them with a sinusoidal light pattern created with an ultraviolet laser and a phase mask. Two phase masks of different periods are used and different film concentrations and sample temperatures are examined to optimise the gratings. The surface is scanned with an atomic force microscope (AFM) to measure the period and depth of the corrugation. The sinusoidal intensity patterns behind the mask are also modelled numerically and put into context with the experimental results. An introduction to grating applications and phase masks and information on exposure conditions and mask alignment can be found in section 2.6 and 3.5 respectively. The obtained SRG results are presented and discussed in Chapter 6.

Chapter 7 concludes with the most important results of this work as well as an outlook of possible future investigation.

The publications obtained during this work can be found in Chapter 8.[6, 7, 8, 9]

2 Background Theory

In this chapter an introduction to organic light emitting diodes and liquid crystals as well as the basic principles in molecular modelling, the origin of absorption and emission spectra, the techniques to create sinusoidal intensity patterns and the calculation of their grating periods is given.

2.1 Organic Light Emitting Diodes

An organic light emitting diode (OLED) is a light emitting device analogous to an inorganic semiconductor light emitting diode (LED) but made out of an organic material. The ability of organic materials to emit light was discovered in 1963 by Martin Pope et al.[10] but was not further pursued until 1987 when C.W. Tang and S.A. VanSlyke achieved a brightness of over 1000 cd/m^2 from an OLED.[11] Organic semiconductors are much cheaper and lighter than inorganic semiconductors (like gallium arsenide and germanium) and they offer the opportunity to be incorporated in flat panel or flexible displays as well as ambient light sources. The most researched organic materials are small molecules and polymers. Displays using the former are already commercially available e.g. in mobile phones like the BenQ-Siemens S88, the Nokia BH-902 and the Sony Ericsson Z610. Although the development of small molecules is beyond the development of polymers it is estimated that the latter will overtake the small molecules in the future. Small molecules are more expensive to work with since they have to be applied by vapour deposition under vacuum. This limits the display size and the possibility to use them for flexible displays since a flexible polymer substrate might be damaged during the deposition process due to the high temperatures occuring. Polymers can be dissolved in organic solvents like chloroform or toluene so that they are solution processable and can be applied to substrates by spin coating or ink-jet printing. This reduces fabrication costs and is a great advantage for the production of large area displays and also flexible displays.

Displays made out of OLEDs would have the advantage that they are active emissive displays. Conventional liquid crystal displays (LCDs) are passive and work with a background light source whose emission is either transmitted or blocked, see Chapter 2.2.4. The background light is always on so the power consumption is much higher than in active displays, where pixels can be switched on and off separately.

The development of OLEDs has now reached the stage, that they can be regarded as a real alternative to inorganic LEDs. A typical device structure is shown in Figure 2.1.

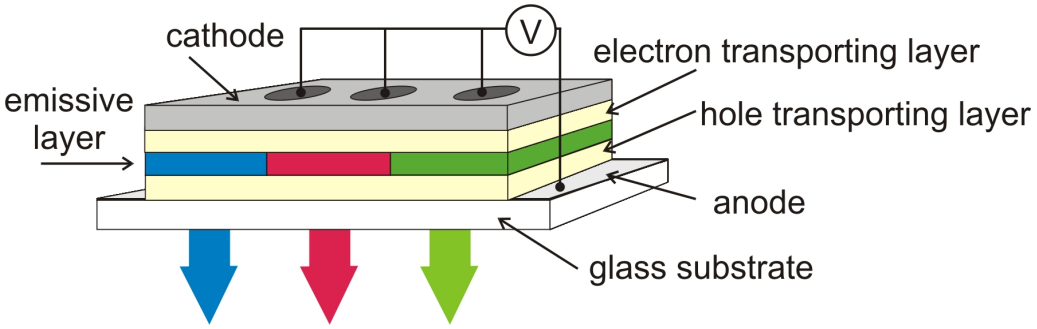

Figure 2.1: Typical OLED device structure.[12]

In most cases a glass slab coated with a transparent anode (typically indium tin oxide, ITO) is used as the substrate to begin with. The next layer is a hole (positive charge) transporting layer. Usually poly(3,4-ethylene-dioxythiophenene) also known as PEDOT is used. This layer protects the organic layer from the rough surface of the ITO, since spikes in the ITO surface can lead to short circuits. The hole transporting layer can also be used to balance the energy difference between the work function of the anode and the energy levels of the emissive layer (see Figure 2.2) to reduce the barriers for charge injection. The work function specifies the energy, which is needed to remove an electron from its atom to the vacuum level. Since ITO has a relatively low work function compared to the ionisation potential (IP) of many organics, the additional layer can reduce this barrier and therefore reduce the operational current. PEDOT can also work as an alignment layer, if it is rubbed before the organic layer is applied.[13] Different types of molecules can be used as emissive layer. Small molecules, main chain polymers or light emitting liquid crystals are available, although the latter class is still under development. The next layer is the electron (negative charge) transporting layer, which has the same function as the hole transporting layer; protection and reduction of the barriers to inject charges. In our case 1,3,5-tri(phenyl-2-benzimidazolyl)benzene (TPBI) is used for this application. A very thin layer of lithium fluoride (LiF) with a thicker layer of aluminium on top is used for the cathode. The presence of LiF lowers the workfunction of the cathode, which enhances charge injection on the cathode side.[14,

[15] The barrier E_e (Figure 2.2) that the electrons have to overcome is small if the workfunction $\Phi_{cathode}$ is low. The aluminium layer protects the organic materials below from air and also acts as a mirror to reflect the organic emission to enhance the amount of light coupled out. Where a voltage is applied an electric field builds up and positive and negative charges are injected. Due to the electric field the injected charges move from molecule to molecule by hopping conduction. If a positive and a negative charge meet they can form an exciton (bound electron-hole pair), which if it recombines can emit a photon.

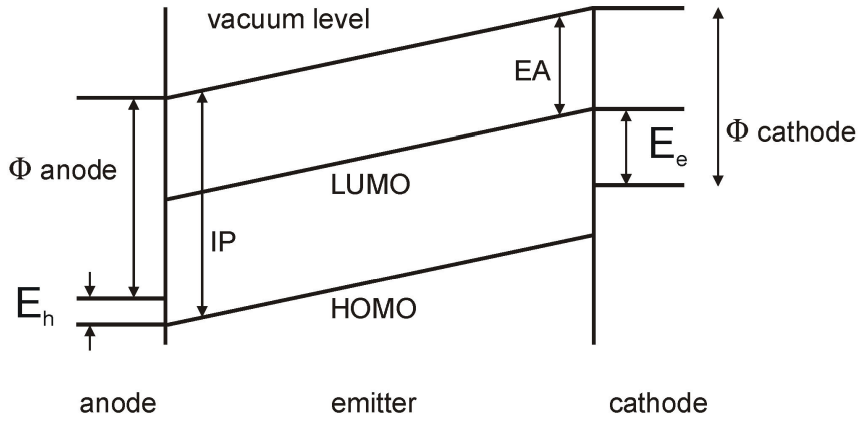

Figure 2.2: Energy level diagram for a simple OLED structure.[16] E_h and E_e refer to the barriers for electron and hole injection respectively. IP stands for the ionisation potential, which gives the necessary energy to separate an electron from its atom. EA stands for electron affinity, which states how capable a material is to bind an electron.[16]

The figure above shows the energy level diagram of the simplest OLED that can be made, where an emitting layer is sandwiched between cathode and anode. The symbols Φ_{anode} and $\Phi_{cathode}$ stand for the workfunctions of the electrodes, LUMO for the lowest unoccupied molecular orbital and HOMO for to the highest occupied molecular orbital. Emission occurs if an exciton recombines in the emitter zone.

For displays the colours red, green and blue are required, but there is also an interest in the other colours of the visible spectrum and especially in white light OLEDs (WOLEDs). In inorganic semiconductors the bandgap is fixed so that only a few wavelengths (most efficiently in the UV, blue, red and infrared region) are available. Blue LEDs are now available but still with high prices.[3] An advantage of OLED materials is their broad emission spectrum. By changing the device structure e.g. by the incorporation of a grating structure the emission spectrum can be narrowed. This way emission can be produced over the whole range of the visible region.

2.2 Liquid Crystals

Liquid crystals (LCs) are mostly known for their application in digital watches and flat panel displays. There they are used as a passive material, blocking the back light or letting it through. In this work active LCs, which are able to emit light will be investigated. In this section an introduction to LC and their properties is given.

2.2.1 Basics

A liquid crystal (LC) is a state of matter between a crystal (solid) and a liquid (isotropic). There exist several types of liquid crystal phases, which are determined by the LC molecular shape, its angular orientation and the degree of order between the individual molecules.

The different LC molecular shapes available include the calamitic (rod-like) molecule and the phasmidic (disc-shaped) molecule. The preferred orientation of a LC molecule is indicated through the director, **n,** see Figure 2.3. This is a unit vector representing an average over all symmetry axes of the LC molecules. The degree of order between the molecules is defined by the order parameter S, which can be represented by [17]

$$S = \frac{1}{2}\left\langle 3\cos^2\Theta - 1 \right\rangle$$

Equation 2.1

Here Θ is the angle between the director **n** and the long axis of the molecule, see Figure 2.3. The angular brackets denote a statistical average over all molecules.[17]

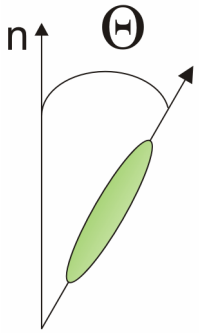

Figure 2.3: Definition of the angle Θ between the director n and a LC molecule.[18]

If all molecules are parallel to **n** the order parameter is S = 1 which denotes the highest possible order. S = 0 states no order at all, hence the material is isotropic. Calamitic

molecules are highly birefringent as a light wave travelling along the long axis of the molecule sees a different refractive index as a wave propagating perpendicular to it.

2.2.2 Structures and Phases

There are two principal liquid crystalline phases for the calamitic (rod-shaped) LC, which are called nematic and smectic.[19] Nematic LCs have an orientational order. They tend to orient in the same direction, whilst smectic LCs have orientational and positional order and they arrange themselves in layers and point roughly in the same direction. Examples for the molecular arrangement of nematics and smectics are depicted in Figure 2.4. For the smectic LCs there are many subcategories including the smectic A and smectic C corresponding to cases b) and c) respectively.

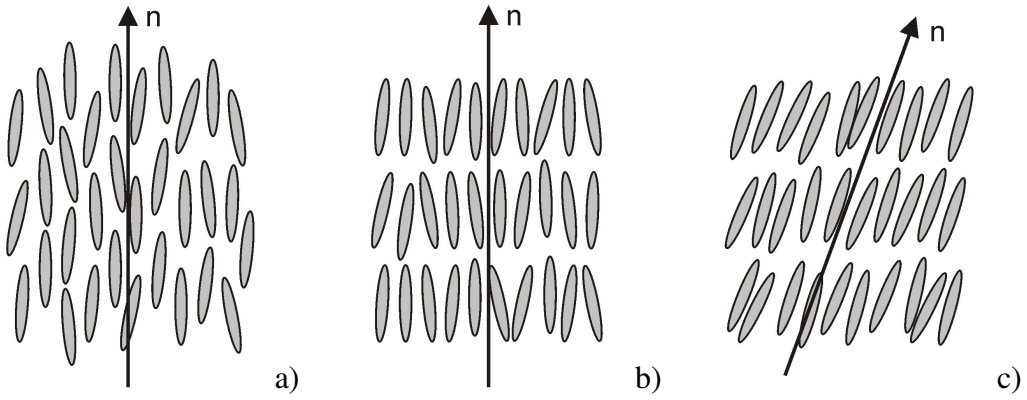

Figure 2.4: Schemes of the phases of calamitic liquid crystals. a) nematic order, b) smectic A order and c) smectic C order.[20]

Chiral molecules in the cholesteric or chiral nematic phase are arranged in a helix as shown in Figure 2.5. The pitch corresponds to the length over which the helix makes a 360° turn.

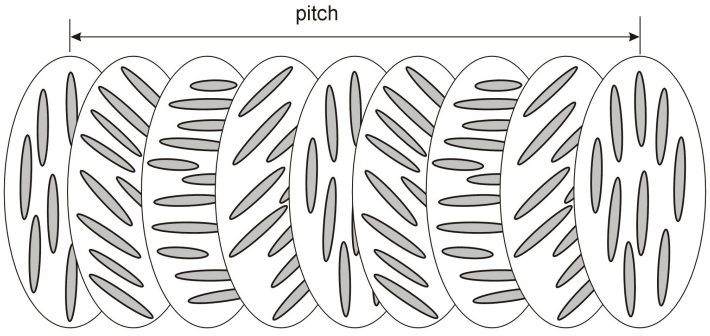

Figure 2.5: The liquid crystal arrangement in a cholesteric phase.[21]

The orientation of LCs with respect to the substrate surface can vary as well and two common configurations are shown in Figure 2.6. Homogenous (or planar) orientation means that the LC molecules align parallel to the substrate surface. Homeotropic means they are oriented perpendicular to the surface.

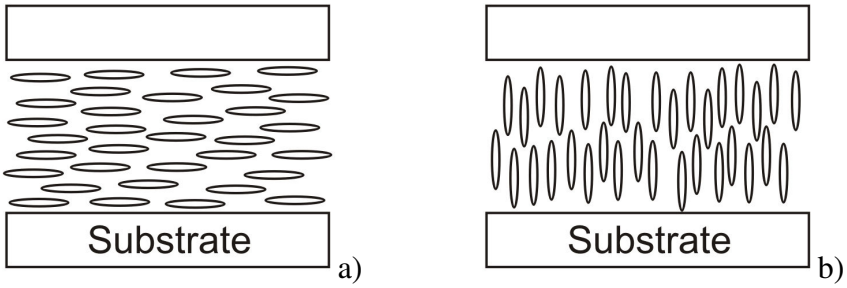

Figure 2.6: a) homogeneous and b) homeotropic liquid crystal orientation.[20]

Figure 2.7 a) shows the homogeneous and b) the homeotropic orientation for the phasmidic molecules in the discotic (columnar) phase.

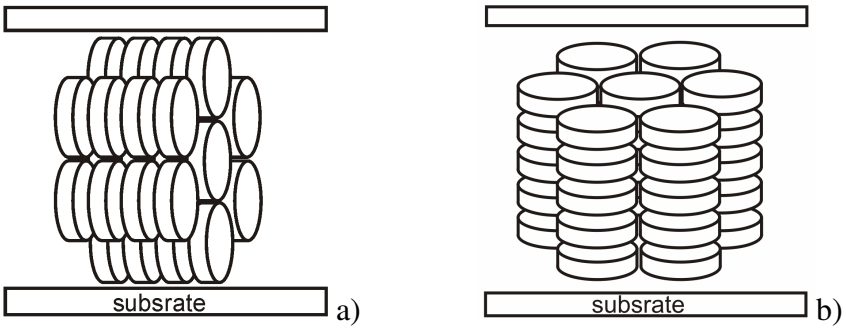

Figure 2.7: Columnar phases of disc-shaped LCs. a) Homogeneous orientation, b) Homeotropic orientation.[16]

2.2.3 Nematic Textures

In this thesis nematic LCs and blends of them are used for the OLED applications. When mixing two different LCs one has to make sure that no phase separation occurs and that a nematic phase is obtained at room temperature to avoid charge trapping at grain boundaries. Therefore the blends have to be observed under a polarising microscope, see Chapter 3.1.4. Figure 2.8 shows a few typical examples for nematic textures.

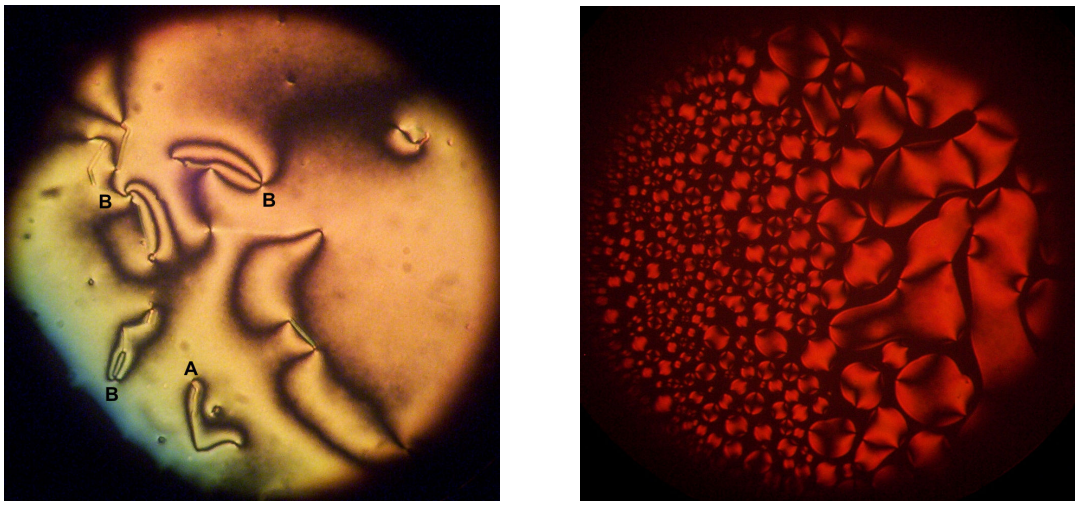

Figure 2.8: On the left a typical nematic texture shows the characteristic 2- and 4-point brushes, labelled A and B respectively. On the right nematic droplets, which appear near the clearing point are shown. Both pictures were obtained from the compound SPK146 and viewed using the oculars of a polarising microscope.

A nematic compound should show a typical Schlieren texture with the so called 2-point and 4- point brushes like in the left picture in Figure 2.8 and droplets on cooling from the clearing point, picture on the right. The origin of the brushes is due to the molecular arrangement around point defects, see Figure 2.9.

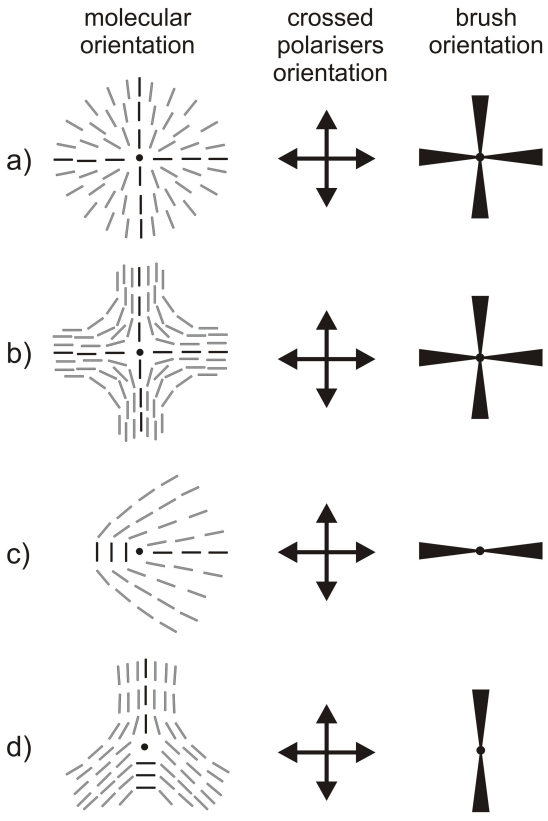

Figure 2.9: Possible arrangements of nematic molecules around point defects.[22] The blackened molecules indicate that they are either parallel or perpendicular to one of the polarisers.

The nematic material has to be positioned between crossed polarisers to be able to observe the Schlieren texture; see Chapter 3.1.4 for more information on polarising microscopy. Regarding for example case a) one can see that some molecules (highlighted in black) around the point defect align parallel or perpendicular to the crossed polarisers, which are indicated by the black arrows. These areas appear dark under the microscope. The light is polarised by the first polariser. Molecules parallel or perpendicular to the polarisation direction behave not birefringent as only one refractive index interacts with polarisation direction of the polariser. The initial polarisation direction of the light passing through the nematic film is therefore not altered and blocked by the second polariser so that the area appears dark.

2.2.4 Liquid Crystal Displays

Commercial liquid crystals, e.g. in flat panel displays, do not emit light. Depending on their orientation they block or transmit light coming from a backlight source. This ability is the main feature used in all LC displays. In the simplest device e.g. a two tone display in a digital watch as shown in Figure 2.10, the black digits are created due to blocking of the backlight. These watches however do not use a constantly running background light source but employ a mirror which reflects the incoming daylight.

Figure 2.10: Digital watch with LC display from Nike.

This ensures a low power consumption but can cause problems in very bright conditions. Figure 2.11 shows one example of the many different types of available larger, colour LC flat panel displays, in this case an active matrix thin film transistor LC display. Going from left to right, light from an unpolarised constantly running background light source is passing through polariser 1 thus changing the light to be horizontally, linearly polarised. The polarised light then enters a cell, which is filled with LCs. The surfaces inside the cell are treated so that the LCs adopt a certain orientation, in this case parallel to the surface (homogeneous orientation, see Figure 2.6). The two cell walls are

positioned in such a way that they align perpendicular to each other. The LCs close to wall A align horizontally and the molecules near wall B vertically. The LCs in the middle then twist slightly molecule by molecule as illustrated for the upper beam in Figure 2.11. If now (horizontally) polarised light enters the cell its polarisation direction will be turned by the LCs so that it is vertically aligned when it arrives at wall B. The white light then passes through a colour filter and through polariser 2. The latter is oriented perpendicular to polariser 1. So only light whose orientation is turned through the LCs would then be able to pass polariser 2.

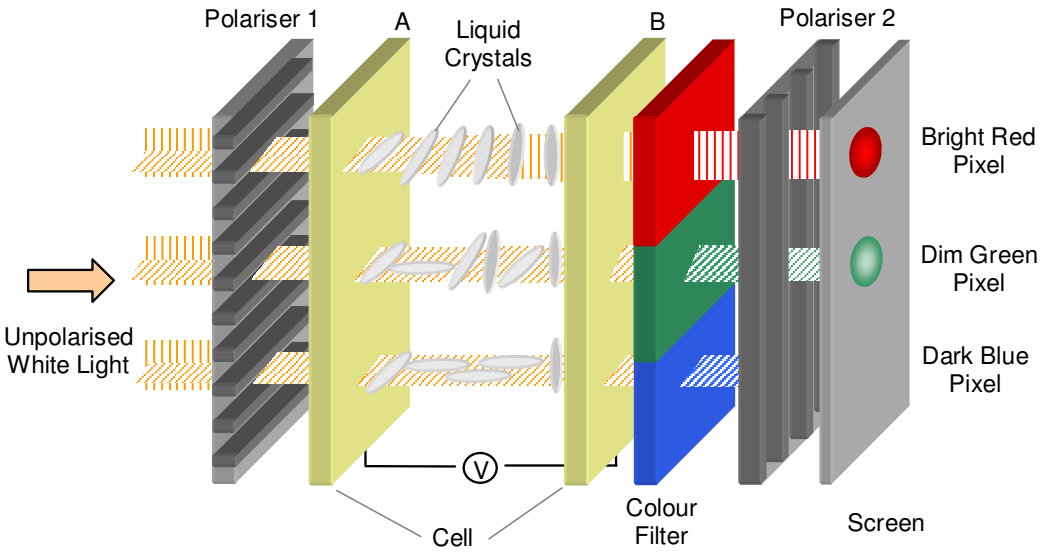

Figure 2.11: Simplified layer structure of an active matrix thin film transistor liquid crystal display. Note that the cell walls are simplified and in reality would contain a grid of transistors, which can be addressed separately. Each pixel is associated with one transistor and can hence be controlled independently.

An array of thin film transistors (TFTs) is incorporated in cell wall A. Each TFT is associated with one pixel. In this case three different pixels (red, green and blue) are regarded. Each transistor controls the voltage across the cell for its corresponding pixel. If no voltage is applied (off state) like in the red pixel case the polarised light experiences a 90° turn when passing through the cell and then can exit through polariser 2 to display a pixel on the screen. In the case of the blue pixel a voltage is applied (on state) across the cell for that particular pixel, which causes all LCs, except those bound at the surface, to align homeotropically. Because of that the polarisation direction of the light is not turned and the light hence not transmitted through polariser 2. The blue pixel remains dark. In the third possible case (green pixel) a voltage is applied to the cell but it is different to the blue pixel case so that the twisted LC orientation is only slightly

changed. This ensures that some light can pass through polariser 2. The green pixel is then visible but is not as bright as the red pixel. Different colours are created by mixing the three main colours red, green and blue by addressing three different pixels that are very close together. This multilayered structure causes a lot of losses as every time the light passes through a polariser or filter some part of it is absorbed. The background light source emits unpolarised light. Only a small fraction of the light, about 42 %, is transmitted through the first polariser.[23] Here therefore the loss is the greatest. A white light source that emits polarised light would overcome this problem, which provides the motivation for section 5 of this thesis.

2.2.5 Light Emitting Liquid Crystals

Figure 2.12 shows a typical structure of a light emitting liquid crystal. These molecules can be different in their spacer, side chain and in their end group size. The chemical structure of the aromatic core (chromophore) can be tailored to control the colour of emission and the energy of the highest occupied molecular orbital (HOMO) and lowest unoccupied molecular orbital (LUMO).

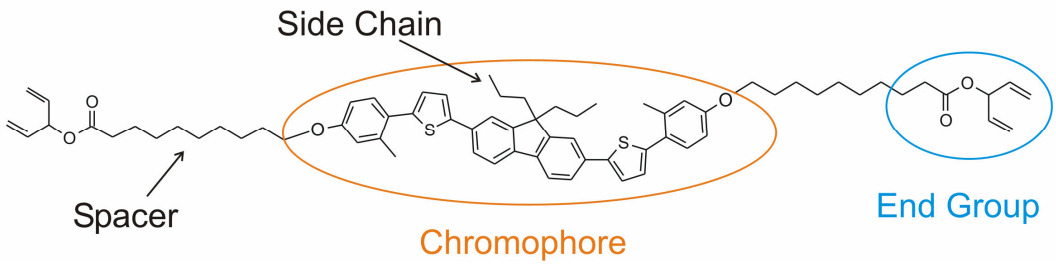

Figure 2.12: Example of the chemical structure of a light emitting liquid crystal.

Side chains and spacers can be added to influence the transition temperatures, solubility and to increase the intermolecular separation.[24, 25] This could prevent possible quenching of the luminescence due to overlapping of the energy levels of the molecules and hence to a reduction of the efficiency. The photopolymerisable end group is required if the molecules need to be crosslinkable, see section 2.2.6.

2.2.6 Crosslinking of Liquid Crystals

For display applications OLEDs need to be able to emit different colours from closely packed pixels. Multilayered devices incorporating charge transporting multi layer films improve the efficiency as with each layer energy level matching can be improved so that

barriers for charge injection can be reduced, which improves the charge transport. The layers are easily prepared by sequential deposition of thermally evaporated small molecules, which can be pixelated by shadow masking. For solution processing the pixelation is mostly done through ink-jet printing. Spin coating or printing would lead to the dissolution of the organic layers below and hence to the destruction of the device. Incompatible solvents have been used to overcome this problem.

Our approach is to crosslink the layers or more precisely the molecules to form a permanent network to render the films insoluble.[26, 27] This is done photolithographically with a laser, which irradiates the film through a mask to pixelate the layer. After crosslinking the uncrosslinked parts are removed by washing the device in toluene or chloroform for several seconds. The next organic layer of another colour is then spin coated over the pixelated layer and crosslinked in a different region. The procedure is repeated until all desired colours are applied. This way our OLEDs can be photopatterned with small pixels and a full colour OLED on a single substrate has been reported.[27] Multilayered devices can also be obtained by crosslinking the entire film. Photochemical crosslinking has been also reported for main chain polymers to form an OLED with red, blue and green emission.[28]

Crosslinking of molecules means the combination of smaller molecules to large chains or networks through polymerisation. Crosslinking can be induced chemically, thermally or through irradiation with light (most commonly from the ultra violet region). In Figure 2.13 the formation of a polymer network is shown. Several molecules are linked by polymerisation of the end groups. The term crosslinking is used if each end of the molecules has a crosslinkable group.

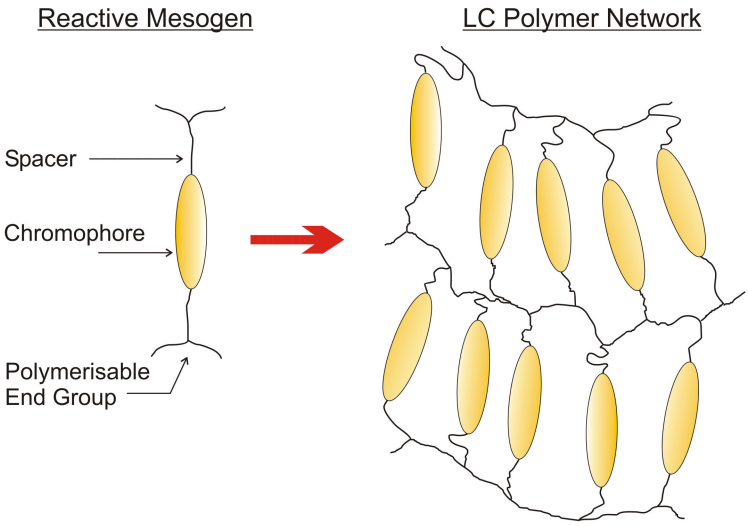

Figure 2.13: Schematic of a crosslinkable single molecule and the resulting molecular network.

A wavelength, which is not close to the emission wavelength, should be used to induce photopolymerisation. Otherwise the network formed might undergo further changes if the OLED is in operation. For OLEDs working in the visible region this can be done by using an end group, which is sensitive to ultraviolet emission. Figure 2.12 shows a diene polymerisable group. This undergoes a free radical cyclopolymerisation reaction (the two end groups form a ring), which is slower than the polymerisation of acrylate or methacrylate end groups. However dienes do not undergo thermal polymerisation so the materials can be thermally cycled during processing.[25] An advantage of the self alignment properties of the nematic LCs is that the emission from uniaxially aligned chromophores is polarised.[26] Crosslinking with polarised emission enhances the polarisation ratio since molecules lying parallel to the polarisation crosslink faster, and their position is fixed. Polarised EL with a maximum polarisation ration of 11:1 was obtained through photoalignment (selective crosslinking).[26] Furthermore patterned polarisation is realisable by crosslinking different spots on a LC film with differently polarised beams. The nematic order was also found to improve charge transport and a hole mobility > 10^{-3} cm^2 V^{-1} s^{-1} was reported for a nematic small molecule.[29] Our semiconducting LCs proved also to be useable for photovoltaics.[30]

2.3 Optical Quantum Efficiency

The external optical (photoluminescence) quantum efficiency (QE) of organic materials (e.g. polymers) is used to evaluate compounds for organic semiconductor devices. A high quantum yield is necessary for efficient light emitting organic devices. The external optical quantum efficiency is defined as [31]

$$\eta = \frac{\text{number of photons emitted}}{\text{number of photons absorbed}}$$

Equation 2.2

If the efficiency of a solution is measured you can assume an uniform angular distribution of the emission whereas for a film this is not applicable. Wave guiding and anisotropic distributions of the polymer chains or molecules within the film cause an unequal distribution of the emission (see section 2.6.2). To ensure that this does not affect the QE results, different compounds in solution or thin film are measured with the use of an integrating sphere. Additionally a laser and a spectrometer, connected to the

sphere with an optical fibre, are needed for the measurement setup. The integrating sphere is a hollow sphere, the inside of which is completely coated with a diffusely reflecting material. The reflectivity should be equal over a large wavelength region. For non-uniform reflectivity a throughput curve of the sphere is needed to correct for the deviation as well as the spectral response of fiber and spectrometer. Barium sulphate is mostly used as coating material but for certain experiments, for example when the emission is near to the infrared region other materials like gold are more suitable. The sphere has two openings; one where the laser beam enters and one where an optical fibre, which is connected to the spectrometer, is attached to. A baffle inside the sphere, which is also coated, screens the fibre from direct illumination coming from the sample and the laser. Figure 2.14 shows the setup for the three measurements which are needed to determine the QE of solutions and films after the method of de Mello and Friend.[31]

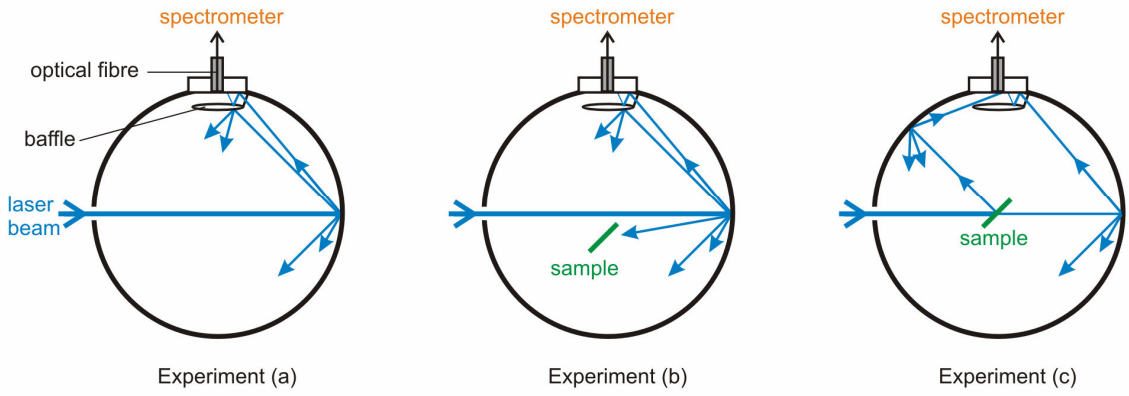

Figure 2.14: The three experimental configurations for the measurement of the optical quantum efficiency with an integrating sphere.[31]

When adjusting the laser beam it is important that the beam does not exit the sphere again after it reflected at the back of the sphere. In experiment (a) only the laser beam is measured. In experiment (b) the sample is placed in the sphere, but not in the direct beam, so that it is excited by scattered light from the laser. In Experiment (c) the sample is directly hit by the beam and its reflection from the sample should not leave the sphere. Figure 2.15 shows typical spectra for these three measurements. For presentational reasons the emission curves were multiplied by a factor of 100 to make them clearly visible against the amplitude of the laser spectrum.

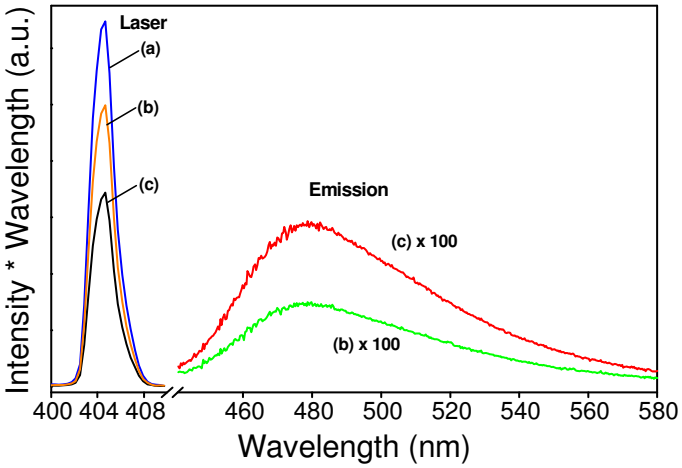

Figure 2.15: Spectra taken for the three different measurements required to obtain for the optical quantum efficiency. Measurement sample was the laser dye Coumarin 30 dissolved in acetonenitrile.

The area under the curve represents the intensity of either laser or sample emission. A measure of the number of photons emitted and absorbed by the sample is required to determine η. The emission intensity x the wavelength is proportional to the number of photons and so is integrated over an appropriate wavelength range. L_i is the integrated signal from the laser for experiment i = (a), (b) or (c). E_i stands for the integrated area of the emission spectrum of the sample. With the equations below the optical quantum efficiency η can then be determined.

$$A = \left(1 - \frac{L_C}{L_B}\right)$$

Equation 2.3

$$\eta = \frac{E_C - (1 - A) * E_B}{L_A * A}$$

Equation 2.4

Here A is the absorption coefficient of the sample at the wavelength of the laser.

2.4 Molecular Modelling

With the invention of computers computational modelling has become more and more important in organic chemistry. The development of fast processors made it possible to

study even more complex molecules like polymers. Nowadays different software packages are available employing different theoretical approaches and theories in quantum chemistry. It is not the aim of this work to explain these in great detail or to compare the different methods. Computational modelling is regarded as another "experimental" tool to examine our light emitting liquid crystals. The simulations on five of our molecules regarding their energy transfer abilities in dimer configurations were carried out under the supervision of experienced researchers (David Beljonne, Bernard Vanbeque and Jerome Cornil) at the Materia Nova research centre from the Polytechnic Faculty of Mons and the University of Mons-Hainaut in Mons, Belgium. Here we give an introduction to molecular orbital theory and the computational terminology and methods employed.

2.4.1 Atomic Orbital Theory

In 1913 Niels Bohr introduced his concept that electrons can only move in orbits around an atomic nucleus. With the help of this model the spectral lines of the hydrogen atom could be explained completely. For many-electron atoms however the model failed and another approach was needed.[32] But the general idea of a confined space in which electrons move around the nucleus is still used today in the form of orbitals. Louis de Broglie then introduced the wave-particle dualism suggesting that high energy particles like photons and electrons show both wave and particle characteristics. This is expressed in the de Broglie relation [33]

$$p = \frac{h}{\lambda}$$

Equation 2.5

where *p* is the particle momentum, *h* Planck's constant and λ the wavelength. Bearing this relationship in mind and employing a quantum mechanical approach, in 1926 Erwin Schrödinger introduced an equation, the so called Schrödinger equation, with which it is possible to find the wavefunction of a particle.[34] This wavefunction ψ describes the behaviour of a particle. For a three-dimensional systems the time-independent Schrödinger equation is written as follows

$$-\frac{\hbar^2}{2m}\nabla^2\psi + V\psi = E\psi$$

Equation 2.6

with $\hbar = \frac{h}{2\pi}$, m the mass of the particle, *V* the potential energy, *E* the total energy and ∇^2 as Laplacian operator.[33]

$$\nabla^2 = \frac{\partial^2}{\partial x^2} + \frac{\partial^2}{\partial y^2} + \frac{\partial^2}{\partial z^2}$$

Equation 2.7

In general the Schrödinger equation can be written as

$$H\psi = E\psi$$

Equation 2.8

where H is called the **Hamiltonian** operator, which represents the left part of the Schrödinger equation. The Hamiltonian is associated with the total energy of the system, which is the sum of the kinetic and potential energy.[34, 33] The square modulus of the wavefunction $|\psi|^2$ of a particle at a certain position is proportional to the probability of finding the particle in that position.[34]

The wavefuntion for one electron of an atom is called an atomic orbital (AO). An electron that is described by this particular wavefunction is said to "occupy" that orbital. The simplest orbitals for the lowest energetic states can be easily visualised. Figure 2.16 shows the boundary surface of an s orbital, e.g. the 1s orbital of a hydrogen atom in its ground state.

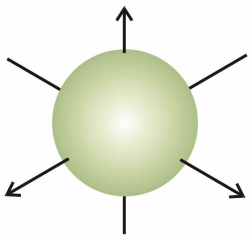

Figure 2.16: The boundary surface of an s orbital, within which there is a 90 % probability of finding the electron.[34]

If an electron is promoted into a higher lying energy level (orbital) e.g. via the absorption of a photon, it may occupy a p orbital. There are three different potential p orbitals as shown in Figure 2.17.

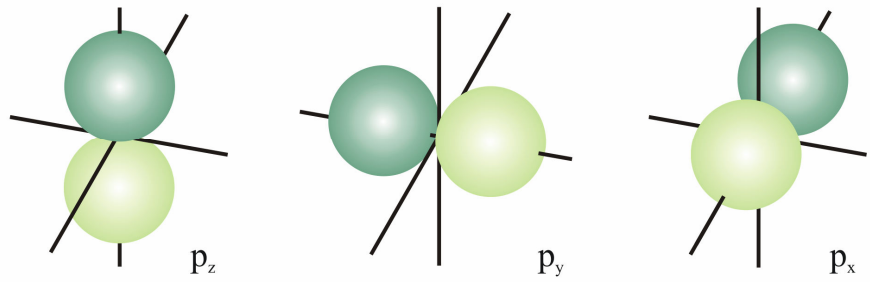

Figure 2.17: The boundary surfaces of p orbitals. A nodal plane passes through the nucleus and separates the two lobes of each orbital. The dark and light areas denote the regions of opposite sign of the wavefunctions.[34]

The higher the energy levels the higher the number of available orbitals and the more complicated the orbital shapes. The energy level of the p orbital is degenerate as all p orbitals are of the same energy.

The occupation of the orbitals in many electron atoms or molecules is built up according to **Pauli Principle**, which states that at most two electrons may occupy an orbital and that if two electrons occupy the same orbital their spins must be paired. The spin of an electron describes its intrinsic angular momentum, which can be imagined as its movement around its own axis.[35] This however is just a classical interpretation to imagine the motion of the electron. In quantum chemistry the spin is quantised and can take the values $+\frac{1}{2}$ and $-\frac{1}{2}$, which is also denoted as spin up ↑ and spin down ↓ respectively. The spins of two electrons in the same orbital must be paired (↑↓), which means that they are not of the same value. In the classical model one can visualise this as two electrons having the same rotational axis, but rotating in opposite directions around this axis. This corresponds to one electron having a spin of $+\frac{1}{2}$ and the other a spin of $-\frac{1}{2}$ with the total angular momentum of a paired spin being zero. Furthermore if an orbital is split into several suborbitals like in the $p_{x,y,z}$ orbitals first all suborbitals have to be occupied by one electron before one can be filled up with a second. This is summarised in **Hund's rule,** which states that an atom in its ground state adopts a configuration with the greatest number of unpaired electrons having the same spin if occupying degenerate orbitals.

2.4.2 Molecular Orbital Theory

In the **molecular orbital theory (MO theory)** it is generally assumed that electrons do not belong to a single atom or bond, but that they can move freely over the whole molecule. The wavefunction for one electron is then called molecular orbital (MO) instead of atomic orbital. The Pauli Principle for AOs is also valid for MOs, so never more that two electrons, whose spins are paired, may occupy a MO.[36] Furthermore the number of MOs created is always equal to the number of AOs that combine.[36] An example is shown in Figure 2.18, where two equal atoms (A and B) e.g. hydrogen atoms combine and two new orbitals here depicted as energy levels are formed. They are called bonding and antibonding orbitals (energy levels).

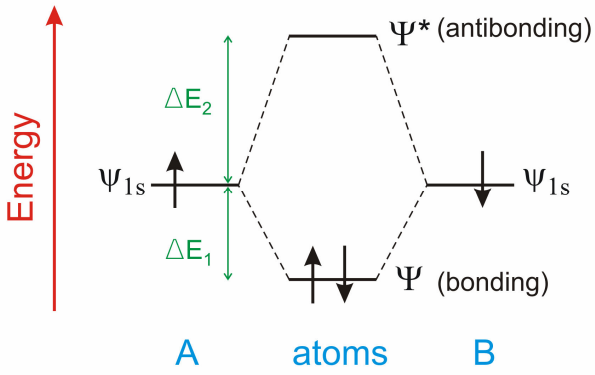

Figure 2.18: Energy level splitting when two identical atoms A and B get close together and form a bond. Ψ is the bonding and Ψ* the antibonding molecular orbital.[36]

In the bonding orbital of a hydrogen molecule, the wavefunctions ψ of the electrons are of the same sign and overlap constructively in the region between the two nuclei so that the possibility of finding an electron in that area is therefore very high, see left part of Figure 2.19. The presence of the electrons between the nuclei reduces the repulsion of the latter and the total energy decreases.

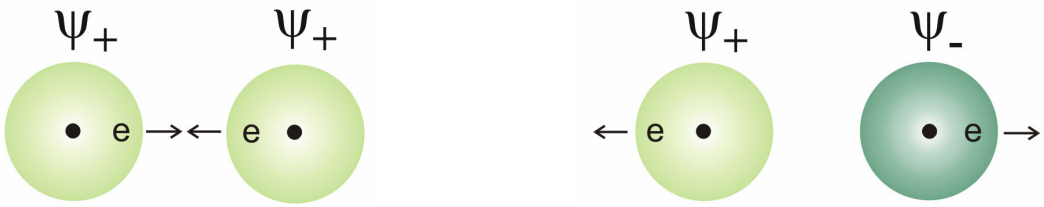

Figure 2.19: Pictorial representation of the formation of orbitals, bonding (left) and antibonding (right).

In the antibonding case the signs of the two wavefunctions are opposite and they add up destructively. Therefore the possibility of finding an electron between the two nuclei is

very low and their repulsion is high. This bond is very unstable giving the term antibonding orbital. Also the total energy is much higher due to the coulombic repulsion, as indicated in the energy level diagram above. The molecule is in its ground state with the two electrons in the bonding orbital. An electron can be transferred to the antibonding orbital, e.g. by the absorption of a photon and then the molecule would be in an excited state. This state is shortlived (μs to ns) and the electron quickly returns to the bonding energy level. In the case of two helium atoms both orbitals are fully occupied, but as the antibonding energy ΔE_2, see Figure 2.18, is always greater than the bonding energy ΔE_1 the bond is not permanent. Therefore helium molecules are called metastable and cannot exist for a long time.[34]

2.4.3 Simplifications in Molecular Models

It is not trivial to determine the MOs mathematically. As in the case of many electron atoms an assumption has to be made to get an approximate solution for the MOs. One assumes that each electron gets assigned its own wavefunction. In a hydrogen molecule for example this would be a 1s orbital. Now the electron can be found either in the orbital associated with the first H-atom ψ_1 or in the orbital of the second atom ψ_2. Its overall wavefunction Ψ is then a superposition of both atomic orbitals

$$\Psi = c_1\psi_1 + c_2\psi_2$$

Equation 2.9

where c_1 and c_2 are coefficients, which are adjusted until the total energy is minimised.[32] In general one can write for a molecule with i atoms

$$\Psi = c_1\psi_1 + c_2\psi_2 + c_3\psi_3 + \cdots + c_n\psi_n = \sum_i c_i\psi_i$$

Equation 2.10

where ψ is the wavefunction of a single atom and Ψ the trial wavefunction for one electron on the molecular orbital. This method is called the **linear combination of atomic orbitals (LCAO)**. This method deals with wavefunctions on molecules made from single electron atoms

Further assumptions have to be made to determine the wavefunctions from many-electron atoms. One of the most important ones is the **Born-Oppenheimer approximation**, which supposes that the nucleus of an atom is stationary and its associated electrons are moving relatively to it. This assumption can be made as a

nucleus is much heavier than an electron and hence much slower than the latter. This aids solving Schrödinger equations for atoms and molecules as only the wavefunctions for the electrons need to be determined.[34] For one-electron atoms the Schrödinger equation can be solved completely. In the case of many-electron atoms however this is not possible as the electrons interact with each other, which renders a complete mathematical expression impossible. It is therefore necessary to make an approximation, the so called **"orbital approximation"** or one-electron approximation.[33] Here the electron-electron interaction is neglected and each electron is described by its own wavefunction. For a helium atom with its two electrons one would assign each electron its own wavefunction in the form of a hydrogenic 1s orbital. The overall wavefuntion Ψ for electrons 1 and 2 then would be written as:[33]

$$\Psi(1,2) = \psi_{1s}(1)\psi_{1s}(2)$$

Equation 2.11

Although it is only an approximation, this model proved to be very useful and is the starting point for the description of the more complicated many-electron atoms. Nevertheless electrons repell each other and this fact needs to be considered. The problem is that a wavefunction of an electron can only be determined when the wavefunctions of the other electrons being present are known. As they all depend on each other a solution is impossible. In 1927 D. R. Hartree introduced a technique which later was modified by V. Fock to acquire numerical solutions for many-electron atoms. As a starting point the wavefunctions for all electrons belonging to a molecule are assumed independently from each other and then the total energy is determined. On the basis of these results a new set of wavefunctions, again for each electron separately, is determined as well the corresponding total energy. This process is repeated so long until the solutions for orbitals and energies differ only slightly from each other and a minimum total energy is reached. The solutions are then self-consistent, that is why this method is also called the **Hartree-Fock self-consistent field (SCF)** procedure.[34,33] For closed shell systems this procedure is also called the **restricted Hartree-Fock (RHF)** method. In general this type of mathematical approximation is called the **variation principle**. Here the most important condition is, that the calculated energy is always equal or higher than the ground state energy, but never lower. With the use of further approximations and semi-empirical methods, which employ also experimental results, very good numerical solutions for all atoms were obtained. For molecules even further

simplifications are necessary to get approximate solutions for the MOs. One approach was introduced by Erich Hückel in 1930.[37, 38]

The energy for the trial wavefunction can be determined by a combination of integrals, which are grouped together in a matrix. These integrals are called the **Coulombic, resonance and overlap integrals**. Imagine a hydrogen molecule consisting of atoms A and B with two electrons (1 and 2) being present. If the two nuclei are sufficient far apart from each other the two atoms are treated as two independent atoms, though still being a molecule. The energy of electron 1 is then mainly described by the Coulomb integral, which considers only one wavefunction. Electron 1 is described by ψ_A and electron 2 by ψ_B.[32,33] If the two nuclei are closer together the electrons are also described by the resonance integral, which describes an electron's movement under the influence of both nuclei. If the two wavefunctions of atom A and B overlap to a great extent see Figure 2.20, the overlap integral has to be taken into account.

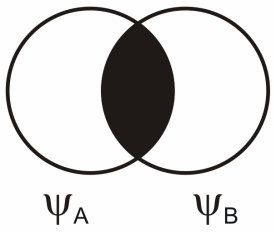

Figure 2.20: The overlap of two 1s atomic orbitals. The shaded area indicates the part that contributes to the overlap integral.[33]

The LCAO method does not suffice to describe larger molecules, as the integrals would be too complicated to solve. That is why further approximations were introduced by Erich Hückel. In the so called **Hückel approximation** all overlap integrals atoms are set to zero. Hence the energies ΔE_1 and ΔE_2 in Figure 2.18 become equal.[33] Furthermore all Coulomb integrals are given the same value. Lastly resonance integrals between non neighbouring carbon atoms are either set to the same value or to zero as well.[33] These restrictions were very severe but they delivered very interesting results at that time.[32] They are also still a good example for the assumption and simplifications that are required if molecules are modelled.

2.4.4 Modelling of Conjugated Systems

Hückel's method applies to planar conjugated systems as for example conjugated hydrocarbon chains. It assumes that electrons in σ- and π- bonds act independently from

each other.[32] A typical example for these two types of bonds is shown in Figure 2.21 and Figure 2.22.

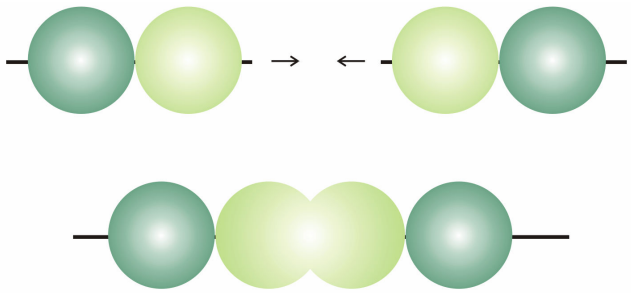

Figure 2.21: Top: Two collinear p orbitals are shown. Below: Their overlap forms a σ-bond. If viewed along the axis from the side the bond looks like a s orbital, hence the name σ-bond.[34]

In general all single bonds are sigma bonds.[36]

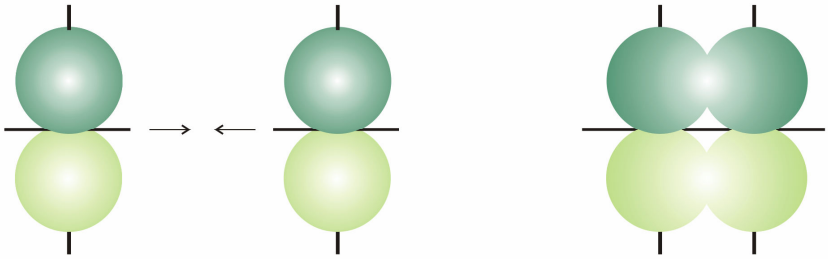

Figure 2.22: On the left are two separate p orbitals that form a π-bond (right). If viewed along the axis from the side the bond looks like a p orbital, hence the name π-bond.[34]

In a conjugated hydrocarbon chain single and double bonds alternate, giving the arrangement presented in Figure 2.23. The π-bonds are delocalised so that the two structures are resonant.

Figure 2.23: Conjugated hydrocarbon chain.

The backbone of the chain is built out of σ-bonds. The electrons contributing to these bonds are very confined in their movement as they are closely bound between two carbon atoms. Therefore Hückel was able to make the assumption to neglect σ- and π-bond electrons interacting with each other. In cases like the conjugated carbon chain or an aromatic ring one can go a step further and assume that the electrons from σ-bonds do not contribute to the MOs due to their confinement and they can therefore be neglected in the MO calculation. Hückel's method was developed before computers

were invented and there are more advanced techniques available nowadays, but in many cases this approach is still applicable.

2.4.5 Energy Level Splitting

The bandwidth or splitting of the highest occupied molecular orbital (HOMO) or lowest unoccupied molecular orbital (LUMO) level is an indication of the conducting ability of these levels. In Figure 2.24 bonding and antibonding interactions of the π orbitals in ethylene (C_2H_4) are shown when going from a single isolated molecule to a dimer and then to a stack of a large number of molecules, which results in the formation of bands.

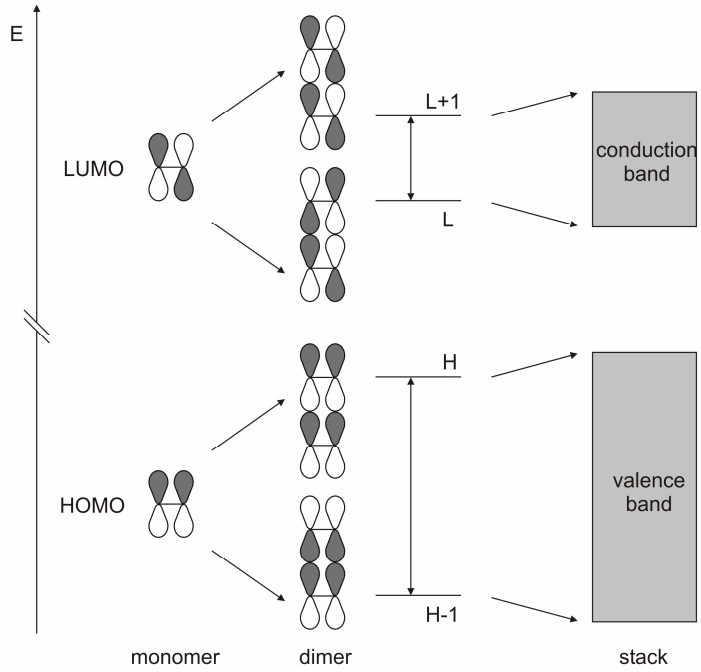

Figure 2.24: Bonding and antibonding π orbitals in HOMO and LUMO levels when going from a ethylene molecule (left) to a cofacial dimer and then to a large number of stacked molecules (right), which leads to conduction and valence band formation.[39] The white and dark lobes indicate wavefunctions of opposite sign.

The HOMO level in the single molecule displays a bonding situation as the wavefunctions of the adjacent orbitals are of the same sign. In the LUMO level the signs are opposite to each other and the total energy is much higher. In the dimer the two interacting HOMO levels of the two single molecules form two new HOMO levels H and H-1, the same happens in the LUMO level, where L and L+1 are formed. The separation of HOMO (H) and HOMO-1 (H-1) is much larger as between LUMO (L) and LUMO+1 (L+1). This can be explained by a closer look at the sign (indicated by the same shading) of the orbitals interacting with each other. In the H-1 case only

orbitals of the same sign are interacting, so the state is fully bonding and lies even lower in energy than the HOMO level of the monomer. In the H level these interacting orbitals are of opposite sign, hence are antibonding and of much higher energy because of the strong repulsion. In the L level the lobes next to each other are antibonding but the repulsion is somewhat compensated as the lobes from dimer neighbours are bonding. In the L+1 level the lobes next to each other are also of different sign as well as the lobes opposite to each other. However the lobes diagonal to each other are of the same sign so that a weak bonding interaction is ensured between neighbours. This difference in the level splitting is being considered as the main reason why holes are sometimes faster than electrons in organic crystalline structures as, in general, one can say that the larger the bandwidth the higher the mobility.[39] However the model in Figure 2.24 is a perfect cofacial arrangement, which is not the usual molecular alignment. Simulations of the HOMO and LUMO splitting due to molecule displacement along the long axis shows that the splitting can vary strongly when a dimer is not in a perfect cofacial arrangement. Cases where the LUMO splitting is two times larger than the HOMO splitting are found; then the electrons are faster than holes.[39]

2.4.6 Electronic Coupling in Dimers

For efficient energy or charge transfer between two molecules a strong interaction (coupling) between these two is required. The transfer rate of an exciton between two adjacent molecules A and D depends on the electronic coupling V_{DA} between A and D.[40] In the Förster theory V_{DA} is usually calculated on the basis of point dipole models. This means that the coupling is determined by the interaction between dipole moments on A (μ_A) and dipole moments on D (μ_D). If μ_A and μ_D are of opposite sign both compensate each other and the coupling is low. Strong coupling takes place for dipole moments of the same sign. This approach is applicable for small molecules but not for larger conjugated molecules, where long range interactions need to be considered. To overcome this problem transition dipole densities instead of point dipole moments are employed to determine the excitonic coupling, which then can be written as follows [40]

$$V_{DA} = \frac{1}{4\pi\varepsilon_0} \sum_m \sum_n \frac{q_D(m) q_A(n)}{r_{mn}}$$

Equation 2.12

with ε_0 being the permittivity of vacuum. Here $q_D(m)$ is the transition density on site m calculated for the lowest optical transition from ground to the lowest excited state on D. The equivalent for molecule A is the transition density q_A on site n and r_{mn} is the distance between sites m and n.[41] This shows that the larger the distance the lower the coupling between A and D. The interaction is dipole-dipole, hence the term through space is often used.[42] The **excitonic coupling model** considers only transitions on one molecule and dipole interaction between D and A, but in reality there are also transitions between different molecules. To account for this additional charge transfer the **supermolecular coupling model** can be used. It adds to the excitonic coupling a) and b) the possible transfer from one molecule to another, cases c) and d) in Figure 2.25.

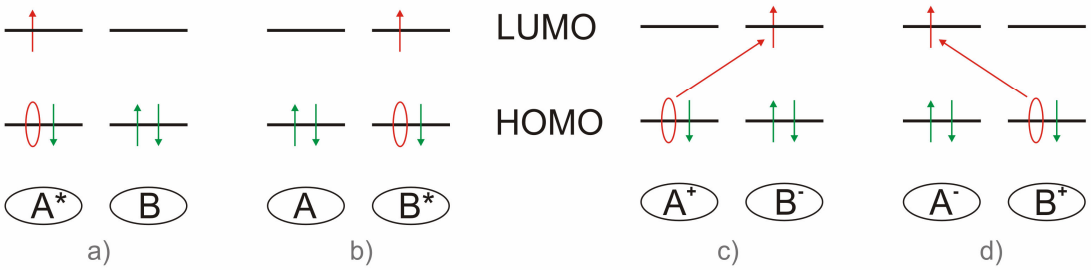

Figure 2.25: Excited state configurations for a dimer made out of the molecules A and B. a) exciton formed in molecule A, b) exciton formed in molecule B, c) electron transfer from the HOMO level of molecule A to the LUMO of molecule B, d) electron transfer from the HOMO of molecule B to the LUMO of molecule A.[43]

For the latter approach the term "through bond" is often used, which indicates that the transfer from one orbital to another, which is further away, takes place over other (bond) orbitals.[42] Hence the supermolecular coupling takes both through bond and through space contributions into account. The coupling values in a dimer are determined by half the splitting of the two lowest optically allowed excited states.[43]

After excitation holes can transfer between the HOMO levels or electrons can transfer between the LUMO levels, see Figure 2.26. This can be considered with a **charge transfer integral**, which represents the coupling between the two states involved.[44] Note that the terms for the different coupling mechanisms are not standardised and vary from publication to publication considering the states involved during transfer and algorithms used. In this work we will use the three expressions; excitonic coupling, supermolecular coupling and charge transfer integral.

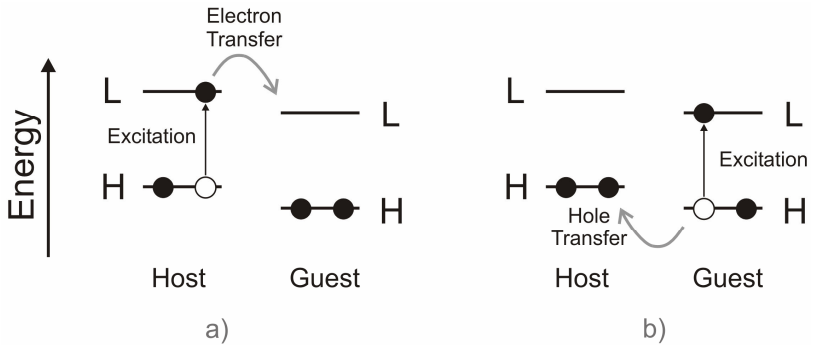

Figure 2.26: Diagram of the HOMO (H) and LUMO (L) levels of a host-guest dimer and a representation of charge transfer after the excitation of either the host followed by electron transfer (a) or guest followed by hole transfer (b). [44]

When considering transfer mechanisms between states one often talks about the coupling between these two states. The transition is allowed and likely to take place if their coupling is strong. Going from a monomer to a dimer can influence the arrangement of the energy levels (orbitals) see section 2.4.5. In Figure 2.24 the case of a perfect cofacial dimer is shown. This is not the most common configuration. A slight displacement along the long axis is not unusual like for the nematic liquid crystals investigated in this work. These shifts and a varying distance between the molecules can also influence on the energetic configuration and hence the coupling.

2.4.7 Molecular Modelling Packages

In Chapter 2.4.2 an introduction into MO theory was given to introduce the kind of assumptions and approximations, which can be made to obtain result for molecular orbitals. With the help of computers it is now possible to get more and more accurate solutions and different approaches are possible. The so called **ab initio** method, which only employs theoretical means, delivers very accurate results but is also very time consuming. Computation times of several months are not unusual. Faster results can be produced with **semi-empirical** methods. They employ experimentally obtained parameters in their calculations. The results are less accurate than those obtained with the ab initio method but are usually close enough to be useful. In this work only semi empirical methods are used.

There are many computer programs available, which consist of different calculation packages. These "packages" contain algorithms based on the different possible approaches to determine the orbitals. Also different accuracies can be chosen, e.g. the number of orbitals or energetic states to be considered. These factors as well as the

speed of the computer processor strongly influence the computational time. Here a brief introduction to the most important packages used is given.

Two very popular simulation software programs are **AMPAC** (Atomic Orbital PACkage) and **MOPAC** (Molecular Orbital PACkage). Both contain different Hamiltonians (algorithms) from which the user can choose.[32] Hamiltonians are for example **AM1** (Austen Model 1)[45] and **PM3** (Parametric Method 3)[46, 47]. Parameterisation means that parameters, which were obtained experimentally, were incorporated into the algorithm. Hamiltonians are not parameterised for all elements. One has to check if the chosen Hamiltonian covers all the elements in the molecule to be calculated. The AM1 is very good when it comes to calculations of hydrogen bonds.[32] An algorithm developed by Zerner is called **ZINDO** (Zerner's Intermediate Neglect of Differential Overlap).[48] It is based on the approximation that certain overlap integrals between electrons are neglected, see Chapter 2.4.3. Different versions of ZINDO, where the parameterisation is specialised e.g. for the calculation of excited states have been developed.

As discussed before the energy of a molecule determined via the Hartree-Fock method is always higher or equal to the real energy value. This is because the electron-electron interaction (e.g. Coulombic repulsion) is not included and the electron is assumed to experience an average electric field. In the **configuration interaction** (C.I.) method the electron correlation is included. So a wavefunction of an electron also depends on the wavefuntion of another electron. The C.I. method is important for excited states simulations. The term single C.I. (S.C.I.) states that only singly excited states are considered during the calculations. For dimer configurations one usually uses optimised monomer configurations to build a dimer. Koopmanns' approximation can be employed, which assumes that the orbital energies of both molecules are the same, which is not always the case, the energy levels might have an offset due to their interaction.[5]

2.5 Absorption and Emission

For optical devices like light emitting diodes or solar cells it is essential to know the absorption and emission spectra of the semiconductor from which the device is made. For solar cells a broad absorption spectrum between 300 - 1000 nm with a peak around 555 nm, as this is the sun's emission maximum, is desirable. For emitters the required spectral width and location of the maximum depends on the application. For displays

the three colours red, green and blue defined according to television standards are required. Therefore a specific emission maximum with a small peak width is necessary. For interior lighting or background light sources in flat panel displays a broad emissive spectrum is needed over almost the entire visible spectrum. These are just a few examples but it shows that spectra are very important when it comes to the characterisation of materials employed in optical devices. Apart from the emissive colour the emission spectra can give information about the structural arrangement of the molecule, its energy levels and transitions between them. In the following paragraph an introduction to absorption and emission spectra and the transitions involved is given.

Absorption and emission spectra are generated via the absorption or emission of electromagnetic radiation. These spectra are specific to every molecule. When a molecule absorbs a photon an electron is promoted from the ground state (GS) to the excited state (ES), which is higher in energy. The missing electron creates a hole in the GS, see Figure 2.27. The minimum photon energy $h\nu_{min}$, where *h* is Planck's constant (*h* = 6.62608 x 10^{-34} Js) and ν the photon frequency for absorption is less than the energy difference between the excited and the ground state (= $E_{ES} - E_{GS}$). This is because the electron and the hole are correlated by a Coulombic interaction. An exciton, a bound electron-hole pair is formed.[49] The minimum photon energy is equal to the exciton energy E_{EX} with $h\nu_{min} = E_{EX} = (E_{ES} - E_{GS}) - E_{BE}$, where E_{BE} is the binding energy of the exciton. In organic materials the binding energy is large because the electron-hole separation is small. Wannier excitons, excitons with a larger separation and thus a large E_{BE}, are found in inorganic semiconductors.[50] The exciton recombines after a characteristic time with the emission of a photon.

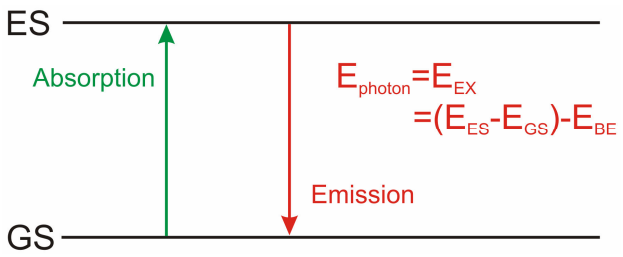

Figure 2.27: Schematic of the absorption and emission of a photon. Through absorption of a photon an electron is promoted from the ground state (GS) to an excited state (ES). Its return to the GS can result in the emission of a photon of the energy E_{photon}.

The transition however can also be radiationless. The schematic in Figure 2.27 shows the minimum absorbed and maximum emitted photon, which are of the same energy. In practice the emitted photon is of lower energy (lower frequency, longer wavelength).

This can be explained by the Franck-Condon principle, which not only considers the electronic states but also their associated vibrational states. Vibrational transitions, which are involved with electronic transitions are called vibronic transitions.[51]

2.5.1 Transition Intensities and Overlap Integrals

Since an electron moves much faster than a nucleus it is assumed that the nuclei geometry of a molecule does not change during the absorption of an electron.[52] Hence only vertical transitions between a GS and an ES are considered, which is stated in the Franck-Condon Principle.[34] In Figure 2.28 the potential energy surfaces for the energies E_{GS} and E_{ES} of a diatomic molecule are shown, where V is the potential energy and r the internuclear distance. The promotion of an electron from the GS to the ES leads to a change in the electronic distribution around the nuclei. Hence the equilibrium separation r_e is different in excited, r_e' and ground state, r_e''. The movement of the electron also causes a change in the surrounding electric field and the molecule starts to vibrate. This gives rise to vibrational states, which are called υ'' and υ' for GS and ES respectively.

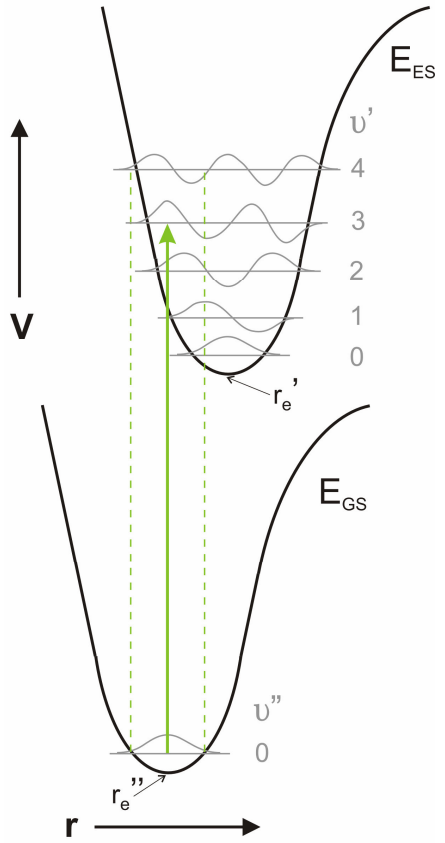

Figure 2.28: Franck-Condon principle for a diatomic molecule. The potential energy surfaces of the ground (E_{GS}) and excited (E_{ES}) state are plotted, where V is the potential energy and r the internuclear distance. Here $r_e' > r_e''$, with r_e being the equilibrium internuclear distance at the potential minimum. The wavefunctions for the vibrational states υ are also plotted. The most likely transition is from υ'' = 0 to υ' = 3, as both wavefunctions have a maximum at the same r_e. The dashed lines indicate the region in which transitions might occur, but with a lower possibility. [51]

The absorption occurs from the lowest vibrational state υ'' = 0 in the GS to the vibrational states υ' in the ES. The vertical transition is strongest where the overlap of the wavefunctions is largest, in this case the 0-3 transition as indicated by the green arrow. In Figure 2.29 the intensities of absorption transitions for two different nuclear configurations $r_e' > r_e''$ and $r_e' = r_e''$ are shown, where $\tilde{\nu}$ is the wavenumber, which is the reciprocal of the wavelength λ.

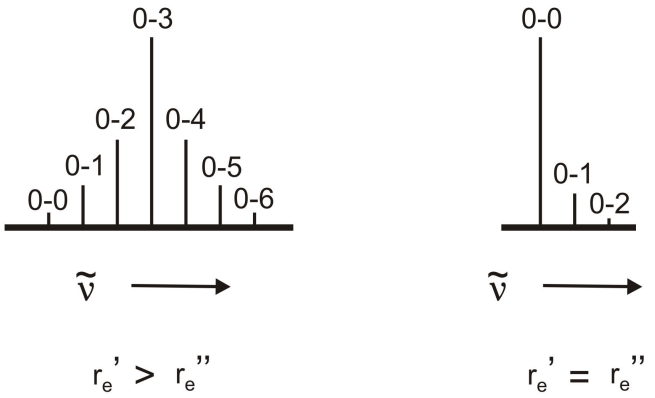

Figure 2.29: Intensity distribution for absorption transitions from υ'' = 0 to various υ' states.. Left: Absorption intensities according to the example from Figure 2.28, where the 0 – 3 transition is the strongest. Right: Absorption intensities for a molecule where the equilibrium distance is the same in ES and GS. Here the 0 – 0 transition is the strongest.[51]

The picture on the left corresponds to the case in Figure 2.28. In the rarer case where the nuclear conformation does not change on excitation the 0-0 transition is the strongest as both wavefunctions are of the same shape and their overlap is therefore very large. Thus the other transitions are very weak. In practical conditions, due to additional influences like solvent polarity, the rotational movements of molecules the spectra do not show single lines but are much broader and often cannot be singly resolved as they are merged together.

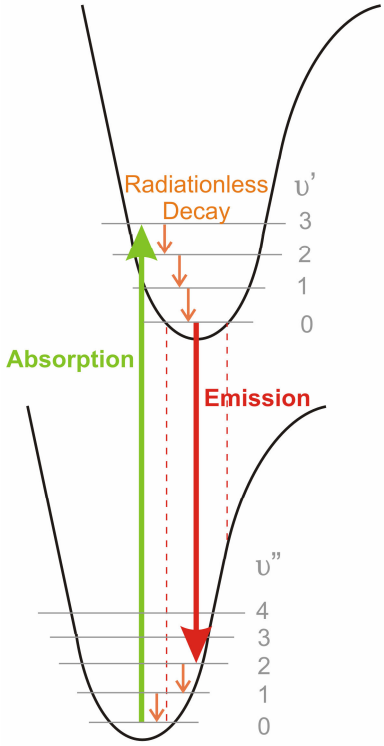

Figure 2.30: Transition steps involved in the absorption and emission process.[34]

The absorption process transfers electrons mostly to higher vibrational levels of ES, the electron is transferred to υ' = 0 via fast radiationless decay. The emission transition, shown in Figure 2.30 is therefore most likely to take place from υ' = 0. From there the electron makes a vertical transition to the GS. Since the equilibrium nuclear configurations from ES and GS are different it is much more likely that the electron is transferred to a vibrational state higher than υ'' = 0. From there it returns to the lowest level via fast radiationless decay. The two bold arrows indicating the strongest absorption and emission transitions show that during the absorption process a much larger energy difference is overcome compared with the emission. Remembering the relationship E = hν, this means that the frequency of the absorbed photon is higher than the energy of the emitted. This explains the often observed shift between emission and absorption spectra shown in Figure 2.31.

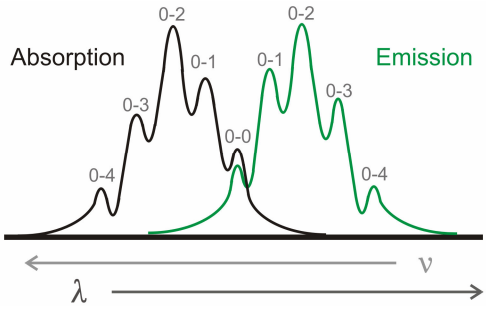

Figure 2.31: Absorption (υ'' = 0 to υ') and emission (υ' = 0 to υ'') spectrum with the strongest transition at 0-2 for both cases. The absorption spectrum shows the vibrational structure characteristic of the ES and the emission spectrum the characteristic of the GS. The emission spectrum is also displaced to lower frequencies, but the 0-0 transitions are coincident.[34]

In the case above the maxima lie at the 0-2 transitions for both emission and absorption. A clear separation is visible, only the 0-0 transition coincides. Sometimes the 0-0 transitions do not coincide, since the energy of the ES can change on occupation.

The so called **Stokes shift** is a measure for the difference in energy (frequency, wavelength) between absorption and emission. The larger the Stokes shift, the greater the difference in internuclear distance (nuclear conformation) for GS and ES and the larger the loss of energy to radiationless transitions.

In the literature one can find several definitions how the shift can be determined. The general definition for the Stokes shift is the difference in energy between the 0-0 peaks of absorption and emission, but especially in absorption these peaks are often not clearly detectable.[53] Often therefore the difference between the absorption and emission maximum is taken. This however is only valid if the peaks correspond to the same

transition e.g. 0-1 for absorption and emission.[54] In Figure 2.32 a typical example for an absorption and emission spectrum from one of our materials is shown.

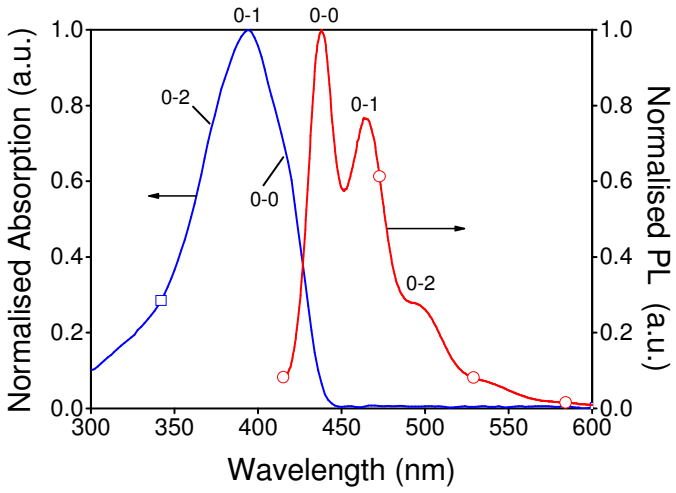

Figure 2.32: Typical example of an absorption and emission spectrum from a light emitting LC in toluene solution.

The 0-0 peak in absorption is hardly distinguishable and we therefore take the 0-1 peak to determine the Stokes shift in this work. It is noted that the corresponding 0-1 peak in emission is not the emission maximum, which was found for most of our materials.

2.5.2 Absorption and Emission in Simulations

In this work absorption and emission spectra will be simulated with semi-empirical methods. In that case the vibrations of a molecule are not taken into account; hence no transitions from vibrational states are calculated. It is however still possible to compare experimental with simulated Stokes shifts since the simulation takes the energy, which is necessary to reorganise the molecule after a transition, into account. In Figure 2.33 a representative sketch of potential energy surfaces of ground state (GS) and excited state (ES) obtainable with semi-empirical methods is shown.

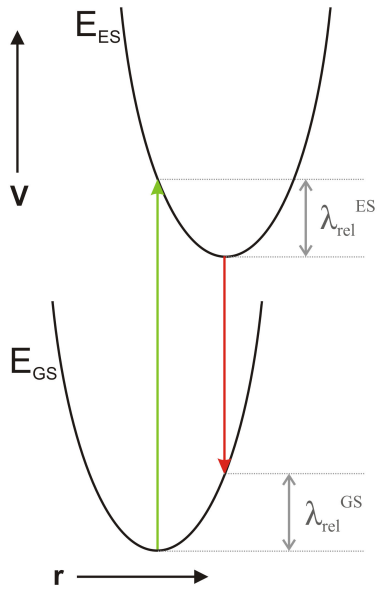

Figure 2.33: Representative sketch of simulated potential energy surfaces in GS and ES and the absorption (green) and emission (red) transitions. The energy lost due to radiationless decay is here indicated by the relaxation (reorganisation) energy $\lambda_{rel.}$ [40]

The green arrow indicates the absorption and the red arrow the emission transition. Position and size of the arrows are similar to the transitions depicted in Figure 2.30. This is because the simulation does take the relaxation or reorganisation energy into account. The relaxation energies for GS and ES are often the same but in general one can say that the Stokes shift corresponds closely to twice the relaxation energy of the excited state.

Beside the vibrations of a molecule the spin properties of electrons influence the shape of a spectrum, as discussed in the following section.

2.5.3 Singlet and Triplet States

The spin characteristic of an electron has already been introduced in section 2.4.1. If an organic molecule absorbs a photon an electron is promoted from a lower energy level (orbital) to a higher lying level. The transition is spin-allowed if there is no spin inversion as shown in the upper part of Figure 2.34.[52] In this case the net spin angular moment is zero as the moments of the paired spins cancel each other out.

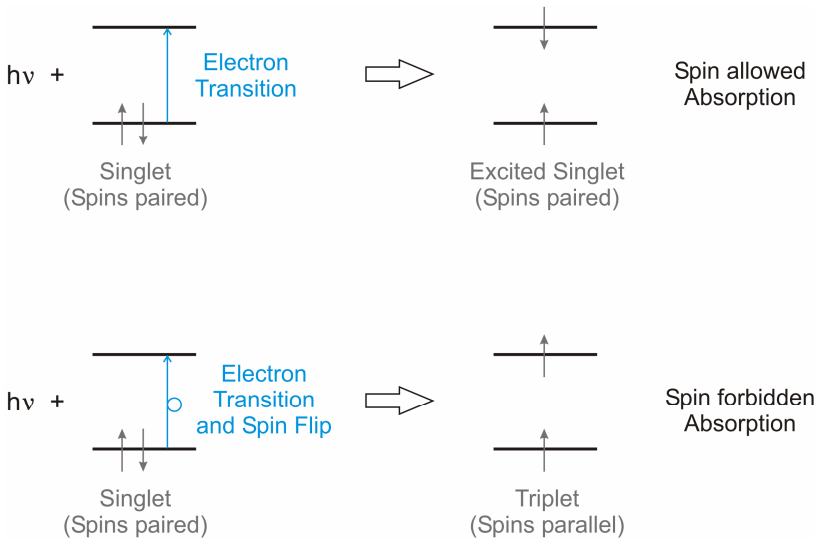

Figure 2.34: The orbital energy level description of absorption. The arrows intersected by the levels represent the electrons and their direction the spin orientation of the electrons.[52]

The lower part shows a spin forbidden transition, where a spin flip takes place. In the excited configuration the spins are then parallel. The net spin angular moment is larger than zero. There are three possible spin configurations (see Figure 2.35) for the parallel case therefore the name "triplet state", which is denoted with "T". In the paired case there is only one configuration possible hence the expression "singlet state" denoted as "S".

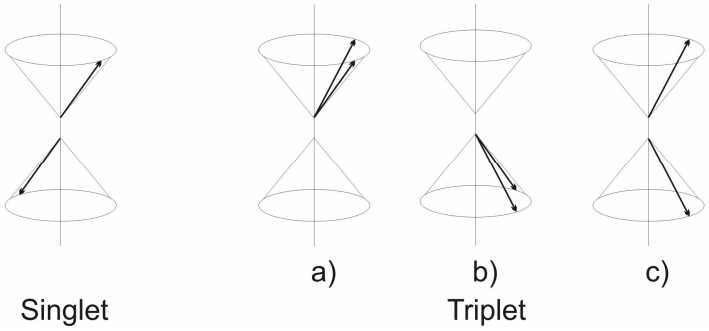

Figure 2.35: Vectorised spin configurations for two electrons with paired spins (singlet) and parallel spins (triplet). For the singlet case only one arrangement is possible and the spins cancel each other out so that there is zero total spin angular momentum. For the triplet case the net spin is nonzero, which can be achieved with three different configurations a), b) and c).[34]

The GS is a singlet state and is therefore called S_0. The lowest excited singlet state is denoted as S_1. The triplet states lie lower in energy than S_1. To depict transfer between S and T states the lowest triplet state T_1 is commonly used to represent the triplets. As in the case of absorption from S_0 to T_1 the emissive transition from T_1 to S_0 is also forbidden due to the required spin flip. Spin flip can occur due the interaction of the

electrons magnetic moment created by its spin and the magnetic moment created by its movement on an orbital, see Figure 2.36.

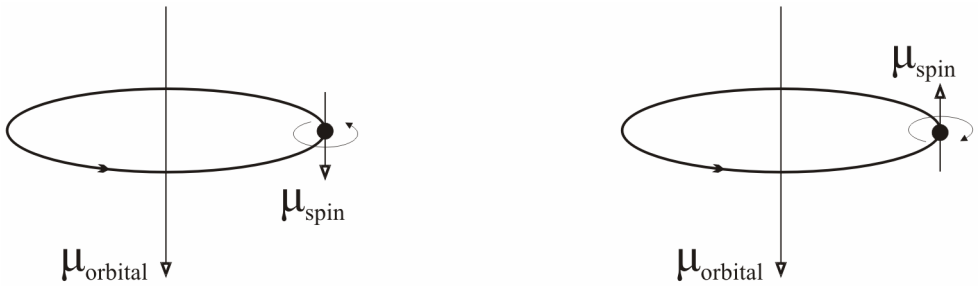

Figure 2.36: The magnetic moments (μ) associated with the orbital and spin angular moments. Left: Motions are in the same direction. Right: Motions are in opposite directions.[51]

The movement of the electron on the orbital creates a magnetic field which for example can cause the lower spin vector in the singlet case in Figure 2.35 to flip to the other side to create the triplet c) configuration. This interaction is called **spin-orbit coupling**. Its strength determines the intersystem crossing between singlet and triplet states. For heavier atoms like sulphur spin-orbit coupling is large and intersystem crossing can be expected.[34]

So far only the excitation via a photon, where $S_0 - S_1$ and $S_1 - S_0$ transitions are the main processes (which is why photoluminescence mainly gives information about the singlet states) has been considered. Upon electrical excitation the triplet states also become occupied. This has the consequence that e.g. in organic LEDs only 25 % of the generated charges are in the singlet and 75 % in the triplet state although there are reports that a higher singlet generation rate is found in polymers.[55, 56] This is a great loss as emissive transfer from T_1 to S_0 is forbidden. To overcome this problem host materials e.g. polymers are doped with guest materials containing heavy atoms, which support spin flips due to strong spin-orbit coupling. In Figure 2.37 the involved transfer processes between host and guest are depicted. Light emission arising from a transition from T_1 to S_0 is called phosphorescence and is much slower (10^{-6} – 10 s) than fluorescence (10^{-12} – 10^{-6} s) due to the required intersystem crossing.[52]

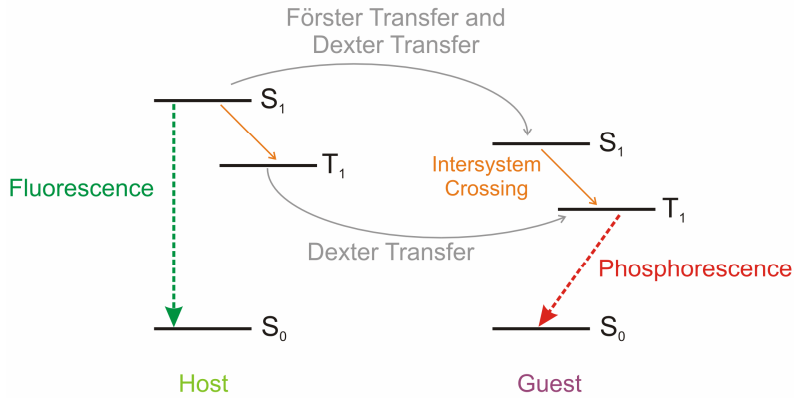

Figure 2.37: Schematic diagram of the transfer processes between singlet and triplet states of host and guest.[56]

For a guest host system the desired emission is the phosphorescence from the guest. To avoid fluorescence it is essential that most of the charges and excitons are transferred from host to guest. The transfer of an exciton from S_1 of the host to S_1 of the guest happens via Förster energy transfer (FET) named after Theodor Förster.[57] He considered a configuration where the energy difference from the fluorescent transitions in the host matches the energy difference of an absorption transition in the guest. This transfer of energy is nonradiative since the dipole-dipole coupling of the transition dipoles on the two molecules results in the simultaneous de-excitation of host and excitation of the guest.[57, 58] To avoid back-transfer, S_1 of the host has to be energetically higher than S_1 of the guest. A good indication for efficient transfer is the overlap of the host's emission and the guest's absorption spectrum when designing a guest-host system.[55]

The FET only occurs between singlet states (allowed transitions) and can take place on a relatively long range. The FET theory was extended by Dexter to include also energy transfer to and from forbidden transitions (triplets). The so called Dexter transfer involves an overlap of the triplet wavefunctions and is therefore confined to very short distances.[59]

2.5.4 General Solvent Effects

The dielectric constant ε_r of the solvent used for the solution can influence the measured spectrum of fluorescent materials. The potential energy V of a system consisting of two charges q_1 and q_2 separated by a distance r is described by

$$V = \frac{q_1 q_2}{4\pi\varepsilon_r\varepsilon_0 r}$$

Equation 2.13

where ε_0 is the permittivity of vacuum.[34] A large ε_r (also called the relative permittivity) corresponds to a high polarity or high polarisability of a medium. Thus the energy of a state decreases with increasing solvent polarity.[60] This means that the higher the polarity of the solvent the larger the bathochromic shift (shift to longer wavelengths). In general only molecules, which are polar themselves, show a large sensitivity to solvent polarity. Nonpolar molecules, like unsubstituted aromatic hydrocarbons, are much less sensitive to solvent polarity".[60] Therefore no general assumption on the ability of a solvent to shift a spectrum can be made on the basis only because of its polarity.[60] The absorption of light occurs within 10 fs and fluorescence needs about 1-10 ns to take place. Solvent effects take about 10-100 ps. The absorption transition is much faster than the solvent effect so that the solvent does not affect the absorption spectrum greatly. Solvent effects however are much faster than the fluorescent transition so that the emission spectrum can be greatly influenced by the solvent. The sample temperature can influence the spectra as well. At lower temperatures solvents become more viscous and solvent effects are therefore much slower. In general one can say that the higher the temperature the larger the shift.[60]

2.5.5 Transition Dipole Moment

The transition dipole moment is a measure of the strength of a transition involving the absorption or emission of a photon. A molecule can only absorb or emit a photon if it at least temporarily possesses a dipole oscillating at the photon frequency. The transition dipole moment, μ_{if} between the initial state $|i\rangle$ and the final state $|f\rangle$, where ψ is the wavefunction for the corresponding state, is defined as:[34]

$$\mu_{fi} = \langle f|\mu|i\rangle = \int \psi_f^* \mu \psi_i d\tau$$

Equation 2.14

Here μ is the electric dipole operator, with $\mu = \sum q_i \times r_i$ and q_i being the charge and r_i the position vector.[34, 51] So a particular transition can only contribute to the spectrum if the corresponding transition dipole moment is non zero. The transition is forbidden when the integral is equal to zero. The transition dipole moment is also directly related to the Einstein coefficient of absorption B, which is a measure of the probability of absorption.[34, 61]

$$B = \frac{|\mu_{fi}|^2}{6\varepsilon_0 \hbar^2}$$

Equation 2.15

The parameter ε_0 is the permittivity in vacuum (ε_0 = 8.85419 x 10^{-12} C^2/J m) and $\hbar$ = $h/2\pi$ with h being Planck's constant.[34] The oscillator strength f is often used to quantify the intensity of an electronic transition at a certain frequency ν.[34]

$$f = \frac{8\pi^2 m_e \nu |\mu_{fi}|^2}{3h e^2}$$

Equation 2.16

Here m_e is the mass of an electron (m_e = 9.10930 x 10^{-31} kg). A large oscillator strength means that the probability for that transition is high.

2.6 Surface Relief Gratings

Gratings with very small periods of about few hundred nanometers are used in many different applications, but especially in small integrated optical devices. They can be incorporated in light emitting diodes (LEDs) or laser diodes (LDs). There a grating can be used to provide a feedback structure, to control the polarisation and the emission spectrum and to enhance the outcoupling of the emission. This work will concentrate on surface relief gratings (SRGs) and their applications in organic emissive devices. In this section a theoretical introduction into grating periods, waveguiding in thin films, phase masks and interference setups is given.

2.6.1 Light Diffraction on a Transmission Grating

Gratings are used in optics to change the directions of electromagnetic waves. Here the waves are not reflected but diffracted. In Figure 2.38 a sketch shows the diffraction of light beam by a transmission a grating.

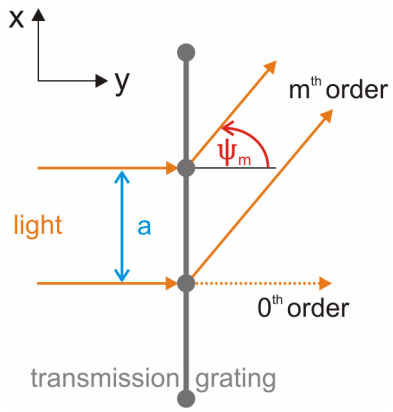

Figure 2.38: Diffraction of light on a transmission grating with the grating period a.[62]

If the grating period "a" is of similar size to the wavelength of the light the rules of ray optics are not valid any more. The light behind the grating is diffracted at angles ψ_m obeying the following relationship [35, 63]

$$\sin \psi_m = \frac{m\lambda}{a}$$

Equation 2.17

where λ is the wavelength in the medium on the right of the grating and m is the diffraction order. The latter can take values of 0, ± 1, ± 2 and so on. For a fixed period and order one can see that the diffraction angle is wavelength dependent. That is why gratings can be used to select single wavelengths from a broader spectrum.

2.6.2 Waveguiding in Thin Films

One of the main limitations of the external efficiency of organic light emitting diodes is that modes are waveguided in the organic film due to its high refractive index n. Figure 2.39 shows some of the possible propagation modes of light generated in an organic layer.[56] Most of the light is reflected at the layer boundaries and is lost by edge emission or by absorption.

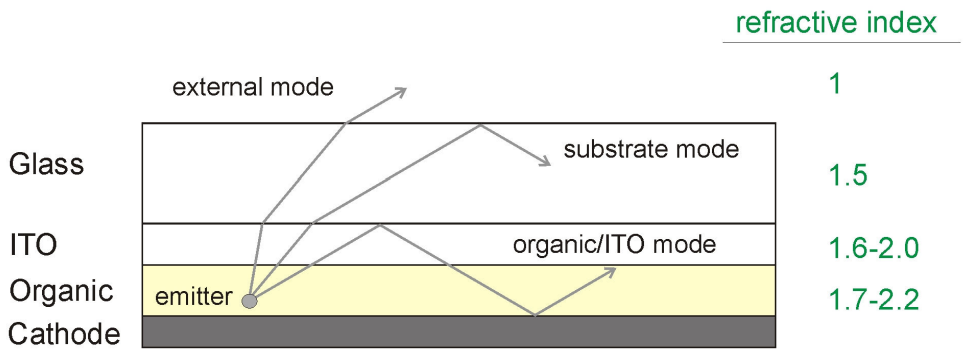

Figure 2.39: Waveguiding in a typical organic light emitting diode.[56]

With Snell's law (Equation 2.18) one can calculate the critical angle Θ_c for total reflection at two layers with two different refractive indexes n_1 and n_2.

$$\sin \Theta_C = \frac{n_1}{n_2}$$

Equation 2.18

Total reflection occurs only if light is transmitted from an optically more dense to a less dense medium, see Figure 2.40.[56] For the passage from the organic layer with a refractive index n of about 2 to air (n = 1) the critical angle would be 30 °. That means only beams with an angle smaller than 30 ° with respect to the normal would leave the device.

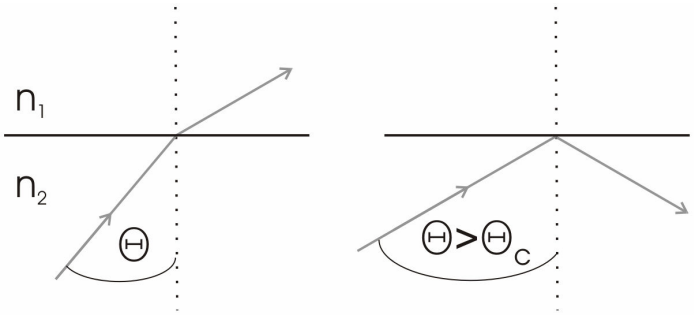

Figure 2.40: Transmittance of a beam from a dense to a less dense medium, $n_1 < n_2$.

The out-coupling efficiency for an isotropic emitting layer, e.g. for small molecules, is given as [56]

$$\eta_{outcoupling} \sim \frac{0.75}{n^2}$$

Equation 2.19

For an emitting dipole like a LC film, where the molecules tend to lie in the plane of the substrate the efficiency increases to [56]

$$\eta_{outcoupling} \sim \frac{1.2}{n^2}$$

Equation 2.20

This however is still not very satisfying. For an organic dipole layer with a refractive index of 2 only 30 % of the light generated would be coupled out. There have been demonstrations that this is just a rough approximation and that a higher percentage can be extracted, it is still a good indication of how much emission is lost due to waveguiding.[56] There have been several approaches to overcome this problem, e.g. the roughening of the glass substrate surface or attachment of lenses to the substrate.[56] Another method is the use of grating structures in the devices to enhance out-coupling by Bragg reflection.[4, 64] Often a corrugated layer underneath the emitting film is used to vary its film thickness and thus its refractive index to create a grating structure.[4, 64]

Our intention is to induce a surface relief grating through photopatterning of an organic light emitting liquid crystal film. Our LCs have crosslinkable end groups, which combine permanently if they are irradiated by UV light, see section 2.2.6. The technique to photopattern the film involves the use of a phase mask. For organic LC films periods in the region of 200 - 300 nm are needed since the refractive index is very high. For example the refractive indices (n) at a wavelength of 633 nm for the commercial materials PPV and MEH-PPV are 2.19 ± 0.02 and 1.7639 ± 0.002 respectively.[65] For two of our LCs refractive indices of 2 and 2.2 with a Δn of 0.5 and 0.7 due to their anisotropic properties were measured for the same wavelength.[6] In the following section the calculation of the required grating periods will be addressed.

2.6.3 Calculation of Grating Periods

The angle Θ of the outcoupled emission with respect to the normal on a film with a surface relief grating is given by the Bragg equation [66]

$$k_0 \sin\Theta = \beta \pm \left(\frac{2\pi m}{\Lambda}\right)$$

Equation 2.21

where k_0 is the free-space vector of the scattered light, β the in-plane propagation vector, Λ the grating period and m the scattering order. The effective index of the waveguide can be written as

$$n_{eff} = \frac{\beta}{k_0}$$

Equation 2.22

with

$$k_0 = \frac{2\pi}{\lambda}$$

Equation 2.23

So for first-order out-coupled modes in normal direction (m = 1, Θ = 0º) the equation becomes

$$0 = n_{eff} \pm \left(\frac{2\pi}{\Lambda k_0} \right)$$

Equation 2.24

Solving for the grating period one gets

$$\Lambda = \frac{\lambda}{n_{eff}}$$

Equation 2.25

With an effective index of 2 grating periods of 200 - 400 nm are required for a wavelength region of 400 - 800 nm. For a laser feedback structure, with light propagating within the film as used in distributed feedback (DFB) lasers the required period Λ_{DFB} is determined as follows: [67]

$$\Lambda_{DFB} = \frac{\lambda}{2n_{eff}}$$

Equation 2.26

This would require even smaller periods between 100 - 200 nm. In practice n_{eff} can be significantly less than the thin film refractive index, so the required periods may not be so small. After the necessary grating period is determined a method is needed to produce a light pattern of that periodicity. Two possible methods are introduced in the following chapters.

2.6.4 Introduction to Phase Masks

Phase masks (PMs) use the diffraction of light to get destructive and constructive interference to create a sinusoidal irradiance pattern. A sketch of a PM with the diffraction orders m = 0, ± 1 is shown in Figure 2.41.

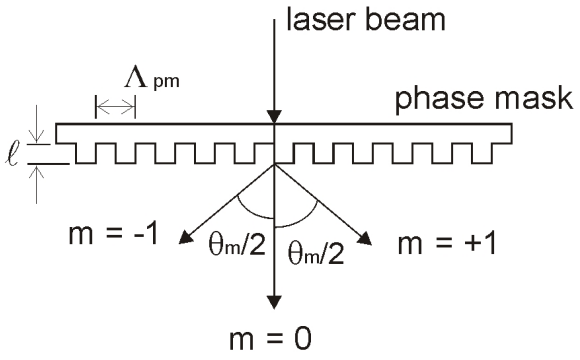

Figure 2.41: Diffraction of a laser beam through a phase mask. Λ_{pm} is the mask period, m is the diffraction order and Θ_m is the diffraction angle of the corresponding diffraction order.[68]

The mask looks like a comb. Depending on the wavelength λ of the laser and the distance between the lobes, which is the PM period Λ_{pm}, the light is diffracted into several orders. Each order is diffracted at a specific angle $\theta_m/2$, which is determined by [62]

$$\sin\frac{\Theta_m}{2} = \frac{m\lambda}{\Lambda_{pm}}$$

Equation 2.27

If light from a coherent light source passes through the mask, some rays travel through the lobes of the mask and so experience a different refractive index and are retarded with respect to the other rays. The rays are in phase and interfere and the length ℓ is ideally chosen so that there is complete destructive interference for the 0^{th} order. Behind the mask interference occurs between the ± 1 orders giving a pattern of peaks and troughs. Since ℓ determines the phase shift, a mask only can be optimized for one irradiation wavelength. Good phase masks have a zero order suppression of 97 %. The second orders should also be suppressed but since their power is a lot weaker than of the first orders their influence is not strongly damaging. For the writing of the grating only the first orders are used.

The period of the irradiance pattern behind the phase PM is

$$\Lambda_g = \frac{\Lambda_{pm}}{2}$$

Equation 2.28

Since grating periods between 200 and 400 nm are needed the phase mask should have a period between 400 and 800 nm. The polarisation of the radiation source plays also an important role in a phase mask set-up. In Figure 2.42 two possible settings are shown. Only the electric component $\overline{E}$ of the beam needs to be considered when setting up the masks. The magnetic component $\overline{M}$, which is perpendicular to the former, can be neglected.

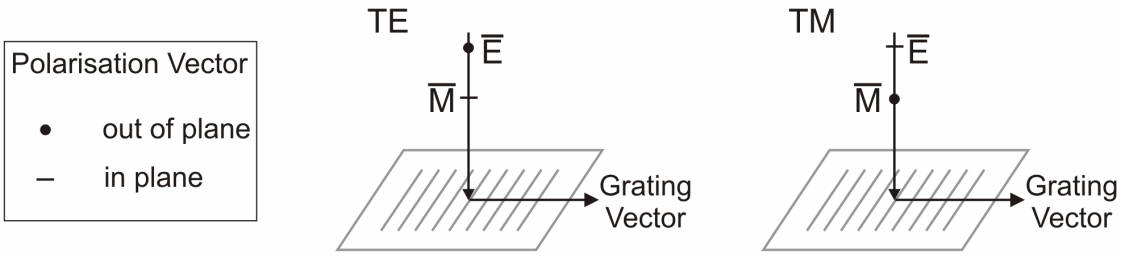

Figure 2.42: Definitions of transverse electric (TE) and transverse magnetic modes (TM) with respect to the groves of a phase mask.

In the transverse electric mode (TE) the electric component is parallel to the grooves of the grating and perpendicular to the grating vector. For the transverse magnetic mode (TM) it is the opposite case. In Figure 2.43 the polarisation directions of the two interfering beams for the two different modes are shown.

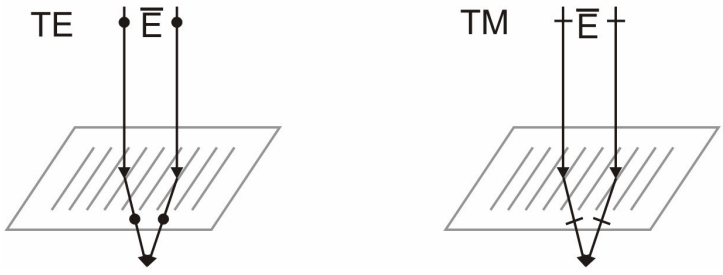

Figure 2.43: Polarisation directions of two interfering beams after passing through a phase mask. In the TE setup the beams are still parallel polarised. In the TM setup the polarisation vectors are no longer parallel but an angle to each other.

For the TE setup the polarisation vectors are still parallel after passing through the mask. In the TM setup however the vectors are at an angle to each other, which leads to an imperfect interference pattern behind the mask. For a neat interference pattern therefore

a laser with a high polarisation ratio is required whose polarisation is aligned perpendicular to the grating vector.

Phase masks have the advantage that they don't need a lot of adjustment and are easily setup. Their period and irradiation wavelength however is fixed. PMs are also expensive, especially when made for small periods and wavelength in the UV region. It can become quite costly if different periods are required. Furthermore they require the mask and substrate to be very close together. Holographic setups offer variable periods over a larger range and no risk of damaging the substrate. They are however not as easy to setup as the PMs and are also more sensitive to environmental influences like vibrations, which will be explained further in the next chapter.

2.6.5 Introduction to Holographic Setups

A typical holographic setup to create an interference pattern is shown in Figure 2.44.

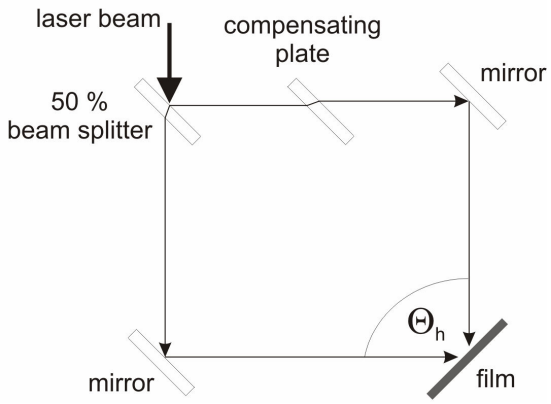

Figure 2.44: A two-beam holographic setup to create an interference pattern in or on top of a thin film.[68]

A coherent light source, usually a laser, is divided by a beam splitter into two beams. An additional plate is placed into one of the beam paths to compensate for the retardation of the other beam, which is travelling through the beam splitter. This way the two beams arrive in phase at the film. Depending on the alignment of the mirrors the two beams hit the film at a different angle. This angle determines the period of the sinusoidal interference pattern that is created on the film. Here this period will be referred to as Λ_h (h = holographic) and can be calculated with [69, 70]

$$\Lambda_h = \frac{\lambda_{uv}}{2\sin\frac{\Theta_h}{2}}$$

Equation 2.29

where λ_{uv} is the wavelength of the laser and Θ_h is the angle between the two beams. For a laser operating at 325 nm one would need an angle of about 48 ° for Λ_h = 400 nm and an angle of about 24 ° for Λ_h = 800 nm. This shows that the availability of the periods created is also limited. For 1 and 179° one obtains the period of about 19 µm and 162.5 nm respectively. In-between these values any desired period can be created. For very small and large angles however the setup might be difficult. This method is non-contact, which is desirable when working with organic layers for electrical devices. Also large scale exposures are realisable, as only a xyz-stage for the substrate would be required to scan it and adjust its height so that the two beams meet on the surface or in the film.

Holographic setups are often used to expose photoresist films, to create a periodic pattern on them.[71] After the film development, where the exposed regions are removed, the substrates are etched so that the areas without photoresist are removed. The layer below e.g. indium tin oxide or silica therefore adopts the pattern. This method is called holographic photolithography and periodicities down to a few hundred nanometers can be produced.[72] These are much smaller those achievable with shadow masks. See section 3.2.2 for further information on photolithography.

The SRGs created are of nanometer scale and can not be checked with common laboratory equipment like a microscope. In this work an atomic force microscope (AFM) was employed to investigate the organic film surfaces. More information on AFMs can be found in the following section.

2.6.6 Atomic Force Microscopy

Atomic force microscopes (AFMs) are used if very small surface variations in the range of Angstroms need to be measured. They are called AFMs because they use the change in force between single atoms as a reference for the change in height on a surface. A sketch of the working principle of an AFM is shown in Figure 2.45.

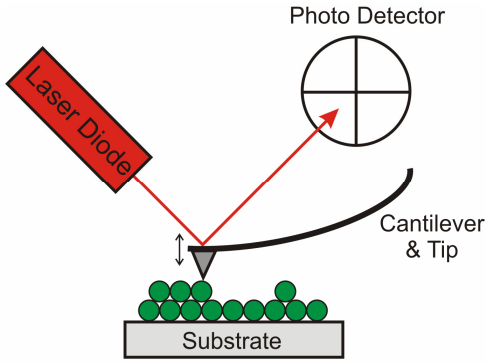

Figure 2.45: Sketch of the working principle of an AFM.

A beam from a laser diode is reflected from the surface of a cantilever to a photo detector. A very small tip of the size of a few atoms is attached below the cantilever. The cantilever vibrates with a specific frequency and scans along the sample surface. If the tip gets close to the atoms on the substrate surface the attractive force between both changes as well as the resonance frequency and amplitude of the cantilever. This changes the position of the reflected laser on the detector. The positional change on the detector can then be translated into a change in substrate height. The mode described is called the non-contact mode. It is non-destructive, as the tip does not touch the surface. It has very high resolution as the weak forces between atoms are strong enough to cause a change in frequency.[73] For soft surfaces, like liquid crystalline films, the tapping mode or also called magnetic AC (MAC) mode is preferable. This mode is similar to the non-contact mode but the tip is much closer to the substrate and therefore shortly touches (taps) the surface with each oscillation.[74]

3 Experimental Procedures

In this section detailed information of the preparation of thin films with our liquid crystals (LCs) is given. The methods required to characterise our materials as well as the techniques used to make an organic light emitting diode (OLED) based on these are explained.

3.1 Compound Characterisation

The light emissive organic materials used in this work are made at the University of Hull, hence their properties are unknown. It is therefore essential to characterise them in terms of their LC transition temperatures, nematic phases, optical quantum efficiency and absorption and emission spectra. In the following subchapters the necessary procedures for the characterisation of our materials are described.

3.1.1 Differential Scanning Calorimetry

Before being able to process the newly developed LCs, a differential scanning calorimeter (DSC) scan was carried out to determine the transition temperatures. Information on these temperatures is essential for thin film preparation; for this work a nematic arrangement of the LC, frozen in a glassy state is desired. Not all compounds are in their LC state at room temperature (RT) and need to be cured at higher temperatures to get a nematic film. For nematics the most important temperatures are the transition from crystalline to LC state denoted as "**N**" for nematic and also called melting point. Further the clearing point, which is the transition from LC to liquid state and denoted as "**I**" is of interest, as this sets the limit of the operating device

temperature, e.g. for an OLED. If the material stays in a nematic arrangement on cooling it possesses a glassy phase. The glass transition temperature from LC to glassy phase is denoted as "**T_g**". A LC is described as monotropic when the nematic phase is only observed on decreasing temperature. Depending on the material it might recrystallise on cooling or another heating cycle. This is denoted as crystallisation temperature "**Cr**".

About 5 mg of the material to be investigated is required for a DSC scan. It is placed in a small aluminium container, which has a lid pressed onto it to seal the container permanently. This ensures that no material gets lost during the scan due to possible evaporation at high temperatures. The aluminium container is placed in a sealed chamber with a known reference sample close by. Before each scan the machine (DSC 7) from Perkin/Elmer is calibrated against a known indium sample. Scans are usually carried out with a scan speed of 10°/min. Two full heating and cooling cycles are recorded to ensure reproducibility of the transition temperatures. One cycle e.g. starts at RT, goes up to 150°C, then down to -30°C and then back to RT. The machine measures the heat flow to and from the sample and reference and compares them with each other. If a material makes a transition from one phase to another it will require more or less thermal energy than the reference source to maintain the same temperature. This difference is detected by the DSC and depicted as either a peak or a valley in the background scan line, where the heat flow is plotted in dependence of temperature. In Figure 3.1 a typical temperature scan of a LC is shown.

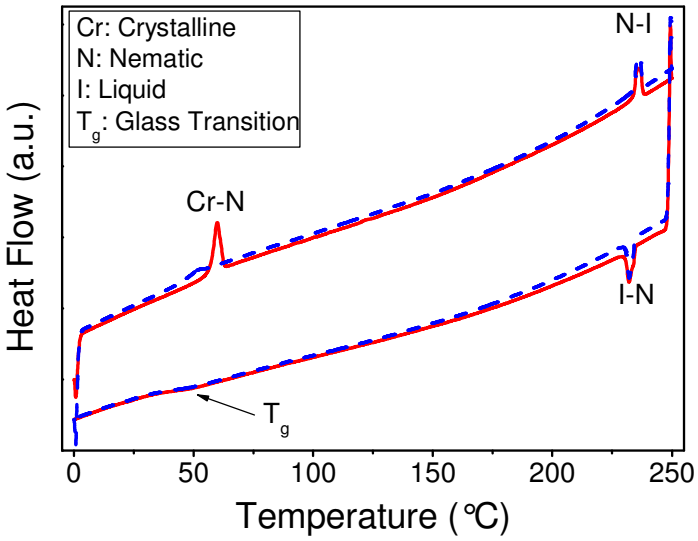

Figure 3.1: Typical DSC graph with two measurement cycles (1st cycle; red, full line, 2nd cycle; blue dashed line). Note that the slight upwards curvature is due to the DSC machine used.

The first measurement cycle starts at 0°C. The Cr-N transition is indicated by the peak at about 60°C, the N-I by the peak at about 236°C and its reverse transition by the trough at 232°C. The glass transition T_g is more difficult to depict as it is indicated by a shallow valley, hence not much energy is required for this transition. The transitions are identical in the second cycle apart from the Cr-N transition, which is now much flatter. This is due to the fact that the material is not crystalline but a nematic glass. The transition to the nematic liquid crystal phase thus requires only a small change in energy. Measuring a blend of two different LCs requires three scans, where the first scan goes at least 20°C above the highest clearing point of the two. This ensures that they both mix homogeneously. On the first cycle one obtains transition temperatures for both compounds individually. On the second cycle they are both mixed and one obtains only one single transition points for the blend.

3.1.2 Absorption and Emission Spectra

When developing new materials for emissive devices it is most important to measure their emission spectra. One here distinguishes between electroluminescence (EL) and photoluminescence (PL). The former stands for the conversion of electric charges into photons the latter for the emission of a photon after a photon of higher or equal energy has been absorbed. It is therefore also of interest to know around which wavelength the material absorbs. The absorption spectra of our LCs in solution and as films are of great interest. In Figure 3.2 a simplified set up for the measurement of an absorption spectrum of a molecule in solution is shown.

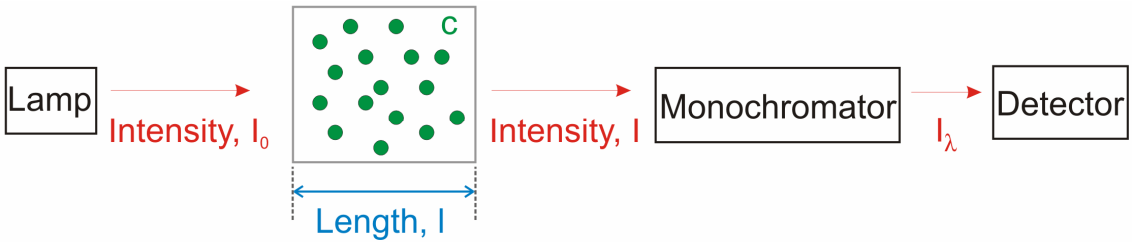

Figure 3.2: Simplified sketch of the measurement of the absorbance of molecules in solution. Here c stands for the concentration of the solution.

First a blank measurement is carried out with only the solvent in the container. The lamp emits light of a wide spectrum, which the grating scans through sequentially. The detector measures the intensity of each wavelength after passing through the blank sample and saves this as the initial intensity I_0. Then the solution prepared with the

same solvent that was used for the blank measurement and the desired molecule to be measured is placed between lamp and detector. The scan is repeated and the intensity I that reaches the detector is compared to I_0 which gives the transmittance $T = I / I_0$ of the sample. The transmittance of a solution depends on the molar absorption coefficient ε, the concentration c and the length l of the sample.

$$I = I_0 10^{-\varepsilon c l}$$

Equation 3.1

Equation 3.1 shows the so called Lambert-Beer law. It is more convenient to talk about the absorbance A of a molecule with $A = \log I_0/I$. The Lambert-Beer law becomes

$$A(\lambda) = \varepsilon(\lambda) c l$$

Equation 3.2

where ε is wavelength (λ) dependent and indicates the strength of a transition. Absorption spectra however are most often broad so that it makes sense to integrate ε to obtain the absorption A_{Band} over the whole band.[34] To measure the absorption spectrum of films the same procedure can be used as for solutions. Here the blank substrate is a clean glass or quartz plate. An identical substrate is then measured with the liquid crystal layer on top.

To record the absorption spectra of our materials in solution and in the solid state as a thin film a dual beam UV/VIS spectrometer Lambda40 from PerkinElmer was employed. The wavelength region was set to 200 – 900 nm. All thin films were deposited on quartz samples of 10 x 10 mm^2 size. The blank measurement, which the spectrometer software subtracts automatically from all measurements, was a clean quartz sample. For the solutions fused silica cuvettes were used as a container, which limited the measurable wavelength region to 385 nm. In this case the blank was a cuvette filled with solvent. In most cases this was toluene.

The EL spectra were recoded during the test of the OLEDs. Device production and testing are described in section 3.2 and 3.3 respectively. After recording, the EL spectra were corrected for the non-uniform spectral response of the spectrometer. The PL spectra in this work are those recorded during the optical quantum efficiency measurements, see Chapter 3.1.3. Samples and solutions were the same as used for the absorbance measurements. The PL measurements were also corrected for the non-uniform response of the spectrometer.

3.1.3 Optical Quantum Efficiency

The photoluminescence (optical) quantum efficiency (QE) measurements were carried out in a barium sulphate coated integrating sphere after the method discussed in section 2.3. The set-up is shown in Figure 3.3. A computer controlled Ocean Optics Spectrometer (S2000) was connected through an optical fibre to the sphere to detect the emission from the sample and the laser. A baffle inside the sphere protected the fibre from direct illumination. Nitrogen gas was introduced through a gas nozzle into the sphere to prevent sample degradation during measurements. A GaN laser diode with an emission wavelength of 406 nm was used as excitation source for the sample.

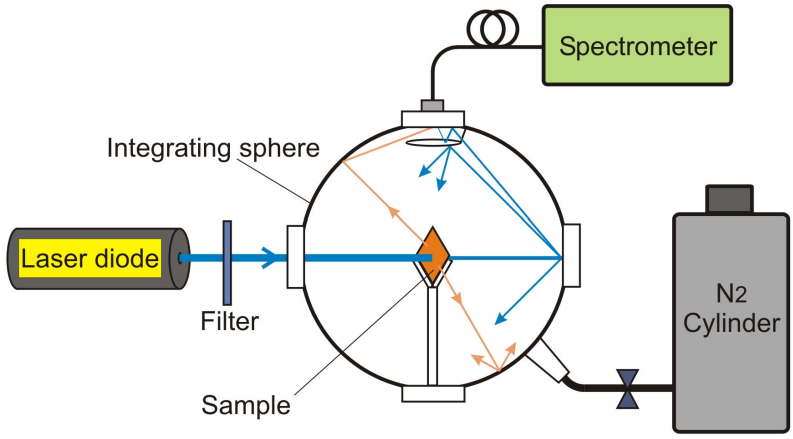

Figure 3.3: Optical quantum efficiency measurement setup.

The spectrometer consisted of a grating, which diffracted the incoming light under different angles, depending on the incoming wavelength, and a line of photodiodes (CCD) measuring the intensity of each wavelength. The spectral response of the CCD within the spectrometer as well as the reflectivity curve of the sphere is not uniform over the whole wavelength measurement range. The measured data was therefore treated with a correction curve to compensate for this error.

It was also checked whether the response of the CCD was linear for different integration times. Therefore the laser was directed into the empty sphere with the laser intensity being reduced, so that the laser peak was just visible in the background noise of the recorded spectrum at an integration time of 5 ms. Measurements for 10 ms, 20 ms etc. were taken. The area below the peak was then integrated and divided by a corresponding factor to be able to compare it to the integral from the 5 ms measurement. The results varied by about 1 %. This is quite small and thus the comparison of measurements obtained with different integration times was acceptable.

Most of the compounds were tested in solution and in a thin film. Toluene or tetrahydrofuran (THF) were used as solvents. Before the measurement the laser diode was warmed up for about 5 - 10 minutes. The use of a filter ensured that the emission of the laser did not saturate the CCD. If a solution was measured it was ensured that not more than a third of the laser power was absorbed. Since the concentration of the compound within the films could not be changed after device production not all films maintained this rule. All films were prepared after the method described in 3.2.6 with spin speeds of 3000 rpm and a compound solvent ratio of 1 mg / 100 µl. As described elsewhere in section 2.3 only three measurements were necessary to determine the efficiency. For measurement (a) an integration time of 5 ms was chosen, so that the laser was in the upper third of the intensity region on the graph displayed by the software. The emission of the sample was much weaker than the laser emission so that the integration time of the spectrometer had to be increased to detect a signal. It is not possible to use only the results of the higher integration times, because then the laser is "overexposing" the spectrometer. So for the three settings (a), (b) and (c), spectra with different integration times were taken. The results of the higher integration time were then divided by the corresponding factor to match a time of 5 ms. The optical quantum efficiency is the ratio of photons emitted/photons absorbed. The CCD within the spectrometers does measure the intensity of the light, but for the QE the number of photons and not the intensity is relevant. A blue photon is of higher energy than a red one; hence the intensity measured in the blue region is higher than in the red for the same number of photons. To correct for this the measured intensity (counts) was multiplied with the corresponding wavelength value (nm). As an example the already corrected spectra from a PV316 film are plotted in Figure 3.4. The laser emission, measured with an integration time of 5 ms, is integrated over 402 – 408 nm for the three different set ups (a), (b) and (c). The recorded PL spectra (300 ms) from the PV316 film are integrated from 500 – 700 nm for set ups (b) and (c). The PL result is then divided by 60 to match the values obtained with 5 ms. With Equation 2.3 and Equation 2.4 from section 2.3 the values for the quantum efficiency corresponding to an integration time of 300 ms were determined.

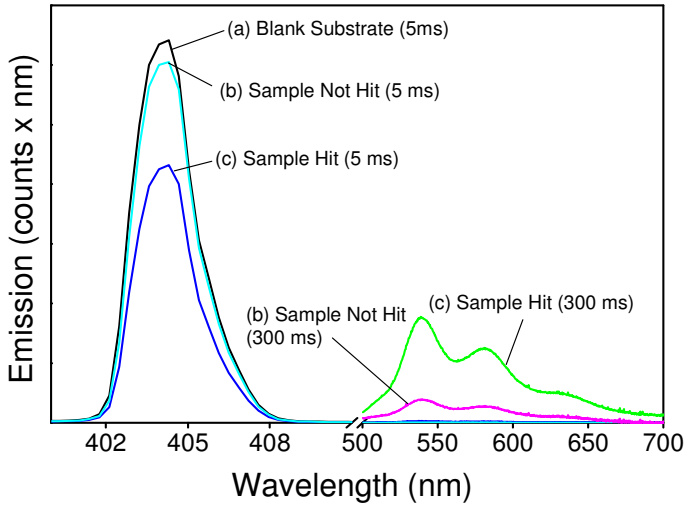

Figure 3.4: Spectra of an exemplary quantum efficiency measurement for a PV316 tetrahydrofuran film.

Two separate measurements were made on two different areas of each film to check for the homogeneity of the film and the reproducibility of the results. Each spot was measured with three different integration times. After treating the results with the correction curve the quantum efficiencies for the different integration times as well as the different spots were calculated. The final value was the mean value of all of them. The error stated corresponds to half the difference of maximum and minimum value measured. For solutions, a homogenous distribution of molecules can be assumed hence only one spot was measured for three different integration times. As a reference the laser dye Coumarin 30 dissolved in acetonitrile was measured. Literature states a optical quantum yield of 67 % in acetonitrile.[75] For a solution of similar concentration we obtained 69 ± 3 % and which agrees with the literature value.

3.1.4 Polarisation Microscopy

In this work mainly nematic LCs were investigated. Apart from DSC measurements (section 3.1.1) a polarised microscope can be used to determine transition temperatures. The temperatures however can not be measured as accurately as the environmental temperature is not as well controlled as in a DSC chamber. The textures of liquid crystals however are best determined optically with the microscope. The anisotropic properties of LCs make it possible to observe phase transitions e.g. from crystal to nematic state when heating a thin nematic film.

A polarisation microscope is quite similar to commonly used microscopes in laboratories except that two polarising plates called the polariser and the analyser are incorporated. A simplified sketch of a polarising microscope is shown in Figure 3.5.

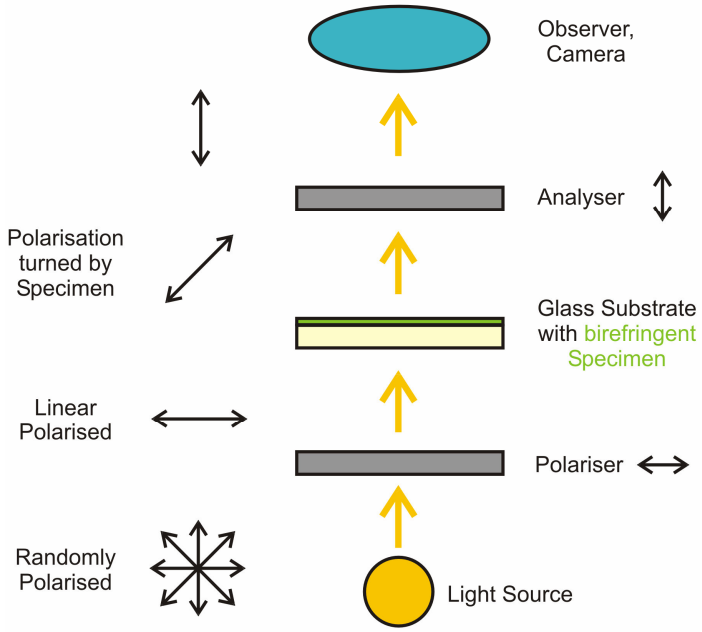

Figure 3.5: Simplified sketch of the path of light and its polarisation direction in a polarising microscope.

Randomly polarised light passes through a polariser to create linear polarised light. This passes through the transparent substrate, which has a thin LC film on top. LCs are highly birefringent and influence the polarisation direction so that a part of the light can pass through the analyser, which is aligned perpendicular to the polariser. An isotropic medium does not affect the polarisation and the light is blocked at the analyser so that the observer sees only darkness. In Figure 3.6 three typical textures observed through a polarising microscope are shown.

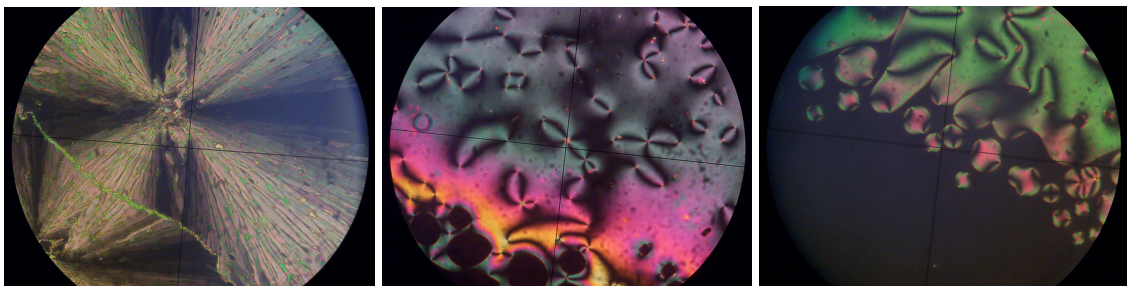

Figure 3.6: Textures of a nematic LC observed with a polarised microscope; crystalline (left), nematic (middle) and nematic to liquid (right) phase.

In this work mainly nematic LCs are investigated, which show the characteristic four- and two-point brushes in the picture in the middle or the droplets on the right. For our

OLED applications that employ LC blends it is important that both mix well and no phase separation occurs. An example for a phase separation is shown in Figure 3.7

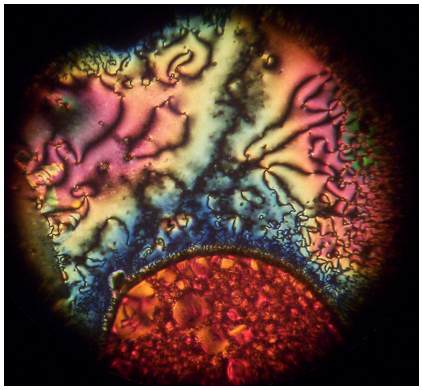

Figure 3.7: Phase separation in a blend of two different liquid crystals. The red area at the bottom is a patch of neat material, which is has not blended with the surround material.

Before the blends were tested in OLEDs their miscibility was investigated under the microscope. Therefore about 1 mg of the mixed (see section 3.2.7 for blend preparation) and in most cases crystalline material was deposited onto a clean microscope slide and a glass cover slip was pressed on top. The slide was then shortly heated with a fan to melt the crystalline material. Now being slightly viscous it was mixed by carefully pressing down and rotating the cover slide on top. After the microscope slide was cooled down to room temperature it was placed onto the hot stage, which is incorporated in the microscope. The sample was heated at 10°/min to about 5°C above its clearing point. When determining exact transition temperatures a slower heating rate is necessary but they were obtained with a DSC. The cleared material was mixed again with the cover slide and cooled down with 0.2°C/min to ensure nematic alignment. When a nematic texture could be observed the cooling rate was set to 5°C/min. After reaching room temperature it was ensured that no phase separation had taken place and that the nematic phase was maintained. If this was the case the blend was applicable for further investigation in OLED devices.

3.2 OLED Preparation

In this section the steps carried out to build an organic light emitting diode (OLED) in our facilities are presented. An OLED is a multilayer device, which ideally would be made out of organic materials only, but so far a better performance is achieved if

inorganic materials and metals are used as well. Figure 3.8 shows the OLED structure used in this work to test different emissive compounds and mixtures in terms of brightness, efficiency, polarisation and colour coordinates.

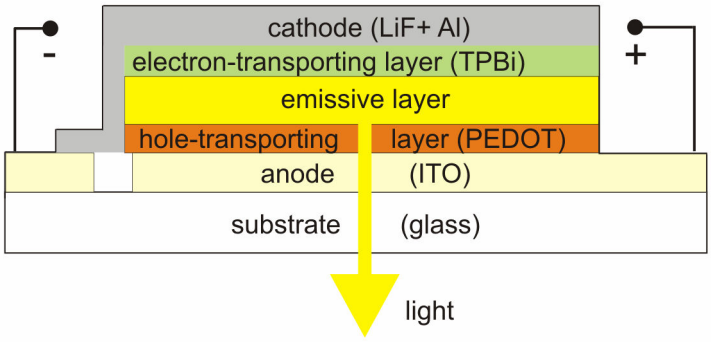

Figure 3.8: Typical OLED structure for the testing of our compounds.

Each device production step is described separately in the following subchapters. During the substrate preparation, powder free gloves were worn and as much handling as possible was carried out with tweezers, to prevent contamination of the substrates and the layers on top. Due to the sensitivity of the emissive compounds their treatment was carried out in a glove box under nitrogen atmosphere with an oxygen content of about 15 ± 15 ppm and a humidity between 0.1 and 3 ppm.

3.2.1 Substrate Cleaning

A glass slide of size 25 mm x 45 mm and precoated with indium tin oxide (ITO) with on top was used as substrate. The ITO, being transparent to visible light, acted as an anode. First the substrates were sonicated for 30 minutes in a 3:1 mixture of a conventional resist stripper SVC175 (Chestech Ltd) and deionised (DI) water to get rid of any grease on the substrates. The solution was heated previously to above 65°C for optimal cleaning efficiency. Afterwards the substrates were rinsed with DI water and then sonicated in (warm) DI water for 15 minutes. This was done twice to get rid of any possible stripper residue. Then the substrates were sonicated for 10 min in acetone to get rid of the water. The last sonication (10 min) was done in methanol or isopropanol to minimise the Schlieren on the substrates when they were blown dry with nitrogen afterwards. To get rid of any possible water residue the substrates were placed in an oven at 100°C for 2 hours and afterwards stored in a new dust free petri dish.

3.2.2 Photopatterning of the ITO Anode

Before the hole transporting layer could be spin coated on top, the ITO anode had to be patterned by photolithography and plasma etched. For the former the following steps were carried out.

First the cleaned substrate was baked at 100°C for 30 minutes to ensure that no moisture was left on its surface. Once cooled down about 10 substrates were then lined up in 2 rows in a fume cupboard. A small film of S1813SP15 photoresist was sprayed on top using sweeping stripes from side to side for about 3 to 4 times. The substrates were covered directly afterwards to prevent any dust deposition on them. After a few minutes they were placed in Petri dishes to let the photoresist film dry for several hours.

The patterning of the photoresist followed. The substrate was placed on a mask, which had the shape of the desired electrode layout. The photoresist was then exposed for 20 minutes with ultraviolet light (UV, 350 - 450 nm) see sketch in Figure 3.9.

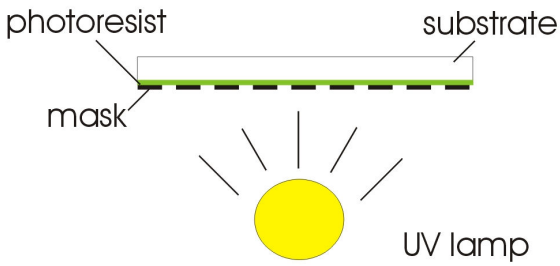

Figure 3.9: Patterning of the photoresist.

The mask used for all devices was the same size as the substrate and is shown in Figure 3.10. The transparent (white) parts let the UV light through so that the photoresist properties were altered. The colour of the photoresist then changed from green to brown. The grey areas of the mask blocked the UV light. The blue dashed line indicates the four OLED test areas, which can be controlled separately with the anode contacts.

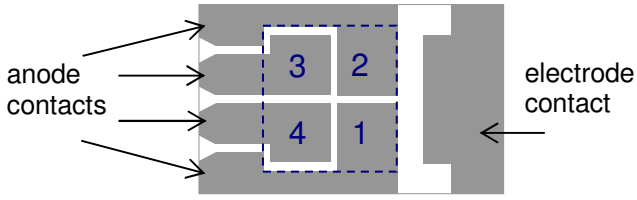

Figure 3.10: Electrode layout of the OLED substrates. The four numbered squares indicate the four different test areas which could be addressed separately through the anode contacts.

After the exposure the substrate was placed in a lukewarm mixed solution of one part 351 photoresist developer and five parts DI water for about 30 seconds so that the exposed regions of the photoresist were completely removed. The substrate was the rinsed in DI water and blown dry with nitrogen gas.

Meanwhile a recrystallisation dish with an etching solution was heated up to 70°C. The substrate was then bathed in the acid for 20 - 30 minutes to remove the ITO. The photoresist protected the substrate from the acid so that only the regions without photoresist on top were removed. Thus the ITO took the shape of the mask used during the UV exposure. The substrate was sonicated in acetone for 15 minutes to remove the residual photoresist and then cleaned again as described in section 3.2.1.

3.2.3 Oxygen Plasma Etching

Oxygen plasma etching was used to smooth and clean the ITO surface as well as to lower its work function to enhance carrier injection.[76] During the etching process spikes in the ITO layer were removed, which could cause shorts between the electrodes of the OLED. This treatment was always carried out shortly before the substrates were intended to be used for a device, because if stored for longer than a month, the ITO layer could oxidise and would need to be plasma etched again.

For the plasma etching the already patterned ITO substrate was mounted in a holder with the ITO side facing down in a vacuum chamber so that only about 2 mm along both the long edges were covered. The chamber was evacuated down to 1.3×10^{-9} bar and flushed with pure oxygen sequentially for about 5 times to ensure a pure oxygen environment. After the last evacuation step oxygen was admitted so that a constant pressure of 0.26 mbar was maintained. An electrical field (200 - 300 V) was applied transversely to the substrate, which ionised the oxygen. The oxygen plasma was maintained for 10 - 12 minutes. Afterwards the substrates were sonicated again for 10 min in acetone and 10 min in isopropanol. Then they were blown dry with nitrogen and stored in an oven at 100°C for about an hour and afterwards stored in a new Petri dish.

3.2.4 Spin Coating of the PEDOT Layer

After the plasma etching and cleaning a few substrates were transferred into a nitrogen filled glove box. Each substrate was spin coated with poly(3,4-ethylene-dioxythiophene) also known as PEDOT, which would form the hole transporting layer. The PEDOT was

purchased at H.C. Starck Ltd under the trade name Baytron®P VP AI 4083. The spin coater held the substrate by vacuum, was set to 4000 revolutions per minute (rpm) for 30 seconds. The PEDOT was applied onto the substrate with a syringe through an attached filter (pore size: 0.45 µm). When the substrate was completely covered it was directly turned by the spin coater. Afterwards the substrate was placed on a hotplate to heat it from room temperature to 50 ºC where it was baked for 5 minutes. Then the hotplate was turned up to 165 ºC to bake the substrate for another 10 minutes. Then the heater was turned of, so that the substrate could cool down slowly (about 10°C/min). The substrate was stored in a nitrogen gas environment if not used directly for further processing.

3.2.5 Rubbing of the PEDOT

To obtain polarised emission from the OLED the liquid crystal molecules of the emissive layer had to be aligned. Therefore the PEDOT layer below the LC layer had to be rubbed, see set up in Figure 3.11.

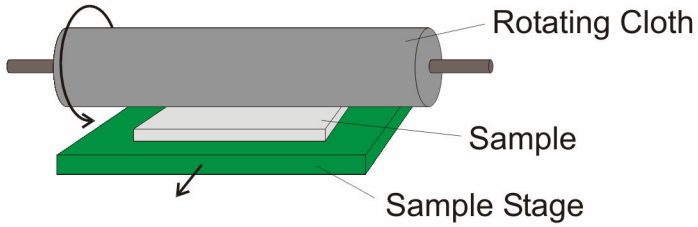

Figure 3.11: Mechanical rubbing of a PEDOT covered substrate.

This was done by moving a PEDOT covered substrate below a rotating velvet cloth. The rotation of the cloth as well as the movement of the sample stage was controlled by a motor and was the same for all rubbed samples in this work. The distance between cloth and sample was adjusted with micrometer screws so that the cloth just touched the sample surface. The samples were translated five times below the rotating cylinder to even out possible irregularities in the cloth.

3.2.6 Spin Coating of the Organic EL Layer

Before a substrate could be coated with an organic layer a solution with the desired LC was prepared. The necessary quantity depended on substrate size and number. For a 1 cm^2 large substrate about 100 µl were required. In this work solutions with compound -

solvent ratios of 1 mg organic compound in 100 µl of solvent were used. For the standard substrate 25 mm x 40 mm, 400 µl and hence 4 mg of compound were mixed.
For the weighing procedure a cleaned sample tube was needed. It was rinsed with DI water, submerged in acetone and then blown dry with nitrogen and put for 1 hour in the oven at 100°C. This was always done for several sample tubes at once, which then were stored in the glove box. Prior to the weighing, to ensure that no residual water had settled on the sample tube, it was put on a hot plate at 105 ºC for 5 minutes. It was then placed in a balance. The inside of the balance was treated with an anti-static gun to get rid of any electrostatic charges before the balance was zeroed. The sample tube was then taken out and put back in the balance again. The inside was treated again with the anti-static gun. If the balance did not display zero weight the whole zeroing procedure had to be repeated. With the help of a clean spatula a small amount of the organic compound was then placed in the sample tube. Before any reading was taken the inside of the balance was treated with the gun again. The last step had to be repeated until the desired amount of compound was found. During the whole weighing procedure the pressure in the glove box was kept constant since the smallest pressure increase or decrease could cause deviations in the weighing result.
The right amount of solvent corresponding to the measured weight was then added to the compound in the sample tube to form a solution. The solvent could be chloroform, toluene, tetrahydrofuran or dichloromethane. These were purchased at Sigma-Aldrich Co. and were the purest version available (anhydrous 99%, packed under nitrogen). In almost all cases toluene was used. It proved to dissolve our compounds best and due to its high boiling point of 110 - 111°C did not evaporate during spinning and hence formed an even film. Before the spin coating the ITO/PEDOT coated substrate was heated up to 105 ºC for 5 minutes to get rid of any possible water residue. Once the substrate was cooled down it was covered with the previously prepared organic solution. This was done with a syringe to which a 0.02 µm pore size filter was attached to get rid of any possible dust particles in the solution. The substrate was turned for 30 seconds at 3000 rpm. Afterwards the sample was carefully placed onto a hotplate and heated up from room temperature close to its particular transition temperature, where it would become a liquid. The substrate stayed on the hotplate for 10 min (20 min if the temperature was below 100°C and toluene was used) and afterwards cooled down to room temperature at 10°C/min. The next processing step was carried out immediately afterwards to prevent any degradation of the LC layer due to traces of water and oxygen in the glove box.

3.2.7 Blend Preparation

The blend ratios discussed in this work are based on the molecular weight of the compounds. The required amounts were weighed in separate sample tubes. Then about 1000 µl of solvent was added into one sample tube and stirred until it was fully dissolved. The solution was then transferred to the other sample tube and carefully shaken to ensure a homogeneous blend. The tube was then placed under vacuum for 12 h to get rid of the solvent. The dried specimen was also used when blends were investigated under the polarising microscope.

3.2.8 Crosslinking of the Organic Layer

To permanently join (crosslink) the liquid crystal molecules together the emissive layer was exposed to ultraviolet light from a 325 nm laser. The laser model was a IK3552R-G HeCd from KIMMON Koha Co, Ltd, which had a linear polarised emission with a measured polarisation ratio of 5.5:1. Since not all organic compounds were crosslinkable this step was not always necessary. Crosslinking made the organic layer insoluble so that if desired another organic layer could be spin coated on top. The required crosslinking fluence depended on the compound. As a rule of thumb it was found that blue emitters needed a fluence of about 400 J/cm^2, green emitters about 600 J/cm^2 and red emitters about 800 J/cm^2. The total laser output power varied between 35 to 53 mW and was checked previous to the crosslinking process to calculate the exposure time needed to achieve the desired fluence.

The beam spot profile was doughnut shaped so to avoid non-uniform irradiation the laser scanned over the substrate so that each part saw the same amount of fluence on average. The laser had a spot size of 4 mm in diameter. The four test areas (area size: 8 mm x 8 mm) were scanned as shown in Figure 3.12 to completely crosslink the organic layer.

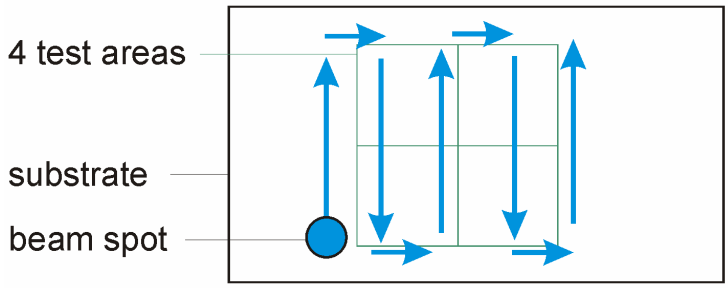

Figure 3.12: Scan of the substrate with a HeCd laser to crosslink the organic layer.

The laser itself was fixed so the sample was moved up and down and sidewards by a computer controlled x-y stage. Several scan cycles were required depending on the desired crosslinking dose and travelling speed.

3.2.9 Physical Vapour Deposition

Physical vapour deposition was used to apply the electron-transporting layer and the top electrode to the substrate. Before the deposition the organic layer was wiped away from the edges of the substrate with a dust free lens paper soaked in toluene. Then the substrate was put into the vacuum dome, which was situated in the glove box. The substrate was placed with the organic layer facing down into a holder. Under the holder there were different heating sources; a tungsten heating helix and two heating boats. Depending on the form of the material that should be deposited it was placed into a helix (wire) or in a boat (granules), see Figure 3.13.

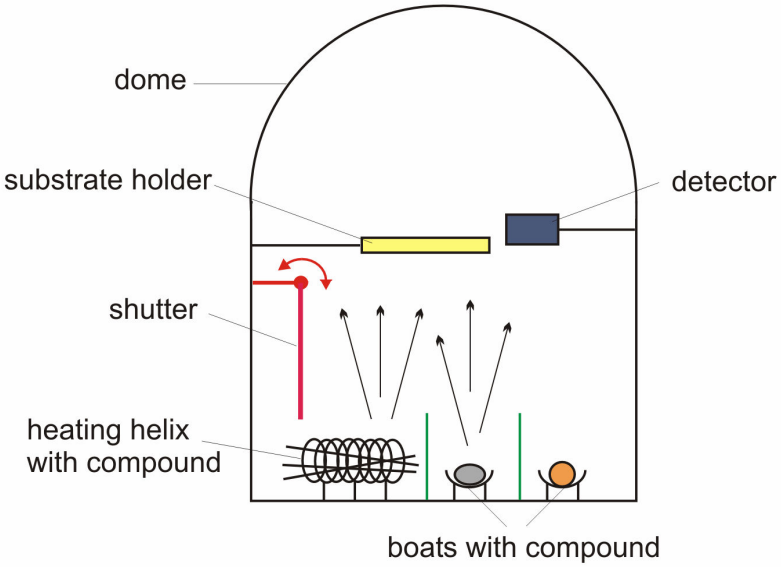

Figure 3.13: The set up for physical vapour deposition in a vacuumed dome. The desired compound for deposition is placed either in a boat or a helix, which is then heated to a high temperature. The material inside then evaporates and is deposited onto the substrate, which is lying face down in the substrate holder. Until the desired deposition rate is reached a shutter is placed between substrate and heating elements.

Under vacuum a helix or boat was then heated up until the material inside evaporated. A shutter was placed between substrates and heating elements to shield the substrate from any unwanted deposition. When the desired deposition rate, which was measured with a detector, was achieved the shutter was opened. Because of the heat the evaporated material moved towards the sample and condensed on the organic layer, building up a

new layer. This process could take from several seconds to some minutes, depending on the required layer thickness and the deposited material. As electron-transporting material 1,3,5-tri(phenyl-2-benzimidazolyl)benzene (TPBI) was used, which was made in-house, see Figure 3.14.

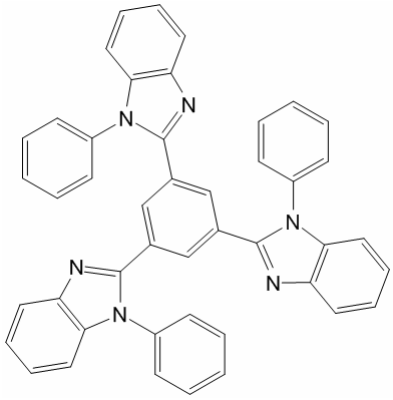

Figure 3.14: The chemical structure of the electron-transporting material TPBi.[77]

For TPBi a layer thickness between 100 - 150 Å and a deposition rate between 5 - 10 Å/s was used. A thin layer of lithium fluoride of 6 Å (0.2 Å/s) and a thicker aluminium layer of about 800 Å (30-50 Å/ s) were deposited sequentially as electrode. Between the depositions of the electrode layers the substrate was moved once for about 1 to 2 mm in its holder so that on one edge the aluminium directly contacted the ITO (see also Figure 3.8).

3.3 Device Testing

The devices were then tested in terms of luminance, CIE (1931) colour coordinates, emission spectrum, efficiency and current voltage characteristics. The set up is illustrated in Figure 3.15. The characterisation process was controlled by Labview. The OLED was connected to a power supply from Agilent (model E3631A), which applied an increasing voltage in 0.5 or 1 V steps. The voltage range differed for each experiment but lay usually between 1 and 14 V. For each step then the electroluminescence (EL) spectrum, current density and brightness were recorded.

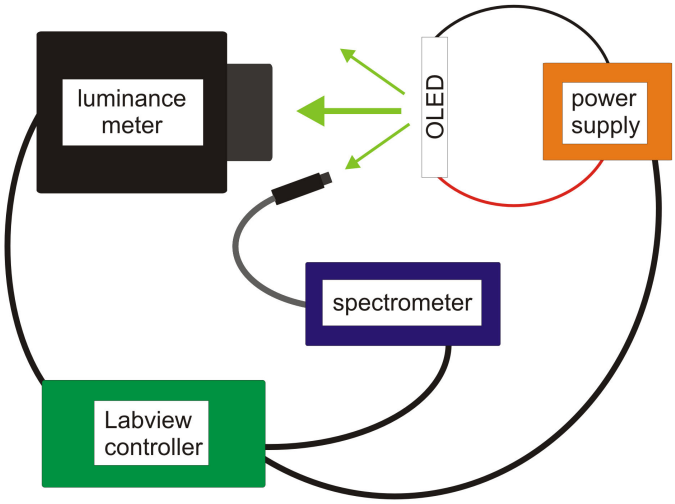

Figure 3.15: Set-up used to measure the current density, brightness and EL spectrum of an OLED for different voltages.

As fibre optic spectrometer the model AvaSpec-2048 (resolution: 2.4 nm, range: 200-1100 nm) from Avantes was used. The luminance was measured with a Minolta LS100 Luminance Meter, which measured over a circular area of 1.63 cm^2 (∅ = 14.4 mm) and had an acceptance angle of 1°. The meter was calibrated at the Minolta Company according to CIE standards. The device efficiency (cd A^{-1}) was obtained by dividing the measured luminance through the current density given from the power supply.

3.4 Simulation Parameters

Simulations on our light emitting liquid crystals LCs were carried out in cooperation with the Materia Nova research group from the Polytechnic Faculty of Mons and the University of Mons-Hainaut, in Mons, Belgium. Special thanks go to David Beljonne, Bernard Van Averbeke and Jérôme Cornil who supervised and supported this work. The work was split into two parts. The first was to consider single molecules and to determine their typical characteristics e.g. the absorption spectra. The second part concerns dimers built from these molecules and their different possible configurations. Further the interactions between the molecules in terms of their coupling strengths were investigated.

3.4.1 Modelling of Monomers

From the available Hull molecular structures, five were chosen to be modelled in the gas phase in terms of their highest occupied molecular orbital (HOMO) and lowest unoccupied molecular orbital (LUMO) energies, oscillator strengths and transition dipole densities as well as their absorption and emission spectra for vertical transitions. The five structures (MPA157, PV237, PV316, PV353, SPK382) were drawn with the AGUI^{TM} software.[78] The corresponding chemical structures are depicted in Chapter 4.1. For all five molecules the side and end chains were set to CH_3 and -OCH_3 respectively in the simulations.

First the molecular arrangement for each molecule in its ground state (GS) had to be modelled. Therefore each structure was plotted with different arrangements of fluorene and thiophene. The torsion angles were pre-optimised by the plotting tool of AGUI^{TM}. For the geometry optimisation the semiempirical Hartree-Fock Austin Model 1 (AM1) model was used to find the configuration with the lowest total energy.[45] The configuration that showed the lowest energy was then used to simulate transitions from GS to excited state (ES). It has to be considered that the model took only vertical transitions for one electron at a time into account. The movement of two electrons at the same time is too complicated to simulate in a short time. For the transitions semiempirical Hartree-Fock ZINDO/S.C.I. calculations were carried out on the optimised structure.[79, 80] With the help of the Zoa software (developed by J.P Calbert) [81] the outputs of the ZINDO simulations were processed to obtain values for the HOMO, LUMO energies, the absorption peak and the oscillator strengths for the GS.

For the transition from ES to GS first the ES had to be determined. Therefore the five GS files were taken and AM1 optimisations were carried out, but this time with varying values for the S.C.I. (single configuration interaction) parameters. After the calculation the simulated wavelength (nm) for the first transition (in Zoa referred to as E.S.#1) was noted. Afterwards the S.C.I. value was increased by 2 and the simulation run again. This loop was continued until the calculated wavelength varied by less than 1 nm. The corresponding S.C.I. value was then used for the ES simulation. Like for the GS, ZINDO/S.C.I. calculations were carried out to get the characteristics, e.g. emission spectra, for the ES of the molecules.

Note that for the calculations of the orbital energies simplified Hartree-Fock calculations were used, which do not take into account that an excitation does have an influence on the electron distribution (Koopman's Theorem). This assumption is very

severe and the energies for HOMO and LUMO are therefore highly overestimated, in general by a factor of two. The Zoa software takes this automatically into account so that absorption and emission energies are corrected accordingly. However the values for HOMO and LUMO levels presented later in the results section are the original overestimated ones obtained with ZINDO.

Optimised GS structures usually are slightly twisted in the gas phase. In thin films it is more likely that they twist less as they are confined in their movement by neighbouring molecules. To get a measure for the influence of the torsion angles (see Figure 3.16) on the energetic behaviour of our molecules the structures PV316 and PV353 were plotted with AGUI^{TM} with all torsion angles set to zero. On these straightened molecules AM1 optimisations followed by ZINDO/S.C.I calculations for the GS were then carried out.

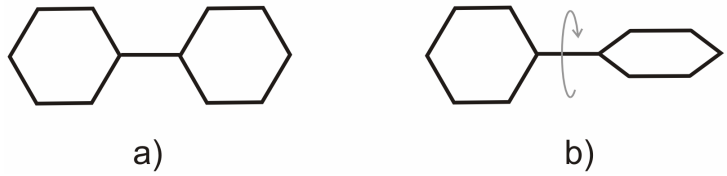

Figure 3.16: Torsion between two molecule units with a) no torsion b) torsion between the units.

The obtained absorption spectra, transition dipole densities and OSs were compared to those obtained with the twisted molecules. All simulations were carried out at a temperature of absolute zero and in the gas phase.

3.4.2 Modelling of Dimers

For the second part of this work the compounds PV316 and PV353 were chosen to determine the electronic coupling between two molecules in a dimer configuration. Three different types of interactions between the molecules were investigated; excitonic and the supermolecular coupling and the charge transfer integral. See Chapter 2.4.6 for further background information on coupling. To enable proper stacking, all torsional angles of the molecules were set to 0°. Thiophene and fluorene side chain conformations were arranged as is depicted in Figure 3.17 and Figure 3.18. The rearranged monomers were optimised with AM1 calculations and then stacked to build a dimer. On the dimers no further optimisations were carried out to avoid the distortion of the structures.

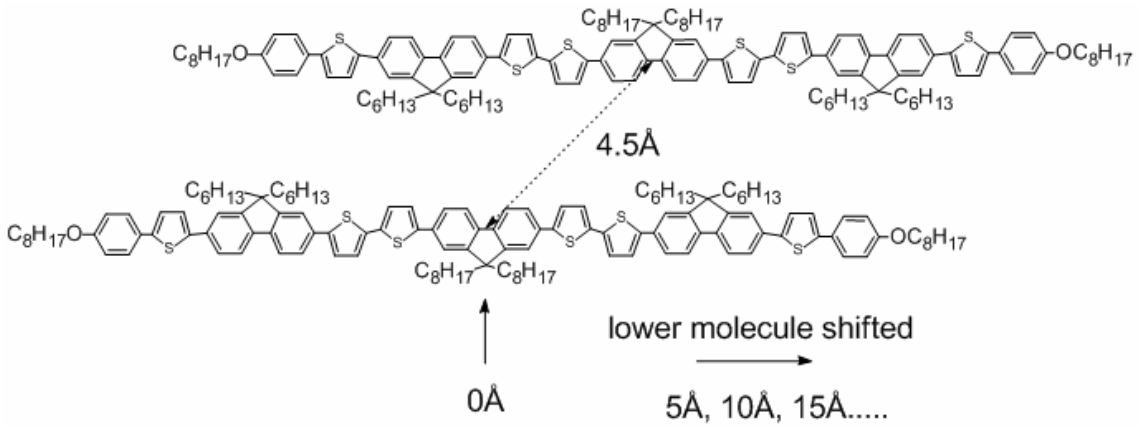

Figure 3.17: PV316 anti-cofacial dimer arrangement when shifted along another PV316 molecule. The side and end chains were replaced with CH_3 and -OCH3 respectively.

The molecules were rotated by 180° along their long axis (anti-cofacial configuration) when stacked to avoid the fluorene side chains combining with each other. The two molecules were separated by 4.5 Å. This value was obtained earlier through X-Ray measurements on a PV316 film.[82] One of the molecules was then shifted along the long axis of the other one in 5 Å steps. For each position ZINDO/S.C.I. calculations for the GS were carried out. ES state calculations were not considered as the GS results are already a good indication for the interaction strength between the two molecules.

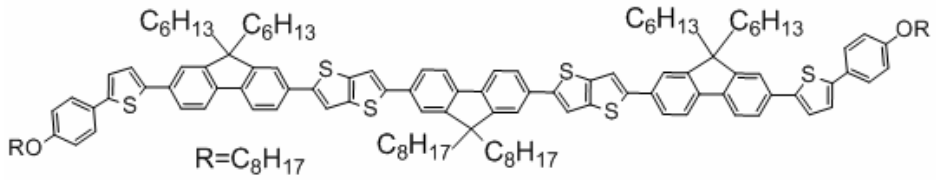

Figure 3.18: PV353 dimer arrangement. The side and end chains were replaced with CH_3 and -OCH3 respectively.

The PV353 was studied in the same arrangement. For the two dimers the OSs, transition wavelengths and energies as well as excitonic and supermolecular coupling and charge transfer integrals were simulated and plotted as function of longitudinal displacement. For the excitonic coupling a special ZINDO calculation was carried out, where the coupling value is directly obtained with Equation 2.12. For the supermolecular coupling ZINDO/S.C.I. calculations on the GS for the dimers were carried out. The GS simulation results were processed and visualised with the Zoa software. In Figure 3.19 a typical result window from Zoa is presented. In the right box different transitions (depicted as excited states E.S.#) consisting of several transitions from different HOMO to LUMO levels and their percental contribution to this state are shown. In theory the absorption spectrum is supposed to be a transition from HOMO to higher lying LUMO

levels, but because orbitals computed in ZINDO are close in energy, the simulated states HOMO-1, HOMO-2 etc contributions are introduced. The OS of each E.S. as well as the maximum absorption wavelength is listed behind the E.S. number.

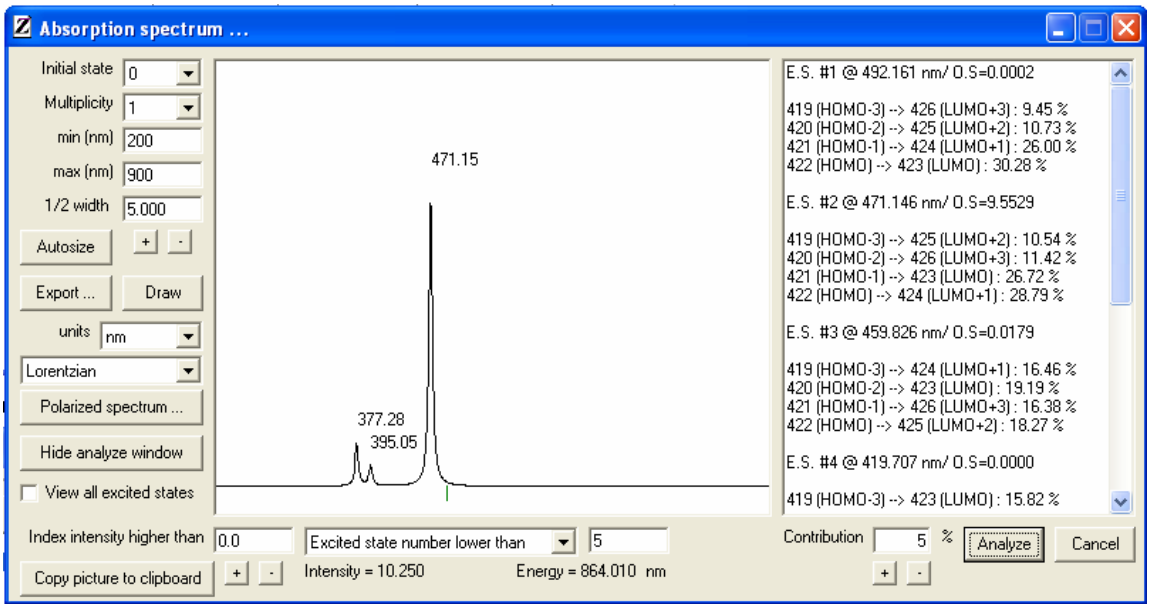

Figure 3.19: Exemplary result window in Zoa for a dimer in its GS. On the left maximum and minimum values for the scale of the absorption spectrum in the middle could be adjusted. Furthermore the x-axis units, linewitdh and shape like Gaussian or Lorentian could be changed. The right box shows the calculated OSs for the different excited states (E.S.) and their transition maxima in (nm). For each E.S. the HOMO to LUMO transitions and their percental contribution to that E.S. transition are listed.

To obtain a value for the coupling strengths, the energy values between two excited states (in general the two lowest) are subtracted from each other and then divided by two.[43] The two lowest optically allowed excited states have to be considered for this.[83] In the case illustrated in Figure 3.19, E.S.#1 is optically forbidden, because of the OS = 0.0002 so that half the energy difference between E.S.#2 and E.S.#3 is taken to obtain a value for the supermolecular coupling. The coupling values of the charge transfer integral were found using the method described by Van Vooren et al.[44] All obtained coupling values were then plotted against longitudinal shift in the PV316 and PV353 dimers.

A lateral shift of 1 and 2 Å was simulated with ZINDO/S.C.I. but no significant change in energy could be observed and hence was not further pursued. All simulations were carried out at temperature of absolute zero in the gas phase.

3.5 Surface Relief Grating Preparations

To find out whether the surface of our liquid crystal (LC) films is photopatternable they were crosslinked through a phase mask. Their surface was then investigated with an atomic force microscope (AFM) and an optical beam profiler. Furthermore polarised absorption spectra were recorded. The substrate preparation and measurement conditions will be presented in the following subchapters.

3.5.1 Substrate Preparation and Crosslinking

Sample preparation and exposure were carried out in a glove box under nitrogen atmosphere with humidity of less than 1 ppm and an oxygen concentration less than 30 ppm. Cleaned 25 x 25 mm^2 glass slides, covered with an about 40 nm thick PEDOT layer, were used as substrates. The PEDOT layer was necessary as the LC used did not form a uniform film on glass. More details on substrate cleaning and PEDOT application can be found in sections 3.2.1 and 3.2.4. LC films made of different thicknesses and concentrations were applied by spin–coating onto the glass/PEDOT substrates. Most measurements were carried out with the LC called PV237 but the compounds PV318 was also investigated. Over 20 different samples were tested. They were numbered S01, S02, S03 etc.. Those numbers will be referred to in the results chapter. An “H” behind the sample number indicates that the substrate was cured for a certain time after crosslinking and “W” that it was washed in toluene afterwards. With an optical beam profiler the thickness of a film prepared with the standard settings 900 rpm, 0.03 mg PV237 in 1 µl chlorobenzene was measured. The thickness was found to be 80 ± 5 nm. All other films made with 2000 rpm or an concentration of 0.02 mg/µl therefore were thinner as either their concentration was lower or the spin speed faster. After spin-coating all films were heated at 5°C/min to 65°C, where they were cured for 15 min and then cooled down to RT again with 5°C/min. Next the samples were crosslinked normally or through a phase mask. For further information on crosslinking see sections 2.2.6 and 3.2.8.

It has to be considered that an optical setup employing a phase mask is very delicate and is subject to the smallest vibrations or misalignment. Crosslinking had to be carried out under nitrogen atmosphere in a glove box to which pumps were connected, which caused a constant vibration of the box. During crosslinking the sample was moved by a xy-stage, which caused additional vibration. In the meantime the box was also used for

other purposes as the crosslinking process itself could last between 4 - 8 h depending on the area size to be crosslinked. This and the fact that the set up was handled wearing thick gloves a precise and stable optical setup was not realisable. A perfect mask alignment normal to beam direction was not realisable and possible reproducibility not ensured. The mask alignment was judged by eye with a probable error of ± 3°. The mask lay directly on top of the LC layer and they were additionally pressed together and attached to a hot stage with several screws. However it was not possible to judge by eye whether all screws were exactly fixed at the same height so that a wedge between substrate and mask might have been present.

Each substrate was divided into 4 areas of equal size as in Figure 3.20, to be able to examine different crosslinking settings on the same film. For absorption measurements the areas needed to be at least 10 mm x 10 mm large. If only AFM measurements were required smaller areas of a minimum of 5 mm x 5mm were sufficient.

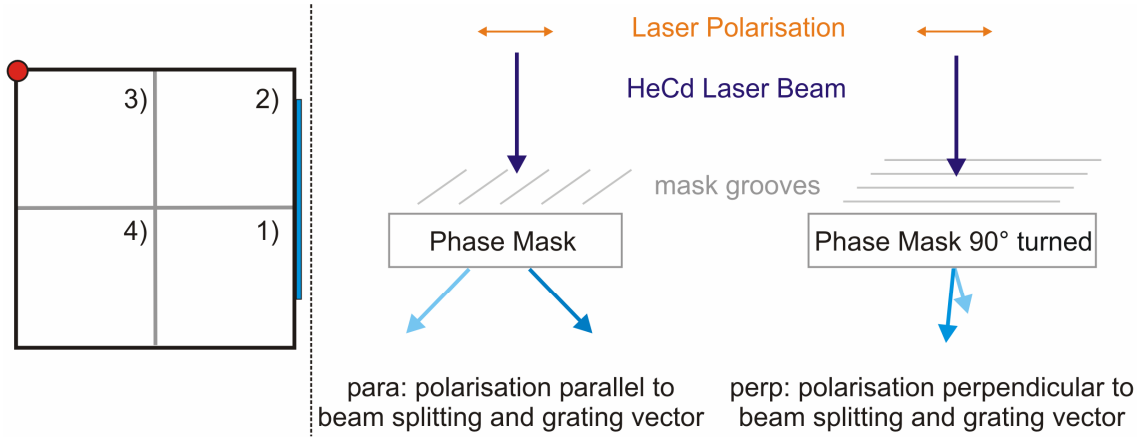

Figure 3.20: Substrate markings and divisions for AFM and absorption measurements and alignment of the phase mask in respect of the polarisation of the HeCd laser beam.

As a reference each substrate was marked with a dot in one corner and a line on the cut edge as indicated in Figure 3.20. The areas were either a) crosslinked, b) crosslinked through a phase mask of either 530 nm or 1 µm period or c) remained untreated = uncrosslinked. The phase masks split the initial beam into two beams of equal intensity. The alignment of the mask with respect to the polarisation direction of the HeCd laser affects the interference pattern behind the mask and was therefore noted as well. Here "para" refers to the splitting being parallel to the polarisation direction (or parallel to the grating vector, see section 2.6.4) and "perp" if the splitting was perpendicular to it, which occurred if the mask was turned by 90°. This definition will be used throughout this work.

A crosslinking energy of 600 J/cm^2 was required to render the films insoluble. The speed of the travelling xy-stage was kept between 0.48 – 0.52 mm/s. The laser power of the doughnut shaped beam (4 mm diameter) was measured before the crosslinking was started and varied between 52 - 53 mW. The mask's attenuation of the initial beam as well as the splitting into two beams were also considered in the fluence calculation. Crosslinking times were adapted accordingly so that all areas were crosslinked with at least 600 J/cm^2 or higher. The 530 nm phase mask (by Ibsen Photonics) was fabricated to match the wavelength of the HeCd laser. It was made out of fused silica and split the beam in 5 mW for the 0th order and 22 mW for – 1 and + 1 order respectively. For the fluence calculations 22 mW were used. In this case no higher orders were present.

The 1 μm mask's working wavelength was unknown, but was in the ultraviolet region. Hence the 0th order suppression was low for the 1 μm mask. With 52 mW initial laser power about 32 - 38 mW was measured for the 0th order and 5 mW for -1 and +1 order. In this case the crosslinking time was calculated with 32 mW as laser power to ensure that the layer would be fully crosslinked. There were also higher orders observable, but these could not be measured singly. They could however not have been strong as the total power measured directly behind the mask lay between 45 – 47mW.

The crosslinking tests were carried out at RT and 65°C with the LC PV237. The elevated temperature would ensure the compound being in a nematic state and gave the molecules more freedom to move due to the additional thermal energy. Tests with PV318 were carried out at the same temperature.

3.5.2 AFM Measurements

The surface of the films was investigated with an atomic force microscope (AFM) developed by Molecular Imaging now Agilent. The AFM used is a prototype so that no reference to type and model is possible. For general information on AFMs see Chapter 2.6.6. The surface measurements obtained with the AFM were then processed with the freeware program Gwyddion to obtain cross-sections, maximum roughness values and period parameters. In Figure 3.21 an example of how the cross-sections were measured with Gwyddion is shown.

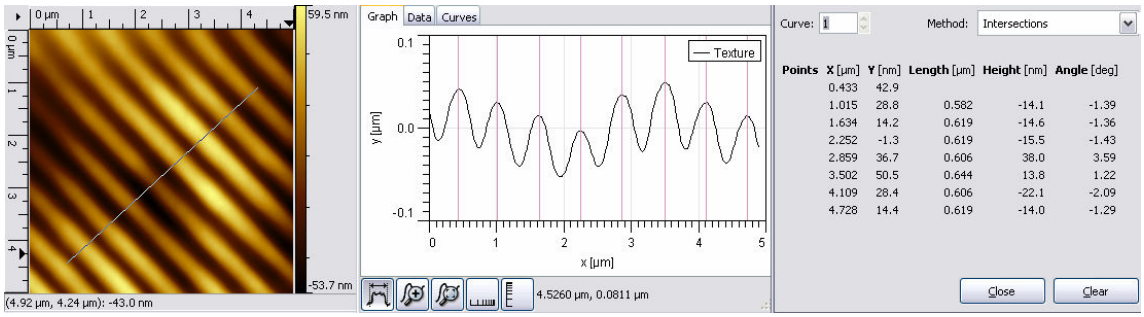

Figure 3.21: On the left an AFM scan viewed with Gwyddion is shown. The line indicates the cross-section, which is plotted in the graph in the middle. The vertical lines indicate where the data plotted in the right window was extracted.

The picture on the left shows the surface scan, the line across is plotted by hand. Therefore it could not be ensured that the cross-section was taken at exactly 90° to the corrugation. An error of ± 3° however has only a small influence on the period measured. For this deviation one obtains with trigonometry (x = 530 nm/cos 3°) 530.73 nm instead of 530 nm as period, which means that the error due to plotting is less than a 1 nm and is hence neglected. The cross-section indicated by the line is plotted in the graph in the middle. Gwyddion allows to extract data at self selected points, indicated by the vertical lines. The corrugation maxima were chosen to determine the periodicity. The distance between the lines is given as "Length [µm]" in the results window on the right. Since the corrugation peaks were not sharp there was a possible error, when determining the maximum. Moving the measurement line across the peak showed a deviation of ± 20 nm. This cannot be neglected but was minimised by taking the difference between several peaks to obtain an average. Furthermore the periods were taken form several cross-sections on one measurement area and then also from several areas on the same exposed film and the averaged again to obtain a reliable value. The ± error for the period (average) stated in the result section corresponds to half the difference between maximum and minimum period measured. The maximum amplitude (height difference between the highest and the lowest point on the cross-section) was determined by the Gwyddion program itself. When plotting the lines for the cross-section it was therefore taken care of that an area with no defects or holes in the LC film was measured. The 2D and 3D pictures of the surface presented in this work were made with the AFM control software (Picoscan) itself. The size of the measured areas varied between 2 µm x 2 µm and 5 µm x 5 µm with a scan speed between 300 - 1000 nm/s. The surface roughness could be measured down to an Angstrom.

3.5.3 Polarised Absorption Spectroscopy

Polarised absorption spectra of several crosslinked films were recorded. Therefore a polariser was introduced into the measurement beam of the Lambda40 spectrometer made by Perkin/Elmer. A clean glass substrate (25 x 25 mm^2) was used as a reference measurement. The PEDOT layer showed no polarisation dependence in previous absorption measurements and hence did not influence the results. Each area measured on the crosslinked films was about 8 x 8 mm^2. Once measured the area was turned by 90° and then measured again. The polarised absorption ratio was obtained by dividing the two spectra. The two measurements were repeated on different spots of the same area to ensure reproducibility.

4 Characterisation and Modelling of Liquid Crystals

In this chapter we report the transition temperatures and spectroscopic characterisation for the LCs used in this work. Further the modelled HOMO, LUMO and transition energies as well as the oscillator strengths in monomers and dimers are presented. Furthermore different coupling interactions in dimers in respect to longitudinal offsets are discussed.

4.1 Structures and Transition Temperatures

For reasons of convenience the compound names used within the University are also used in this work. The compound names are assembled from the initials of the creator and product numbers in chronological order. In Table 4.1 all investigated structures and their transition temperatures are presented in alphabetical order. The transition temperatures were measured with a differential scanning calorimetry (DSC) machine by Perkin/Elmer. See section 3.1.1 for information on the determination of the transition temperatures with DSC.

Table 4.1: Molecular structures and their transition structure.

Name	Structure	Temperature (°C)					
		Tg	Cr		N		I
AW01	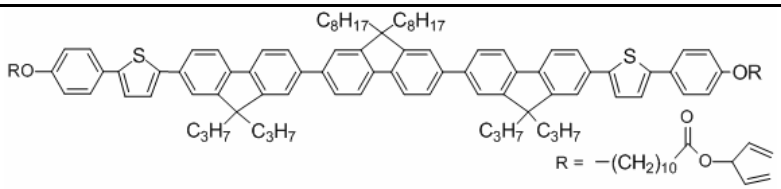	5		77		112	
GJR130	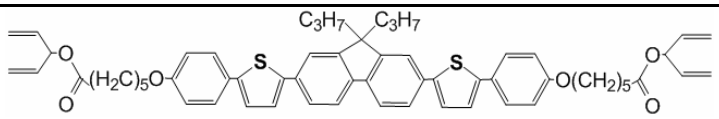	39		92		108	
MPA157	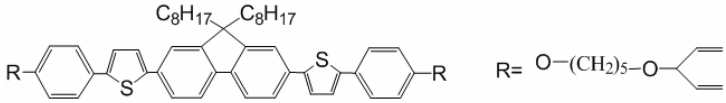	-25		97		44	
PV237	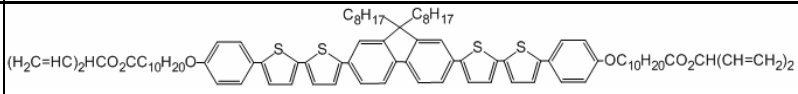	0		52		143	
PV316	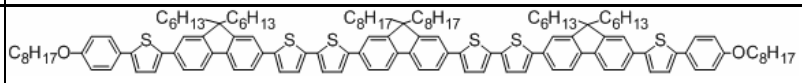	55				235	
PV318	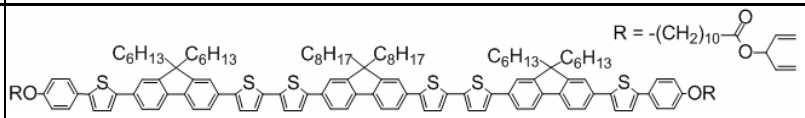	25				187	
PV353	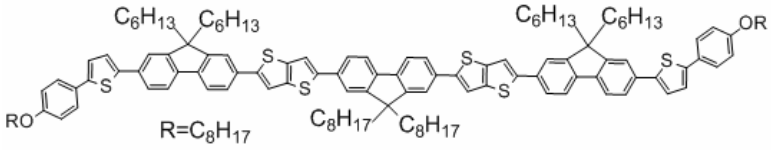	60		120		350	
SPK107	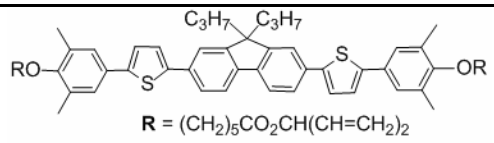	22		NA		30	
SPK146	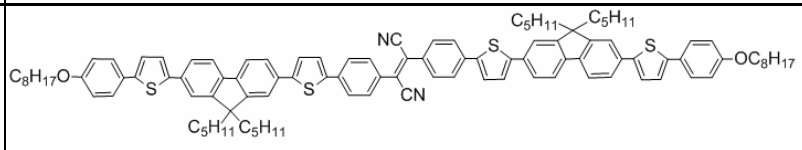	76		180		246	
SPK382	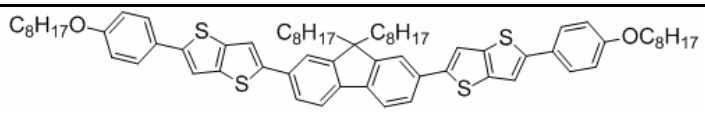	26		130		231	

The LC called SPK107 showed no measurable crystallisation point. Its nematic phase was also not clearly determinable with a polarisation microscope. Its low transition temperatures however made it an excellent candidate for mixtures to reduce the transition temperatures of other compounds. All other compounds showed a nematic phase.

4.2 Optical Quantum Efficiency Results

For most of the LCs presented in Table 4.1 the optical quantum efficiency (QE) in solution and solid state was measured using the methods discussed in sections 2.3 and 3.1.3. The efficiencies as well as the solvents used are stated in Table 4.2.

Table 4.2: Optical quantum efficiency results in solution and in the solid state (film).

Compound	Optical Quantum Efficiency (%)			
	Solution	Solvent	Film	Solvent
AW01	57 ± 0.7	toluene	22 ± 1.1	toluene
GJR130	71 ± 1.7	toluene	28 ± 1.1	tetrahydrofuran
MPA157			20 ± 0.9	tetrahydrofuran
PV237	33 ± 0.5	toluene	15 ± 0.3	toluene
PV316	48 ± 1.4	toluene	36 ± 2.5	tetrahydrofuran
PV318	39 ± 1	toluene	35 ± 0.8	tetrahydrofuran
PV353	67 ± 2.5	toluene	31 ± 3.5	toluene
SPK107			4 ± 0.5	toluene
SPK146	42 ± 1.3	toluene	4 ± 0.9	toluene
SPK382	71 ± 1.2	toluene	14 ± 0.6	toluene

The highest QE was observed for the GJR130 with 71 %. In the solid state however the efficiency decreased to 28 %. For films made with the polymer poly-(methoxy-5-(2'-ethyl)-hexyloxy-p-phenylenevinylene) also called MEH-PPV, values of about 10 % were reported.[31] In all cases the efficiencies in solution were greater than in solid state. This effect is also often observed in polymers, where aggregation leads to quenching due to interchain interactions.[84, 85] In section 4.4.2 we investigate this aggregation effect for some of our molecules with the help of semiempirical simulations on LCs in monomer (solution) and dimer (thin film) configurations.

4.3 Emission and Absorption Spectra

In this chapter all available spectra from the compounds investigated are presented. Absorption spectra were recorded in the solid state (film) as well as in solution using the methods described in 3.1.2. The emission was measured as electroluminescence (EL) from an OLED and as photoluminescence (PL) in solution or thin film. The PL spectra were recorded using an integrating sphere (see section 3.1.3) with a 406 nm laser diode as excitation source. Further information on the processing conditions is given in Chapter 3.1.2.

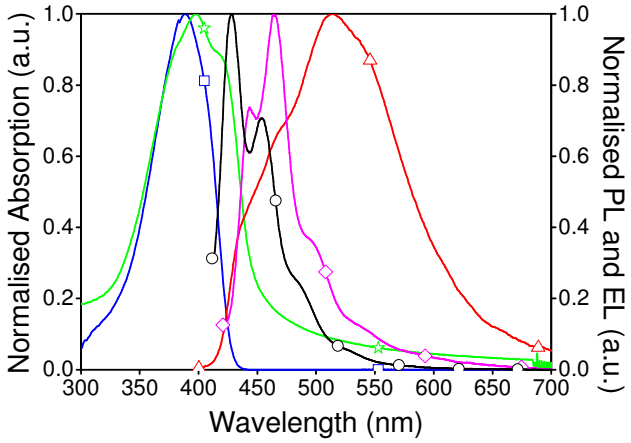

Figure 4.1: Absorption and emission spectra of toluene films and solutions made with the compound AW01. Absorbance in solution (blue squares) and in thin film (green stars). PL in solution (black circles) and in thin film (pink rhombi). EL in thin film (red triangles).

For AW01 the absorption maximum in solution lies at 388 nm in thin film at 397 nm. The PL maxima lie at 428 nm in solution and 464 nm in thin film. On the first run of the OLED the EL maximum lies in the blue/green region at 466 nm but shifts with running time to 513 nm.

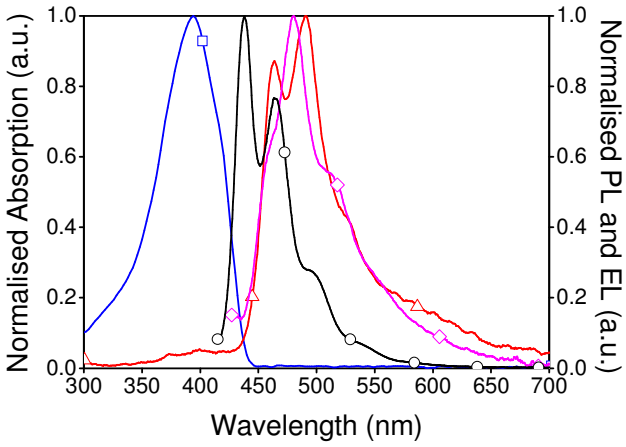

Figure 4.2: Absorption and emission spectra of toluene films and solutions made with the compound GJR130. Absorbance in solution (blue squares). PL in solution (black circles) and in thin film (pink rhombi). EL in thin film (red triangles).

For GJR130 the absorption maximum in solution lies at 393 nm. The PL maxima lie at 480 nm in solution and 438 nm in thin film. The EL maximum lies at 490 nm.

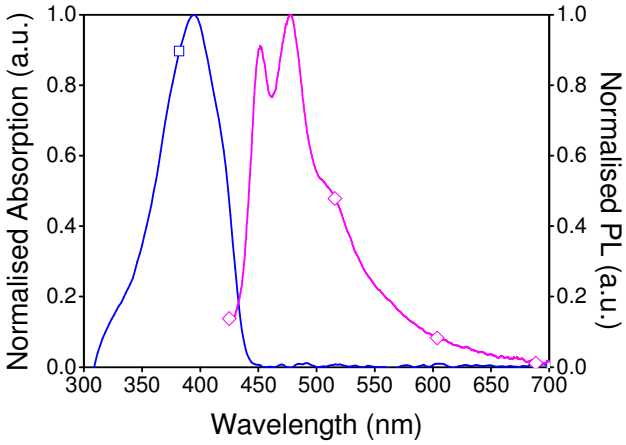

Figure 4.3: Absorption spectrum of a toluene solution (blue squares) and PL emission spectrum (pink rhombi) of tetrahydrofuran film and made with the compound MPA157.

For MPA157 the absorption maximum in solution lies at 394 nm. The PL maximum in thin film lies at 477 nm.

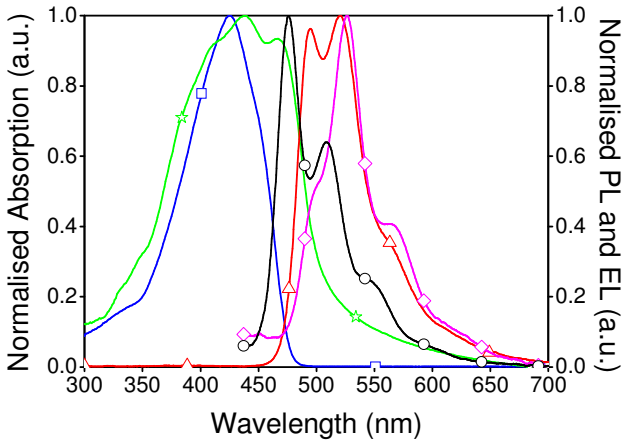

Figure 4.4: Absorption and emission spectra of toluene films and solutions made with the compound PV237. Absorbance in solution (blue squares) and in thin film (green stars). PL in solution (black circles) and in thin film (pink rhombi). EL in thin film (red triangles).

For PV237 the absorption maximum in solution lies at 425 nm in thin film at 438 nm. The PL maxima lie at 475 nm in solution and 526 nm in thin film. The EL maximum lies at 520 nm.

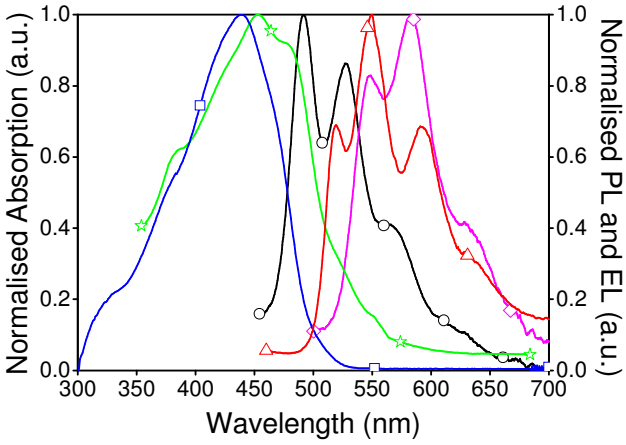

Figure 4.5: Absorption and emission spectra of toluene films and solutions made with the compound PV316. Absorbance in solution (blue squares) and in thin film (green stars). PL in solution (black circles) and in thin film (pink rhombi). EL in thin film (red triangles).

For PV316 the absorption maximum in solution lies at 438 nm in thin film at 453 nm. The PL maxima lie at 549 nm in solution and 491 nm in thin film. The EL maximum lies at 583 nm.

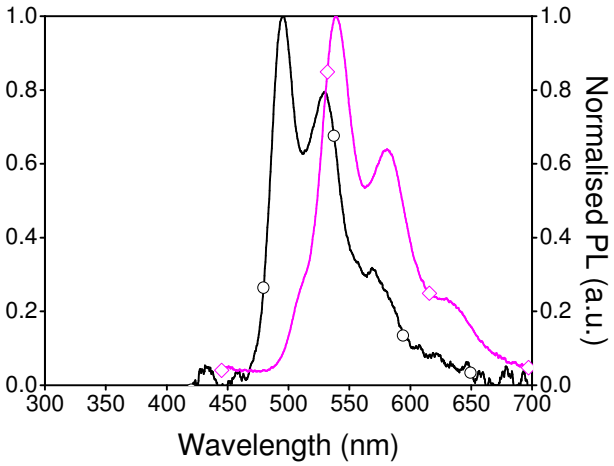

Figure 4.6: PL emission spectrum (pink rhombi) of a tetrahydrofuran film and of a toluene solution (black circles) made with the compound PV318.

For PV318 the PL maximum in solution lies at 495 nm and at 539 nm in thin film.

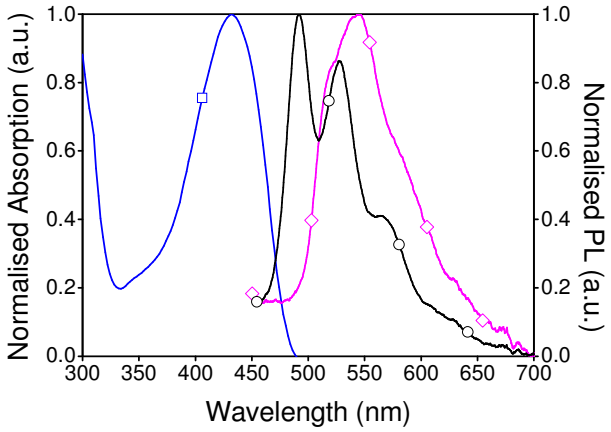

Figure 4.7: Absorption and emission spectra of toluene films and solutions made with the compound PV353. Absorbance in solution (blue squares). PL in solution (black circles) and in thin film (pink rhombi).

For PV353 the absorption maximum in solution lies at 432 nm. The PL maxima lie at 491 nm in solution and about 543 nm in thin film.

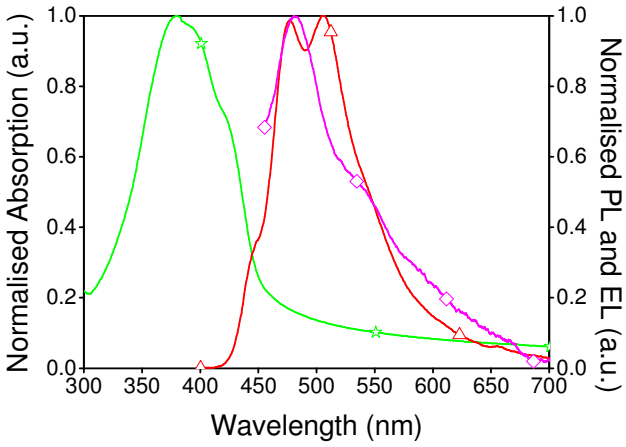

Figure 4.8: Absorption and emission spectra of toluene films and solutions made with the compound SPK107. Absorbance in thin film (green stars). PL in thin film (pink rhombi). EL in thin film (red triangles).

For SPK107 the absorption maximum in thin film lies at 380 nm. The PL maxima lie at 481 nm in thin film. The two EL maxima lie at 476 and 506 nm.

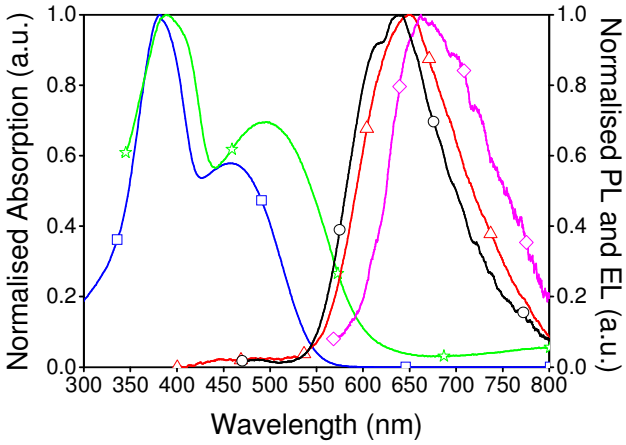

Figure 4.9: Absorption and emission spectra of toluene films and solutions made with the compound SPK146. Absorbance in solution (blue squares) and in thin film (green stars). PL in solution (black circles) and in thin film (pink rhombi). EL in thin film (red triangles).

For SPK146 the absorption maximum in solution lies at 381 nm in thin film at 389 nm. The PL maxima lie at 638 nm in solution and about 665 nm in thin film. The EL maximum lies at 648 nm.

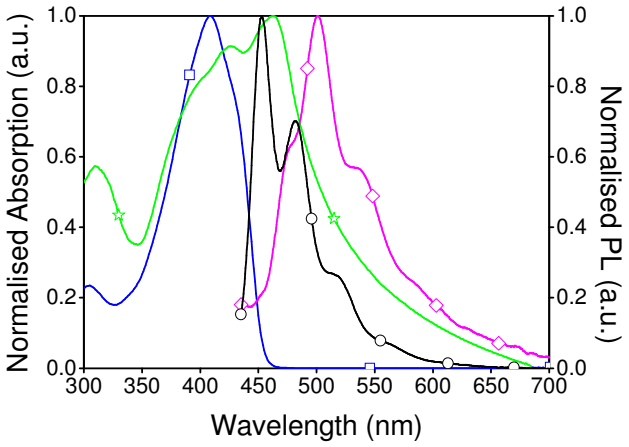

Figure 4.10: Absorption and emission spectra of toluene films and solutions made with the compound SPK382. Absorbance in solution (blue squares) and in thin film (green stars). PL in solution (black circles) and in thin film (pink rhombi).

For SPK382 the absorption maximum in solution lies at 408 nm in thin film at 462 nm. The PL maxima lie at 451 nm in solution and 500 nm in thin film. In general the maxima for thin films are red shifted in respect to the maxima obtained with solutions. This effect is well known for organic materials and might originate e.g. from the planarisation of the backbone or due to molecular interactions due to aggregation.[86] Also the absence of the solvent in the solid state, due to the substrate heating above the solvent's boiling point during film preparation, must be considered. Solvents usually have higher dielectric constants. The latter influences the potential energy of a system, see Chapter 2.5.4 and thus the energy of the levels involved in the emission and absorption transitions.

4.4 Simulation of Molecules

In cooperation with the Materia Nova research group, which was established in 1995 by the Polytechnic Faculty of Mons and the University of Mons-Hainaut, in Mons, Belgium simulations on our light emitting liquid crystals LCs were carried out. Special thanks go to David Beljonne, Bernard Van Averbeke and Jérôme Cornil who supervised and supported this work.

The work was split into two parts. The first was to consider single molecules and to determine their typical characteristics e.g. the absorption spectra to compare them to experimental results. The second part concerns dimers built from these molecules and

their different possible configurations. Here the interactions between the molecules in terms of their coupling strengths were investigated.

4.4.1 Monomer Characterisation

The molecules MPA157, PV237, PV316, PV353 and SPK382 were modelled in the gas phase to calculate their highest occupied molecular orbital (HOMO) and lowest unoccupied molecular orbital (LUMO) levels, oscillator strengths (OS) and transition dipole densities as well as their absorption and emission spectra for vertical transitions. For more information on transition dipoles and OSs see section 2.5.5. The chemical structures of the five molecules can be found in section 4.1. Side and end chains were set to CH_3 and -OCH_3 respectively for the simulations. It has to be considered that the software optimised structures were not as flat as depicted in the schematic drawings. The molecular conformations and the corresponding torsion angles will be discussed later in this chapter. In Table 4.3 the obtained energies for the five structures in their ground state (GS) and excited state (ES) as well as their absorption and emission peaks and corresponding oscillator strength are summarised. From the GS configuration one can obtain information about the absorption transition from GS to ES, from the ES configuration information about emissive transitions, hence from ES to GS.

It is stressed again that the obtained energies for HOMO and LUMO are overestimated by a factor of about two. The Zoa software corrected absorption and emission energies accordingly. However the values for HOMO and LUMO levels given in Table 4.3 are the original overestimated ones.

Table 4.3: Energies and oscillator strengths for the five compounds in the gas phase. Only vertical transitions were taken into account. Note that the absorption and emission energies are about half the difference between HOMO and LUMO.

Compound	State	HOMO (eV)	LUMO (eV)	Max Energy in Absorption (GS) or Emission (ES) (eV)	Max.Wavelength In Absorption (GS) or Emission (ES) (nm)	Oscillator Strength
MPA157	GS	-6.690	-0.547	3.099	400	2.4578
	ES	-6.386	-0.876	2.652	468	2.6297
PV237	GS	-6.495	-0.753	2.770	448	3.0735
	ES	-6.149	-1.088	2.339	530	3.3018
PV316	GS	-6.407	-0.854	2.636	470	4.3155
	ES	-6.131	-1.168	2.229	556	3.9029
PV353	GS	-6.410	-0.768	2.704	459	4.0166
	ES	-6.170	-1.061	2.333	532	4.0137
SPK382	GS	-6.475	-0.695	2.804	442	2.7806
	ES	-6.216	-1.000	2.421	512	3.0005

For the compound MPA157 the absorption maximum lies at 400 nm or equivalently at 3.099 eV. The OS of the absorption is 2.4578 and the HOMO and LUMO levels in the GS lie at -6.690 and -0.547 respectively. The OS for the ES is larger than for the GS, which means that the emissive transition is stronger and more likely to take place than the absorption transition. OS values usually do not exceed the value of "1".[51] The larger values obtained therefore might also be due to the overestimation of the HOMO and LUMO energies or the absence of a surrounding medium. The values obtained however can still be compared with each other as the same algorithm was used. In Figure 4.11 the oscillator strengths for GS and ES from Table 4.3 are plotted for better comparison.

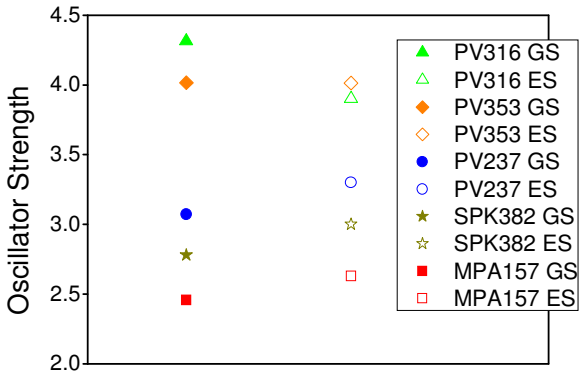

Figure 4.11: Oscillator strengths for the twisted optimised molecules in a gas phase for transitions from the ground state (GS) and excited state (ES).

It is interesting that the OS is increasing with molecule length as MPA157 is the shortest and PV316 the longest molecule. For the three shorter LCs (MPA157 < SPK382 < PV237) the ES oscillator strengths are as high as the values for the GS. For the two longer molecules (PV353 < PV316) the opposite result is observed.

With the visualisation software Zoa we were able to plot the p-orbitals of the HOMO and LUMO levels in the GS and ES. The result for the GS of MPA157 is shown in Figure 4.12.

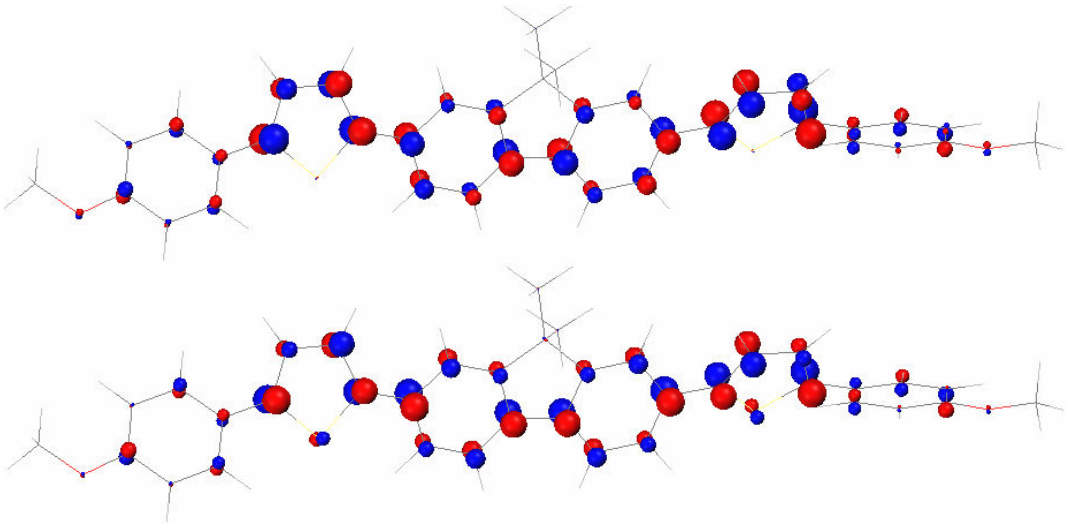

Figure 4.12: The p-orbitals of the modelled compound MPA147 in the GS. The picture above shows the HOMO and the picture below the LUMO level. The colour of the spheres indicates the sign of the wavefunction of the orbital.

This representation however is not very practical as the interaction between HOMO and LUMO level is not directly apparent. Therefore the transition dipole densities, corresponding to the strength of a transition between the orbitals, of the HOMO and

LUMO level are plotted. The transitions with the highest OS from HOMO to LUMO for GS and from LUMO to HOMO in the ES are plotted, see Figure 4.13 to Figure 4.22. The size of the spheres is representative of the strength of a transition dipole from HOMO to LUMO level. In the figures red represents a positive and blue a negative sign of the dipoles. The sphere sizes are not to be scaled when comparing different pictures.

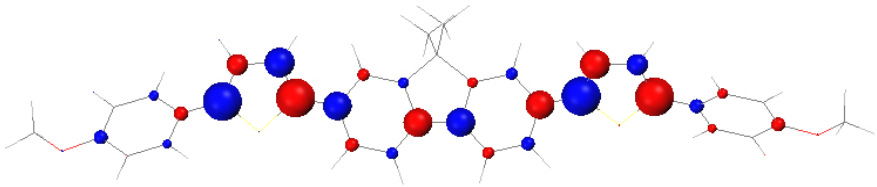

Figure 4.13: MPA157 transition dipole densities, GS.

Figure 4.13 shows the distribution of the resultant transition dipole densities in the GS from the two orbital plots of the HOMO and LUMO level in Figure 4.12. In Figure 4.14 the densities obtained for the transitions between the orbitals of the LUMO and HOMO plot of the ES (analogue to Figure 4.12) are shown.

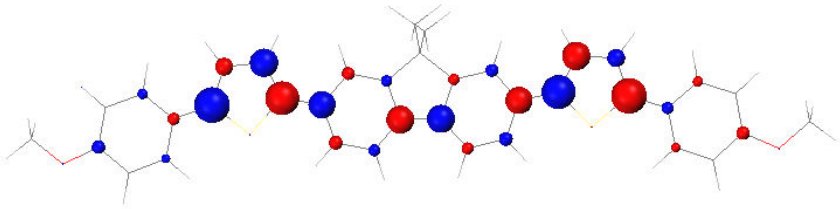

Figure 4.14: MPA157 transition dipole densities, ES.

The transition dipole densities are concentrated on the thiophenes and the fluorenes. This is valid for both configurations GS and ES. Hence the charges involved in absorption and emission processes can be found mainly on these units.

Furthermore the torsion angles on the optimised structures between benzene, thiophene and fluorene units were measured, see Table 4.4 to Table 4.8. The angle was measured between 4 atoms on the molecule. The starting point was always the sulphur on a thiophene and the end point a carbon atom three steps away going either clockwise or anti-clockwise.

Table 4.4: MPA157 torsion angles.

Compound	State	Benzene-Thiophene	Thiophene-Fluorene	Fluorene-Thiophene	Thiophene-Benzene
MPA157	GS	26.79°	25.59°	25.61°	26.67°
	ES	0.10°	0.18°	0.19°	0.09°

It is striking that in the GS all torsion angles lie around 25° but in the ES they are all close to 0°. This is a good indication of how different the molecular conformation of ground and excited states can be. A large difference in nuclear conformation means also a large Stokes shift, see section 2.5.1. This explains the difference in the modelled absorption and emission peaks presented in Table 4.3.

In Figure 4.15 and Figure 4.16 the transition dipole densities of PV237 for GS and ES are plotted. The measured torsion angles are listed in Table 4.5.

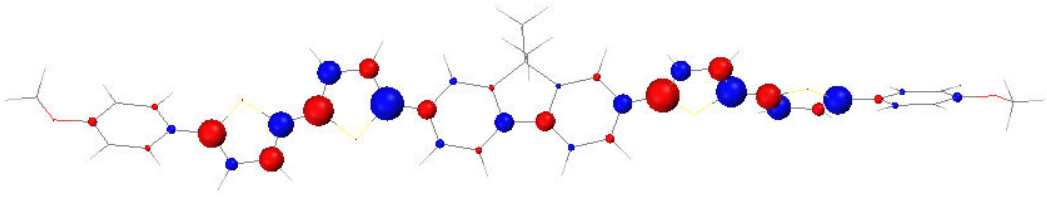

Figure 4.15: PV237 transition dipole densities, GS.

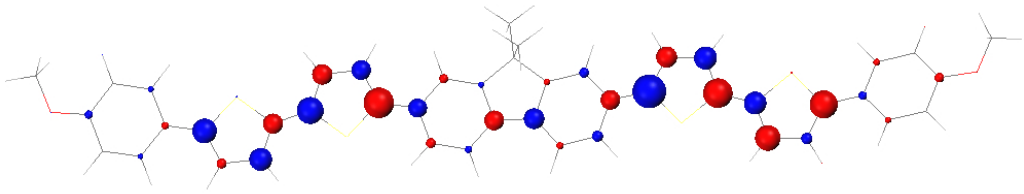

Figure 4.16 PV237 transition dipole densities, ES.

As in the case of MPA157, HOMO to LUMO transitions and vice versa mainly take place on the thiophene and fluorene units. The torsion angles however do not all become close to zero in the ES. They change by about 13- 16° between the GS and ES for the outer rings compared to a 26° change to zero in the centre. Hence the nuclear conformation on the outer parts changes less than in the middle of the molecule during a transition.

Table 4.5: PV237 torsion angles.

Compound	State	Benzene-Thiophene	Thiophene-Thiophene	Thiophene-Fluorene	Fluorene-Thiophene	Thiophene-Thiophene	Thiophene-Benzene
PV237	GS	27.53°	25.63°	26.40°	26.11°	25.40°	27.37°
	ES	14.31°	0.80°	0.07°	0.07°	0.43°	11.03°

This shows that the end parts of the PV237 molecule contribute less to the charge transfer than the centre.

In Figure 4.17 and Figure 4.18 the transition dipole densities for GS and ES of PV316 are plotted.

Figure 4.17: PV316 transition dipole densities, GS.

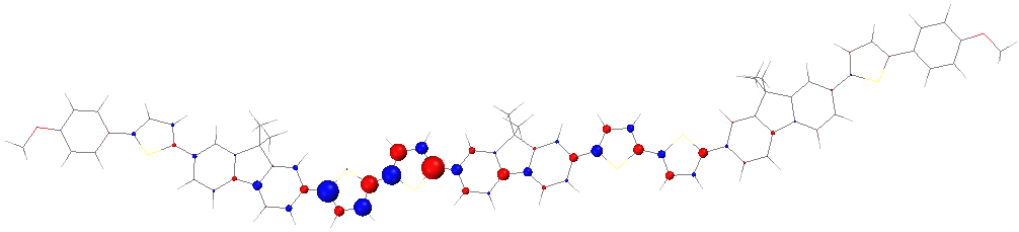

Figure 4.18: PV316 transition dipole densities, ES.

Unlike the MPA157 and PV237 cases the transition densities are not symmetrically distributed. This is probably due to slight bond variations, which favour one side of the molecule. This asymmetric distribution does not affect other simulated values like OS and transition energies and is therefore not considered any further. It is however notable that most of the charge transfer takes place on the thiophene units. The outer fluorenes show only small densities (spheres). The asymmetry is also mirrored in the asymmetric change of the torsion angles when going from GS to ES, see Table 4.6.

Table 4.6: PV316 torsion angles.

Compound	State	Benz.-Thio.	Thio.-Fluor.	Fluor.-Thio.	Thio.-Thio.	Thio.-Fluor.	Fluor.-Thio.	Thio.-Thio.	Thio.-Fluor.	Fluor.-Thio.	Thio.-Benz.
PV316	GS	27.16°	25.86°	25.39°	5.32°	26.36°	26.17°	22.10°	25.25°	25.72°	26.85°
	ES	23.64°	19.44°	0.10°	0.15°	0.10°	0.64°	0.04°	17.82°	25.08°	24.56°

The outer angles change about 4- 12° and the charge transfer in concentrated in the centre of the molecule In Figure 4.19 and Figure 4.20 the transition dipole densities for GS and ES on the PV353 molecule are plotted.

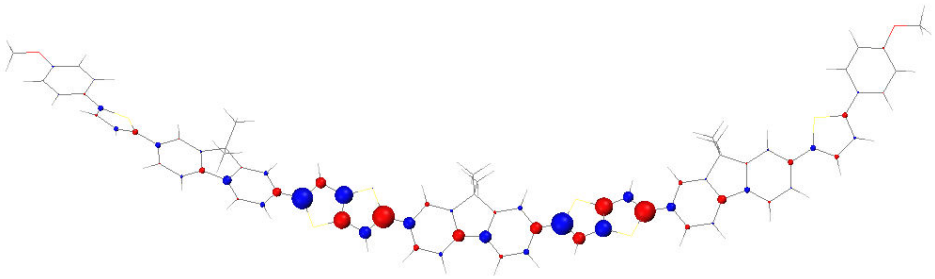

Figure 4.19: PV353 transition dipole densities, GS.

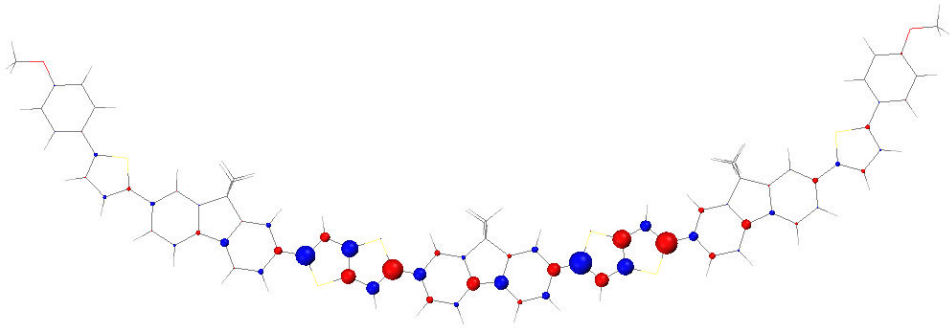

Figure 4.20: PV353 transition dipole densities, ES.

The banana shape of the optimised structure is not very realistic as the side chains on the fluorenes would rather repell than attract each other. However this configuration showed the lowest potential energy in the GS and was therefore not abandoned. The transition densities are distributed symmetrically and like for PV316 the greatest transition densities are mainly found on the thiophenes. The torsion angles listed in Table 4.7 also show symmetric behaviour.

Table 4.7: PV353 torsion angles.

Compound	State	Benzene-Thioph.	Thioph.-Fluorene	Fluorene-Thioph.	Thioph.-Fluorene	Fluorene-Thioph.	Thioph.-Fluorene	Fluorene-Thioph.	Thioph.-Benzene
PV353	GS	26.34°	24.91°	27.19°	26.17°	25.16°	27.50°	24.63°	25.83°
	ES	22.01°	18.20°	0.99°	0.38°	0.08°	0.61°	14.09°	21.48°

For the centre part between the thiophenes the angles change by about 25 – 27° when going from GS to ES. The outer angles change by only about 4- 10°. The transition dipole densities of GS and ES for SPK382 are shown in Figure 4.21 and Figure 4.22.

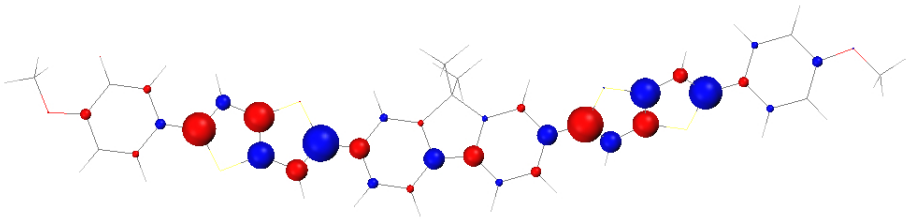

Figure 4.21: SPK382 transition dipole densities, GS.

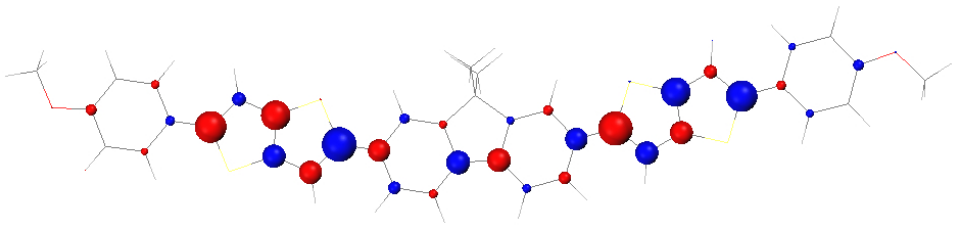

Figure 4.22: SPK382 transition dipole densities, ES.

As for the other molecules the strongest transitions can be found on the thiophenes and the centre fluorene. The molecule is much shorter than PV316 and PV353 so that the ends are closer to the fused thiophenes and hence are more involved in the charge transfer. This is mirrored in the change of torsion angle, see Table 4.8.

Table 4.8: SPK382 torsion angles.

Compound	State	Benzene-Thiophene	Thiophene-Fluorene	Fluorene-Thiophene	Thiophene-Benzene
SPK382	GS	27.02°	25.80°	26.25°	28.07°
	ES	6.40°	0.30°	0.43°	7.64°

The outer angles change about 20° compared to the angles in the centre which change about 25 – 26°. This difference is not very large so almost the whole molecule is in

involved in the transfer processes. So in general one can say that the highest transition dipole densities are situated on the thiophenes. Except for PV316 all densities are symmetric in their strength but not in their sign. For all molecules the states are fully delocalised as the transition densities are spread along the backbone.

For comparison the experimental absorption and photoluminescence (PL) spectra from the five compounds in toluene solution as well as their simulated spectra are presented in Figure 4.23 and Figure 4.24. A Lorentian shape with a small half width was chosen to represent the simulated absorption and emission peaks, though in reality the spectra are much broader. Further broadening was not included to facilitate distinction between experimental and modelled spectra.

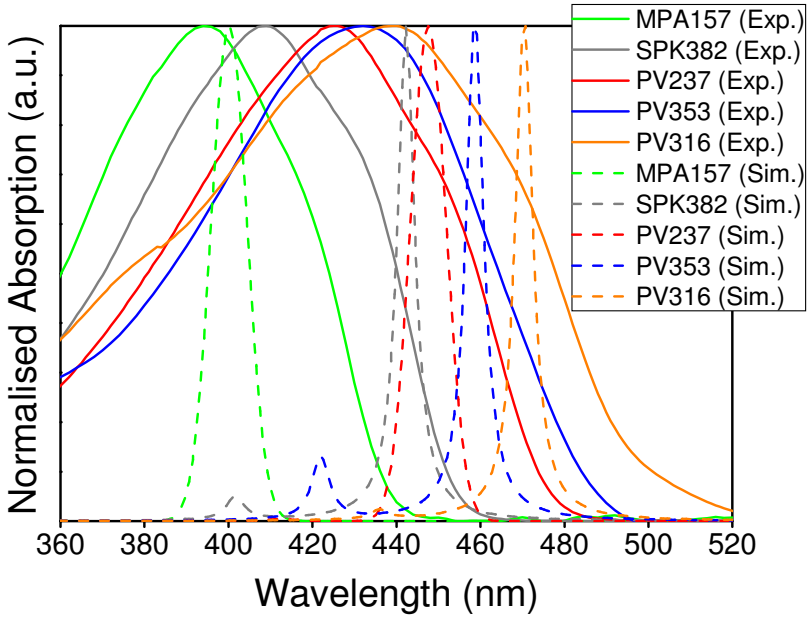

Figure 4.23: Experimental absorption spectra of the compounds in a toluene solution as well as the simulated absorption spectra (dashed lines). The small width of the simulated spectra is due to the arbitrary fit that was chosen when plotting the data.

In general one can say that the absorption spectra of organic molecules experience a bathocromic shift (bandgap decreases) with increasing chain length.[87] This trend was also observed for both experimental and simulated data for our LCs. Apart from the results for MPA157, experimental and simulated absorption peaks differ by about 40 nm from each other. This is not surprising as already mentioned; simplified HF was used, which overestimates the HOMO and LUMO energies. Furthermore the molecules were simulated in a gas phase at 0 K, hence thermal vibrations and solvent influences were not considered. The spectra however are still a good indication that the simulated

results are not very far off so that further investigations like dimer configurations can be made on the basis of this first optimisation. The simulated and experimental photoluminescence (PL) emission spectra are shown in Figure 4.24.

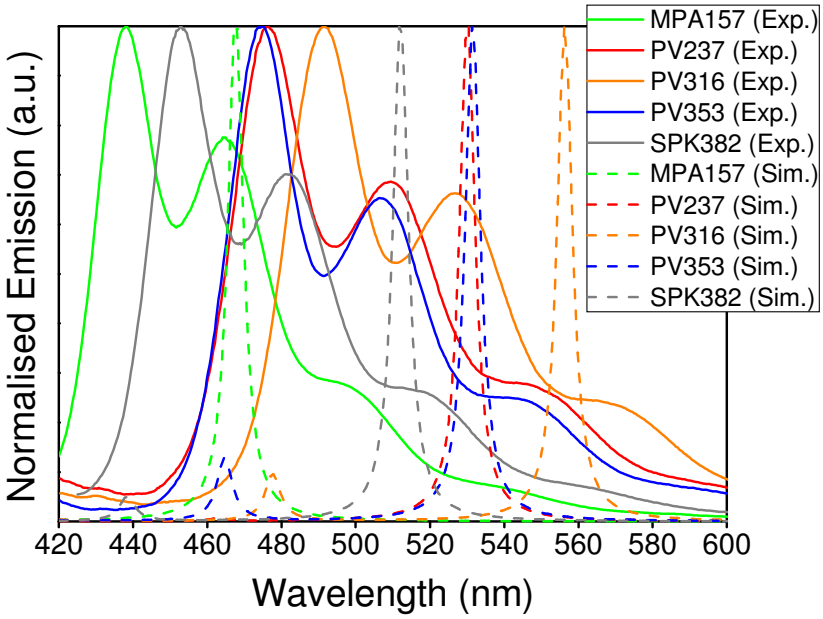

Figure 4.24 Experimental photoluminescence (PL) emission spectra of the compounds in a toluene solution compared to the simulated and later broadened emission spectra of the five compounds in a gas phase (dashed lines). For MPA157 no experimental PL spectrum in solution was available and a spectrum of GJR130, which has the same chromophore core, was plotted instead.

As was observed in absorption, the emission peak moves to longer wavelengths with increasing chain length. The experimental and simulated Stokes shift was calculated for each molecule; see Table 4.9. From the absorption the maximum peak and from the emission the central peak, both corresponding to the 0-1 transition, are used to calculate the Stokes shift. For further information on the Stokes shift and the comparability of simulated and experimental values see Chapters 2.5.1 and 2.5.2.

Table 4.9: Experimental and simulated absorption and emission peaks and the calculated Stoke shifts for the compounds in solution (exp.) or in gas phase (sim.). Note that for the experimental PL peaks the centre peak and not the PL maximum was considered.

Compound	Experimental Central Peak (nm)		Simulated Peak (nm)		Experimental Stokes Shift (nm)	Simulated Stokes Shift (nm)
	Absorption	Emission	Absorption	Emission		
MPA157	394	464	400	467	70	67
PV237	425	509	447	530	84	83
PV316	439	526	470	556	87	86
PV353	432	507	458	531	75	73
SPK382	409	481	442	512	72	70

The experimental and simulated Stokes shifts agree with each other within 3 nm. In Figure 4.25 the simulated absorption spectra of the PV316 and PV353 molecules in the twisted and the straightened configuration are shown.

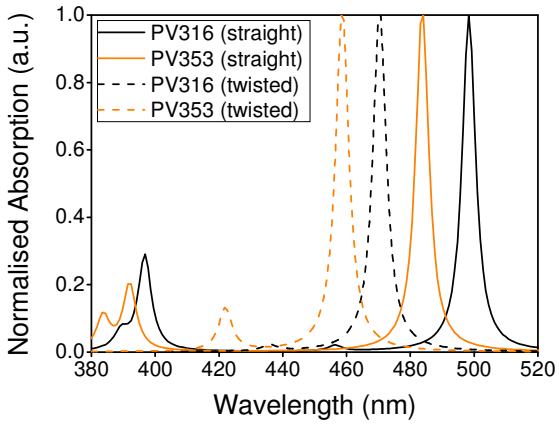

Figure 4.25: Comparison of the absorption spectra of PV316 and PV353 for the optimised twisted and the straight molecule, where all torsion angles were set to 0°.

The absorption spectra of the straightened molecules are red shifted; 28 nm for PV316 and 26 nm for PV353. In the straightened molecules the interaction of the atoms with each other is different as in the twisted configuration; hence the orbital overlap is not the same. This affects the HOMO and LUMO energies (similar as when going from monomer to dimer, see Figure 2.24) and thus the absorption wavelength. For comparison the simulated characteristics values for both twisted and straightened PV316 and PV353 molecules are listed in Table 4.10.

Table 4.10: Simulated values for twisted and straightened structures in their GS.

Compound	State	HOMO (eV)	LUMO (eV)	Peak Absorption Energy (eV)	Peak Absorption Wavelength (nm)	Oscillator Strength
PV316 straight	GS	-6.314	-0.975	2.488	498	4.4753
PV353 straight	GS	-6.331	-0.894	2.563	483	4.5099
PV316 twisted	GS	-6.407	-0.854	2.636	470	4.3155
PV353 twisted	GS	-6.410	-0.768	2.704	459	4.0166

Beside the red shift, which is mirrored in the lower energy values, a slightly higher OS is observed, which would mean that the flat configuration is favourable in terms of efficiency. The reason for these differences might also be due to the fact that the outer fluorene units are rotated about 180° for this simulation to correct for e.g. the banana shape of PV353 in Figure 4.19. The new configuration is displayed in Figure 4.26 and Figure 4.27 where the transition dipole densities for PV316 and PV353 respectively are shown.

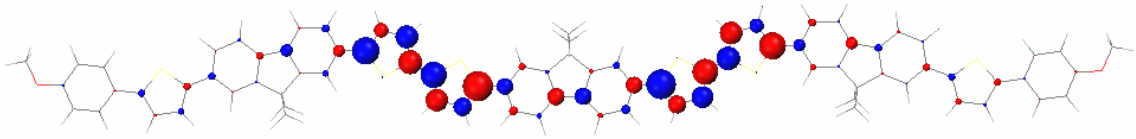

Figure 4.26: Transition dipole densities for the straightened PV316 molecule in its GS.

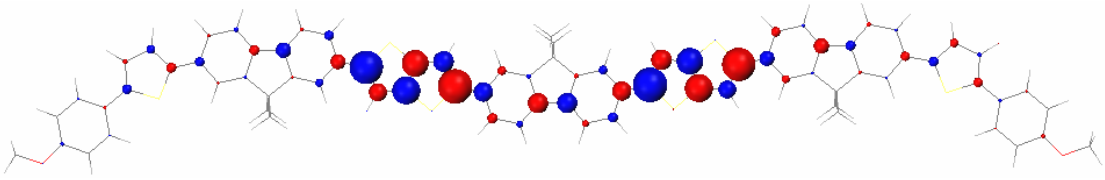

Figure 4.27: Transition dipole densities for the straightened PV353 molecule in its GS.

The highest densities are located on the thiophene units similarly to the twisted molecules. Hence the outer parts of the molecule do not play an important role in the transfer of charges. Having investigated five molecules as monomers it is now of interest to simulate them in a dimer configuration. Therefore the compound PV316 and PV353 were chosen and modelled.

4.4.2 Dimer Characterisation

When going from a monomer to a dimer configuration the energetic levels change due to the interaction of the molecular orbitals when brought closely together like shown in Figure 2.24 in section 2.4.5. This influences the emission and absorption wavelengths and transition intensities between HOMO and LUMO levels. The OS of the transitions can be used to compare between monomer and dimer configurations. A large OS indicates a strong transition, but one still has to consider which excited state (E.S.) is involved. Anti-cofacial or cofacial configurations are rarely encountered in crystalline structures, which is why the impact of the translation of one molecule along its long axis is investigated to assess the influence of packing geometry on charge transport.[5]
In Table 4.11 the simulated characteristic values of the PV316 dimer for all shifts along the long axis are summarised.

Table 4.11: PV316 dimer ground state characteristics.

Excited State E.S.#	Shift (Å)	HOMO (eV)	LUMO (eV)	Peak Absorption Energy (eV)	Peak Absorption Wavelength (nm)	Oscillator Strength
1	0	-6.307	-0.978	2.454	506	0
1	5	-6.303	-0.985	2.457	505	0.0002
1	10	-6.293	-0.977	2.474	501	0.0001
1	12	-6.285	-0.987	2.469	502	0.0001
1	18	-6.288	-0.966	2.476	501	0.0005
1	20	-6.293	-0.969	2.487	499	0.0004
1	25	-6.309	-0.973	2.499	494	8.6864
1	30	-6.305	-0.972	2.491	498	8.5940
1	35	-6.305	-0.970	2.491	498	8.8661
1	40	-6.300	-0.965	2.491	498	9.1065
1	45	-6.308	-0.969	2.495	497	9.2027
1	50	-6.311	-0.972	2.499	496	9.2675
1	55	-6.313	-0.973	2.502	496	9.2624
1	60	-6.314	-0.974	2.503	495	9.1693
2	0	-6.307	-0.978	2.557	485	9.4906
2	5	-6.303	-0.985	2.530	490	8.8073
2	10	-6.293	-0.977	2.524	491	8.2122
2	12	-6.285	-0.987	2.521	492	8.0004
2	18	-6.288	-0.966	2.515	493	8.4182
2	20	-6.293	-0.969	2.510	494	8.6239

For shifts from 0 – 20 Å the energies for E.S.#1 and #2 are given since the former is a dark state in this configuration with an OS = 0. Note that the HOMO and LUMO energies for E.S.#1 and #2 are the same, the transition energies however are not. This is because the absorption energies are composed from different HOMO to LUMO transitions. E.S.#1 might mainly be dominated by a HOMO to LUMO and E.S.#2 by a HOMO to LUMO+1 transition. See section 3.4.2 for a more detailed description on how the E.S.s transitions are composed. For shifts between 0 to 20 Å the E.S.#1 shows OSs close to zero and the E.S.#2 is the state mainly involved in the absorption transition. Most charges will be transferred to the lower E.S.#1 and since the difference in energy (E.S.#2 – E.S.#1) is larger than 25 meV it is very unlikely that some might are transferred back to E.S.#2. Emission however is most likely to take place from the lowest E.S. to the GS (Kasha's rule).[52] If the coupling between these two states is low light emission is strongly attenuated.[83] This means that a displacement of 25 Å and

higher between the two molecules is favourable for highly emissive transitions since then the E.S.#1 is then optically allowed. For the straightened PV316 monomer the OS = 4.4753. In the dimer for shifts from 25 to 60 Å the OS is about twice as large, hence for this configuration transitions from HOMO to LUMO levels are twice as likely to take place. In a dimer there are more charges to interact with each other than in a monomer this result in not unreasonable. For 0 to 20 Å shifts however the OS = 0, which means that the monomer would be the preferable configuration opposed to the dimer. One therefore cannot generalise that a dimer is more efficient than a monomer or vice versa.

The OSs of the four lowest E.S. against the longitudinal shift are plotted in the left graph in Figure 4.29.

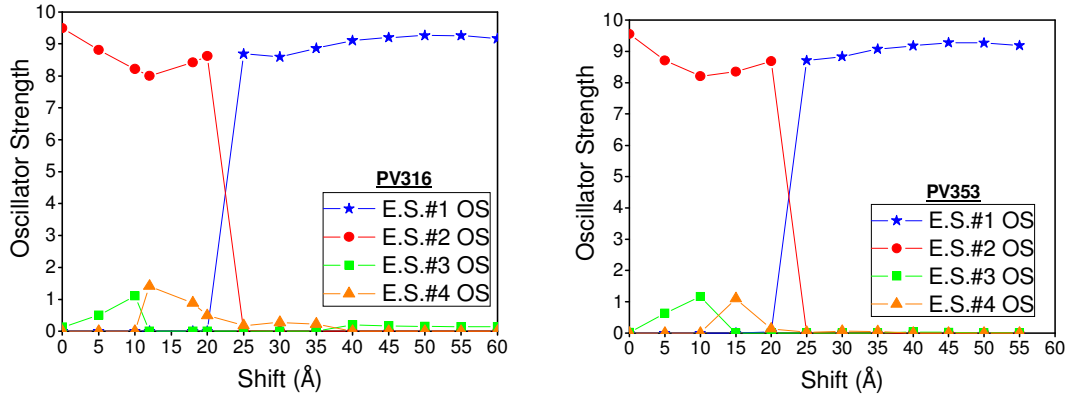

Figure 4.28: Variation of the oscillator strengths of the four lowest excites states (E.S.#1 being the lowest) with a longitudinal shift of the two molecules in the PV316 (left) and PV353 (right) dimer.

The switch of OS from E.S.#2 to E.S.#1 between 20 to 25 Å is also observed for the PV353 dimer in the right graph. So for both dimers larger shifts are favourable for efficient light emission as the interaction between the lowest excited state and the GS is not forbidden. For molecules with rod-like chromophores two different arrangements, called H- and J-aggregate, are often observed. In a stack (H-aggregate), which would correspond to our 0 – 20 Å shifts, chromophores tend to show a bathochromic shift. When aligned beside each other (J-aggregate), which corresponds to our 25 – 60 Å shifts, they display a hypsochromic shift.[88] This effect is also observed with the PV316 dimer as the absorption wavelength in the H-type is smaller than in the J-type. Similar results were obtained with the PV353 dimer. The simulated characteristics for the GS of PV353 are summarised in Table 4.12.

Table 4.12: PV353 dimer ground state characteristics.

Excited State E.S. number	Shift	HOMO (eV)	LUMO (eV)	Peak Absorption Energy (eV)	Peak Absorption Wavelength (nm)	Oscillator Strength
1	0	-6.314	-0.907	2.520	492	0.0002
1	5	-6.324	-0.899	2.532	489	0.0022
1	10	-6.304	-0.901	2.539	488	0.0003
1	15	-6.325	-0.907	2.542	487	0.0003
1	20	-6.337	-0.907	2.570	482	0.0337
1	25	-6.340	-0.908	2.568	483	8.7080
1	30	-6.340	-0.908	2.561	484	8.8378
1	35	-6.343	-0.908	2.559	485	9.0740
1	40	-6.342	-0.907	2.562	484	9.1792
1	45	-6.340	-0.905	2.566	483	9.2757
1	50	-6.339	-0.903	2.571	482	9.2697
1	55	-6.336	-0.900	2.572	482	9.1895
2	0	-6.314	-0.907	2.632	471	9.5529
2	5	-6.324	-0.899	2.608	476	8.7124
2	10	-6.304	-0.901	2.596	478	8.2060
2	15	-6.325	-0.907	2.589	479	8.3518
2	20	-6.337	-0.907	2.576	481	8.6841

One can conclude that both PV316 and PV353 display stronger absorption transitions in an anti-cofacial dimer than in a monomer, this will also lead to a strong emission in a J-aggregate.

The transition dipole densities for the excited state with the largest OS are plotted for the 0 Å shift of the PV316 and the PV353 dimer in Figure 4.29 and Figure 4.30 respectively.

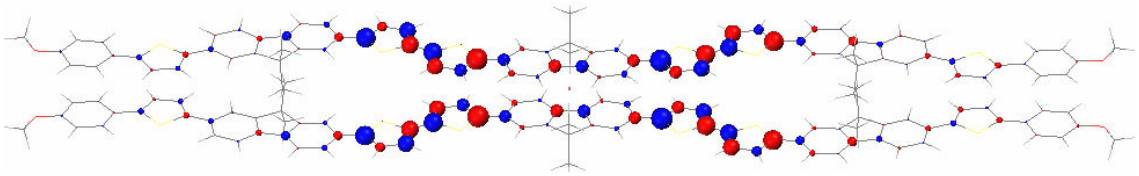

Figure 4.29: Transition dipole densities of E.S.#2 on the PV316 dimer with 0 Å shift.

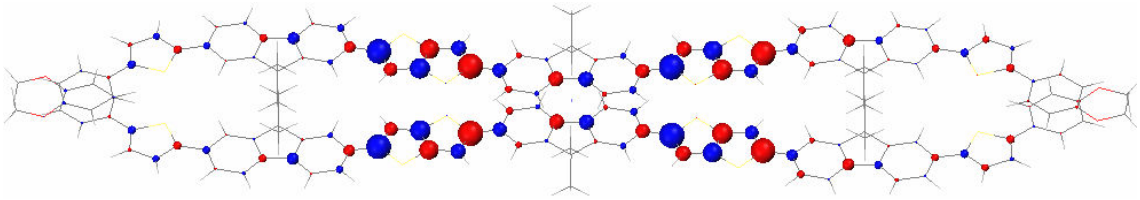

Figure 4.30: Transition dipole densities of E.S.#2 on the PV353 dimer with 0 Å shift.

The transition dipole densities are located on the inner thiophene units as found on the PV316 and PV353 monomer. This is observed for all E.S.s that were simulated. For larger shifts, where only the outer parts overlap, where thiophenes are absent, one hence can expect that the coupling is low as the thiophenes are then too far away from each other to interact.

4.5 Coupling in Dimers

Different interaction mechanisms, the excitonic and supermolecular coupling as well as the charge transfer integral, were calculated for longitudinal offsets in a PV316 and PV353 dimer

4.5.1 Excitonic Coupling

The excitonic coupling contribution to the intermolecular interaction in the dimer was calculated. As discussed in 2.4.6 excitonic coupling involves only transitions from HOMO to LUMO on one molecule and a dipole-dipole interaction between the two molecules. The results for the excitonic coupling change with shift along the long axis are presented in Figure 4.31 for the PV316 dimer and the PV353 dimer. The excitonic coupling is obtained from the interaction of the transition dipoles; hence the sign of the coupling value can change due to the orientation of the dipoles. For the evaluation only the magnitude of the coupling value and not its sign is important.

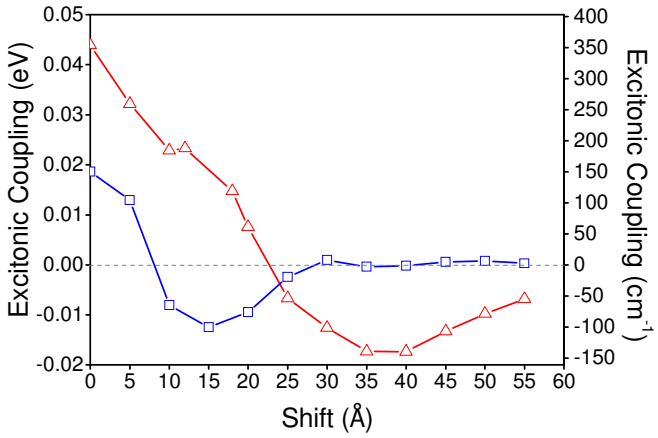

Figure 4.31: Excitonic coupling between two molecules in an anti-cofacial dimer configuration with longitudinal shift. Graph shows the PV316 dimer (triangles) and the PV353 dimer (squares).

The excitonic coupling in the PV353 dimer is strongest at 0 Å and equal to zero at a 8 Å shift. Then the coupling increases again and fluctuates around zero for all larger offset positions above 30 Å. This is plausible as the charges, when looking at the transition dipole densities (Figure 4.30), are mainly concentrated in the centre of each molecule. After a shift of 30 Å only the end chains still overlap, so there is nothing to interact with each other. PV316 however does not show the same behaviour although its charges are also situated in the middle of the molecule. This behaviour is not explainable and needs further investigation. The excitonic coupling for the 0 Å shift is twice as large in the PV316 dimer as for the PV353 dimer. The only difference between the centres of the molecules is that PV316 has bithiophenes instead of the fused thiophenes of PV353. As on the thiophene units most of the charge transfer takes place one can conclude that bithiophenes are more efficient opposed to fused thiophenes. This assumption however only can be made for the anti-cofacial dimer. In more realistic arrangements, with twisted molecules and e.g. horizontal displacement the coupling might be very different. Considering that kT ≈ 25 meV the excitonic coupling values are very low with a maximum of 18.6 meV and 43.9 meV at 0 Å for PV353 and PV316 respectively.

4.5.2 Supermolecular Coupling

To obtain a value for the supermolecular coupling the transition energies of the two lowest optically allowed excited states (E.S.) are subtracted from each other and then divided by two.[43] As already shown in section 4.4.2 the lowest excited state E.S.#1 is optically forbidden in a H-aggregate arrangement for both the PV316 and PV353 dimer.

For the coupling calculation the corresponding "partner" state for either E.S.#1 or 2 had to be determined, since it is not automatically the next lowest E.S. In Figure 4.32 the supermolecular coupling results for both molecules are shown.

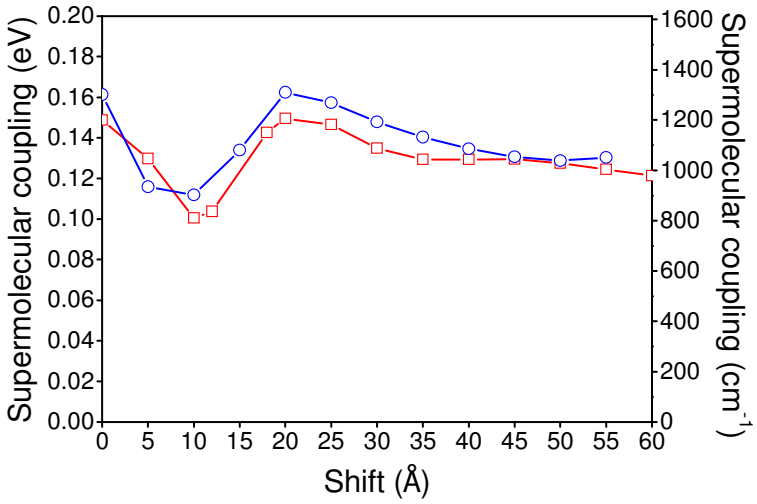

Figure 4.32: Supermolecular coupling for PV316 (squares) and PV353 (circles) dimers shifted along their long axis.

The coupling values are about four times larger than those from the excitonic coupling. This is normal as charges are more "free" to move in the supermolecular approach and hence can interact more easily with the environment. The maximum coupling value of 0.16 eV is found for PV353 at a shift of 20 Å. For comparison a co-facial dimer consisting of two polyene chains with 6 carbon atoms and separated by 6 Å had a simulated supermolecular coupling value of about 0.22 eV.[83]

In both dimers the coupling is lowest for a shift of 10 Å. An explanation for this drop can be found from the plots of the transition dipole densities for the two E.S.s used to calculated the splitting these were the states E.S.#2 and E.S.#4 for the 0 Å shift in the PV316 dimer. Their transition dipole densities are shown in Figure 4.33 and Figure 4.34 respectively.

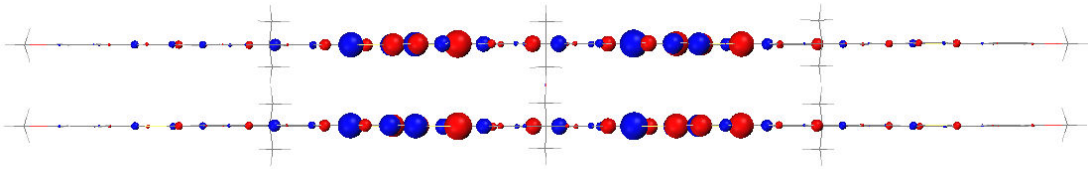

Figure 4.33: Transition dipole densities of E.S.#2 for the 316 SM dimer with a lateral shift of 0Å.

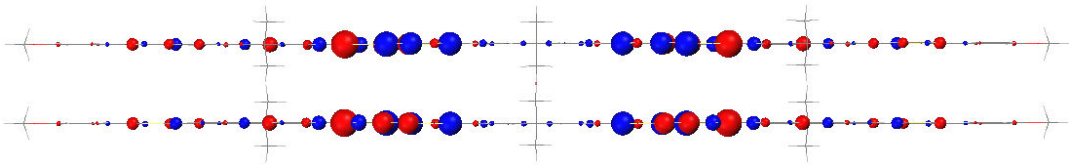

Figure 4.34: Transition dipole densities of E.S.#4 for the 316 SM dimer with a lateral shift of 0Å.

For the 0 Å anti-cofacial PV316 dimer the highest transition densities are directly opposite to each other and the short range through bond interaction is strong. Looking at the densities for the 12 Å shift in Figure 4.35 and Figure 4.36 one can see that the densities are not symmetrically distributed like for the 0 Å shift. For both excited states the highest densities are opposite to regions with very small transition dipole densities, so the coupling is low.

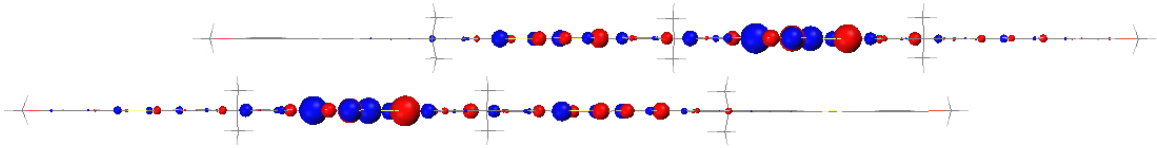

Figure 4.35: Transition dipole densities of E.S.#2 for the 316 SM dimer with a longitudinal shift of 12 Å.

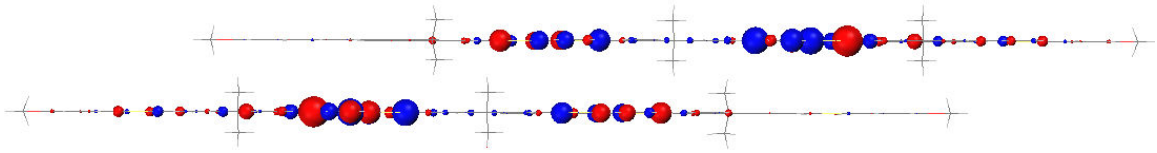

Figure 4.36: Transition dipole densities of E.S.#3 for the 316 SM dimer with a longitudinal shift of 12 Å

A redistribution of the densities is also the reason for the increase in coupling for the 20 Å shift. The transition densities of the two excited states involved are shown in Figure 4.37 and Figure 4.38. In E.S.#4 the two highest densities face each other so that the coupling can be more efficient than for the 12 Å dimer arrangements.

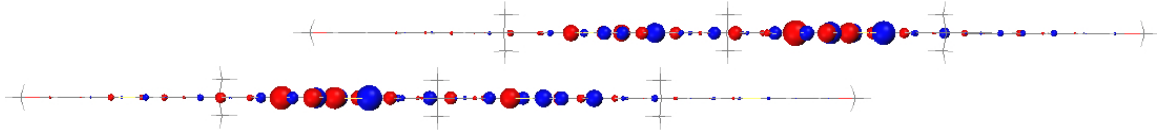

Figure 4.37: Transition dipole densities of E.S.#2 for the 316 SM dimer with a longitudinal shift of 20 Å

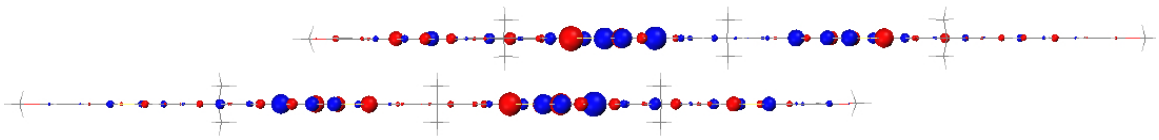

Figure 4.38: Transition dipole densities of E.S.#4 for the 316 SM dimer with a longitudinal shift of 20 Å

It has to be considered however that not only the presence and strength of the transition dipole densities influence the coupling, but also the sign of the transitions. The supermolecular coupling of the PV353 dimer shows a similar behaviour but with slightly stronger coupling values.

4.5.3 Charge Transfer Integral

The charge transfer integral for the PV316 dimer was calculated with shifts from 0 to 60 Å. Here one molecule represents the donor and the other the acceptor though both molecules are of the same structure. As shown in Figure 2.26 charge transfer involves the excitation of the host followed by either hole transfer between HOMO levels or electron transfer between LUMO levels of the donor and the acceptor. With the charge transfer integral one can determine the electronic coupling between two states.[44]

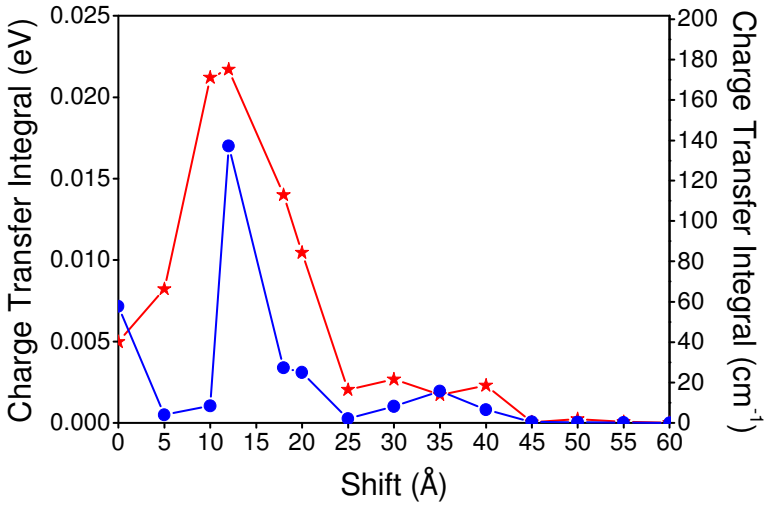

Figure 4.39: Charge transfer integral in the PV316 dimer for HOMO (stars) and LUMO (circles) level.

The coupling rate from HOMO to HOMO is slightly higher than from LUMO to LUMO with a maximum at 12 Å of 0.022 eV for the HOMO and 0.017 eV for the

LUMO level. This is expected as for small molecules or oligomers the splitting of the HOMO level is higher as for the LUMO level and the transfer therefore larger.[40]

For comparison for a tetracene co-facial dimer with 4.5 Å spacing a transfer integral value of about 0.04 eV for holes and 0.03 eV for electrons was simulated.[89] It is also noted that the charge transfer is high when supermolecular coupling is low and becomes zero with a shift of 40 Å. This makes sense when we consider that with increasing offset the overlap of the orbitals involved decreases. It has been shown that even with small molecular displacements significant changes in the transfer integrals have been observed.[89]

It is difficult to compare coupling values from different simulations and research groups as the same dimer configuration is seldom used. The length of the molecules investigated and the distance between them changes the coupling values significantly. It is however encouraging that our simulated coupling values are not far off from the published results.

4.6 Summary Chapter 4

We have simulated the transition energies and oscillator strengths for a number of nematic molecules. We find that the OS increases with molecular size. In the ground state the molecules have a twisted configuration with torsion angles of about 25°. A planar configuration is obtained in the excited state. A parallel anti-cofacial dimer configuration was used to simulate the optical transition in a thin film. The ground state OS was modelled as a function of long offset of the molecules to investigate the effect of nematic ordering. The OS was effectively independent of the offset. However for displacement ≤ 20 Å the lowest energy transition is forbidden, whereas it is allowed for larger offsets. Assuming a similar result for emissive transitions we can conclude that efficient solid state PL requires a long offset. The nematic material has random offsets so some but not all molecules will show efficient radiative decay. This might be one of the reasons why the optical quantum efficiency in the solid state is significantly less than in solution for all of our materials, see Table 4.2. Another cause can be quenching due to exciton diffusion to non-radiative defects within the film. These defects can be induced during film preparation and are not present in solution due to the free movement of the molecules.[1]

5 White OLEDs

White organic light emitting diodes (WOLEDs) are extensively researched for their application as backlights for liquid crystal displays (LCDs) and as solid-state lighting sources for room illumination.[90; 91, 92] An advantage to common light sources like incandescent light bulbs or fluorescent lamps is their low power consumption, which is an important factor since the general public is becoming more energy-conscious.[93] Many different configurations have been investigated to achieve white emission from organic materials using either small molecules or polymers. Small molecules are vacuum deposited and devices with a pure single component,[94] a host doped with red, green and blue chromophores,[95, 96] a multilayered device[97, 98] or stacked OLEDs were reported.[99] Polymers offer the much cheaper solution based deposition procedures like ink-jet printing and spin coating.[100] White light has been obtained with different polymer based compounds like polyaniline,[101] polymer blends,[102, 103] doped polymers,[104] co-polymers,[105] and side-chain polymers.[106] For LCDs backlights linear polarised white emission would be even more of advantage as then the loss due to the polariser incorporated is omitted (see section 2.2.4). Polarised white light has been achieved from mixtures of liquid crystalline oligomers in the glassy phase.[107] Oligomers as well as polymers however have also the disadvantage of high glass transition temperatures and the possible mixing of layers in a multilayered structure.[100] Our approach to create (polarised) white light is to blend two emissive LCs of different colour with each other. The properties of the LC allow uniaxial molecular alignment, which leads to polarised emission. Crosslinking of the LC layer forms a molecular network and renders the film insoluble.

In this chapter the necessary preliminary tests and the production of polarised white light emitting diodes with in-house made materials are described. Several blue/green LC emitters were mixed with an orange/red LC emitter to create white emission. Polymer blends tend to phase separate.[108] This would result in a non uniform emission of red and blue patches. Therefore first the miscibility of blends made from different ratios of the blue/green compound and red compound was tested. For our application a nematic

phase at room temperature was required as plane polarised emission can be obtained from an aligned LC phase. Therefore the phase for all blends from various compounds that gave white light was checked at room temperature using a microscope.
The diodes made from these mixtures were then tested (procedure see section 3.3) in terms of brightness, efficiency, spectra, CIE colour coordinates and their stability and whether they gave polarised emission when aligned.

5.1 Liquid Crystal Blends

Miscibility tests with the blue/green compounds AW01 and SPK107 and the red compound SPK146 were carried out. Their chemical structures are given in section 4.1. Blends of different ratios were prepared according to the procedure described in section 3.2.6. The clearing points from the neat compounds were found using the Differential Scanning Calorimetry (DSC) as described in section 3.1.1. SPK107 clears at 30°C and its glass transition temperature is T_g = 22°C. A crystallisation temperature was not measurable with the available equipment. The transition temperatures for AW01 are Cr-N = 77°C, N-I = 111°C and T_g = 5°C and for SPK146 Cr-N = 180°C, N-I = 246°C and T_g = 76°C. A polarisation microscope (section 3.1.4) was used to determine whether the blends showed a nematic phase at room temperature.

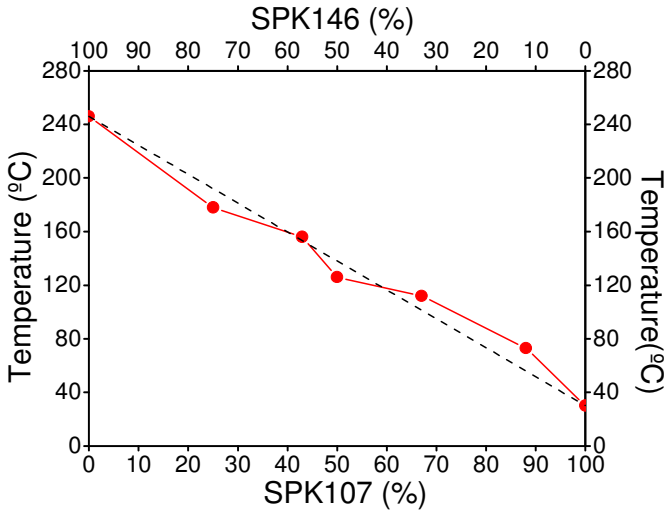

Figure 5.1: Phase diagram of the clearing temperatures for blends of the blue/green compound SPK107 and the red compound SPK146. Complete miscibility of the nematic phases of both components is observed for all compositions in the phase diagram using mixtures based on mol %. The dashed line indicates the ideal behaviour.

Figure 5.1 shows the clearing temperatures obtained from the blends of SPK107 and SPK146. By connecting the two clearing points of the neat compounds SPK107 = 30°C and SPK156 = 246°C through a dashed line the theoretical expected temperatures are indicated. The measured temperatures are all close to the ideal. This indicates that no phase separation occurred as one then would expect the compound with the higher clearing point (SPK146) to dominate the temperature curve. However this did not happen here, which proved a good miscibility of those two compounds. The phase diagram for the different blends of the blue/green emissive compound AW01 and the red emitter SPK146 is shown in Figure 5.2.

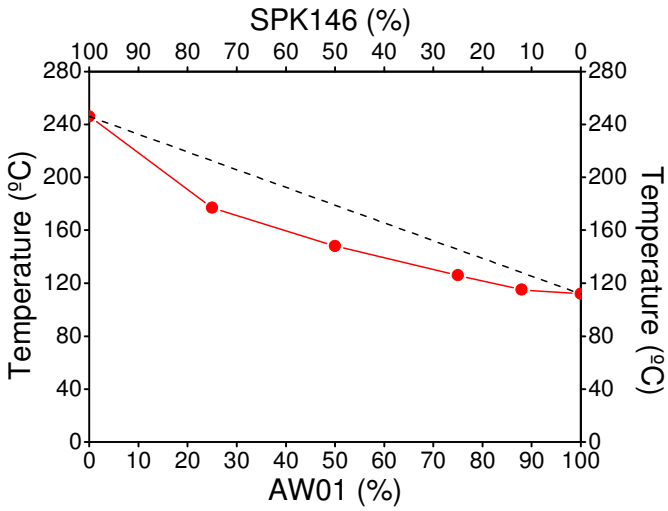

Figure 5.2: Phase diagram of the clearing temperatures for blends of the blue/green compound AW01 and the red compound SPK146. Complete miscibility of the nematic phases of both components is observed for all compositions in the phase diagram using mixtures based on mol %. The dashed line indicates the ideal behaviour.

The observed clearing temperatures for the binary mixtures are in good agreement with the theoretical predicted curve. The blue/green emissive compound GJR130 (see Table 4.1 for structure and transition temperatures) was also blended with the red SPK146 to obtain white emission. The lack of material however did not allow the investigation of several blend ratios. The ratio of 7:1 which corresponds to 88 % of blue/green compound and 12 % of red compound was found to work best to obtain white electroluminescence (EL). Photos of the nematic Schlieren textures at RT from blends of 88% AW01, GJR130 or SPK107 with 12 % SPK146 are shown in Figure 5.3.

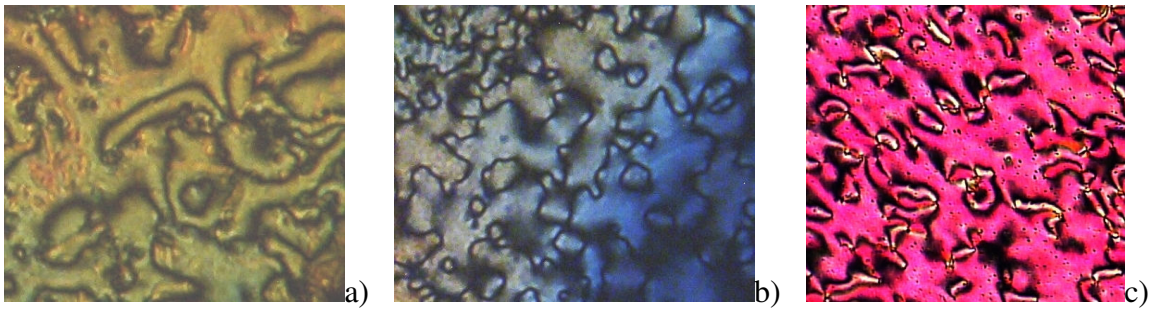

Figure 5.3: Photos from the nematic phases at room temperature from the blends of a) GJR130 and SPK146 R:7:1, b) SPK107 and SPK146 R:7:1, c) AW01 and SPK146 R:7:1 taken through a polarising microscope.

As previously discussed in section 2.2.3 a nematic phase's characteristics are the 2- and 4- point brushes. These are found for all three different blends a), b) and c) at RT, which

proved complete miscibility of the blended compounds. Furthermore no phase separation despite the differences in clearing and melting point could be observed for all blend ratios of AW01 and SPK146 and SPK107 and SPK146. This and the formation of a nematic phase frozen in a glassy state at RT verify that the blends were homogeneously mixed.

5.2 Spectral Overlap of Compounds

The red emitter SPK146 itself showed a poor performance when tested in an OLED. The blue/green emitters apart from SPK107 performed much better. For a white spectrum the contributions of blue/green and red have to be relatively even. It is therefore essential that Förster energy transfer from the blue/green to the red molecule takes place to enhance the performance of the red emitter. Therefore the absorption spectrum of the red emissive compound should overlap with the PL emission spectrum of the blue/green emitter. See section 2.5.3 for more information on Förster transfer. A large overlap of absorption and emission most probably gives an efficient energy transfer. The absorption spectrum of SPK146 and the PL spectra of the blue/green emitters AW01, GJR130 and SPK107 are plotted in Figure 5.4.

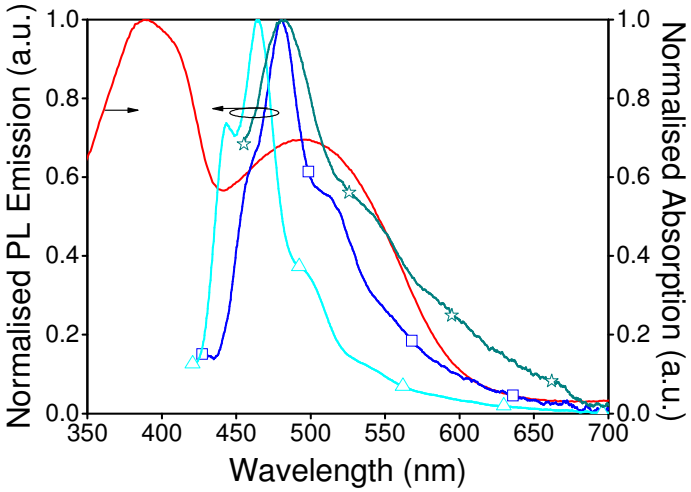

Figure 5.4: Plot of the absorption spectrum of a SPK146 film and the PL emission spectra from films made of the blue/green emitters AW01 (turquoise triangles), GJR130 (blue squares) and SPK107 (green stars). An overlap for all blue/green PL spectra with the absorption of the red SPK146 is observed.

The PL spectra of all blue/green emitters overlap with the absorption spectrum of SPK146, so that efficient transfer can be expected.

5.3 White OLED Devices

The measured results for Organic Light Emitting Diodes (OLEDs) made from neat and blended films are now presented. The EL spectra were corrected for the nonuniform response of the spectrometer and smoothed afterwards (20 pts adjacent averaging). The spectral correction has a greater influence in the blue/green than in the red region. Maxima could be red shifted for about 30 nm due to this correction. The spectrometer used showed a pixel error at 450 and 650 nm. Dips in the spectra at these wavelengths, that were not smoothed out are therefore artificial. The different blue/green emitters were blended with a red emitter to create white EL. More background information on the compounds used e.g. their chemical structure and optical quantum efficiency can be found in Chapter 4. OLEDs were built from the blends as described in section 3.2. A sketch of the test rig is shown in Figure 3.15.

5.3.1 OLED with AW01 and SPK146

At the first run the OLED made from AW01 only (results in Figure 5.5) reached a brightness of nearly 800 cd cm^{-2} and an efficiency over 0.3 cd A^{-1}. The spectrum had its maximum in the blue/green region around 450 nm, which changed at higher voltages. Note that actually a double peak at 440 and 463 nm was seen, which was probably due to the pixel error of the spectrometer. The data shown below is from the second run of the tested electrode. The spectrum of this compound tended to broaden and red shifted with time and the maximum moved from 468 to 515 nm.

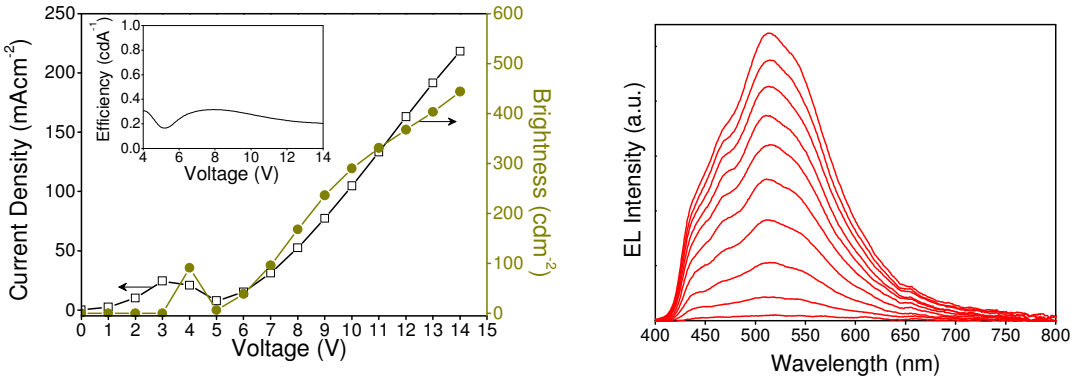

Figure 5.5: Recorded current density, brightness and efficiency as function of voltage as well as the voltage dependent EL spectrum for an OLED made with the blue/green emitting compound AW01. The OLED's test electrode had been running before at a voltage above 10 V so that the spectrum could stabilise.

Graphs in Figure 5.6 show the characteristics of an OLED made from the red emitter SPK146.

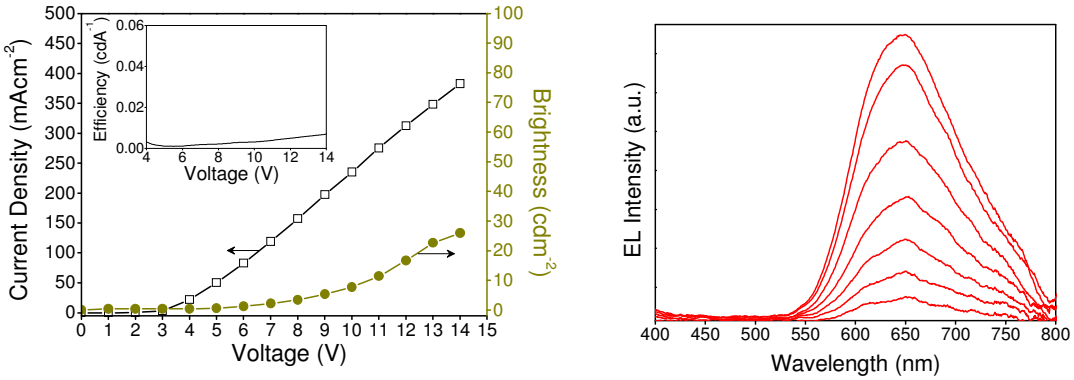

Figure 5.6: Recorded current density, brightness and efficiency as function of voltage as well as the voltage dependent EL spectrum for an OLED made with the red emitting compound SPK146.

The device showed an efficiency of lower than 0.01 cd A^{-1} and a brightness of less than 30 cd m^{-2}. The peak of the spectrum is at 650 nm. The two compounds characterised above were then blended with a ratio of (7:1) 88 % AW01 and 12 % SPK146 and an OLED fabricated. The device characteristics are shown in Figure 5.7.

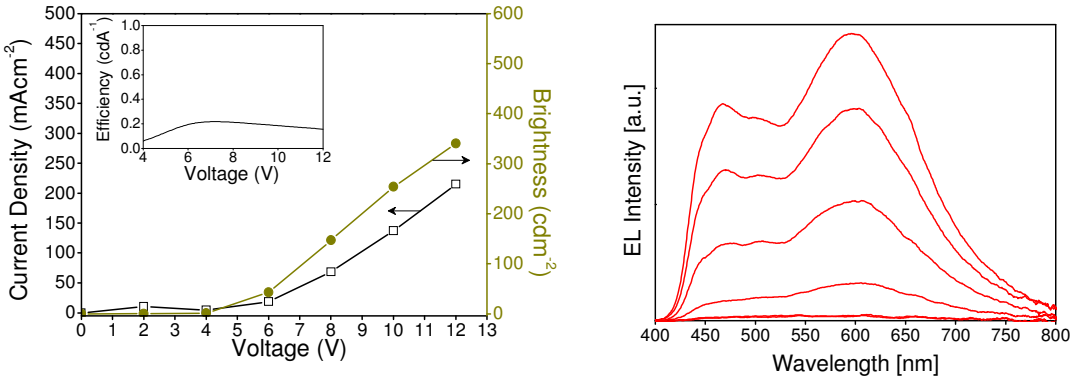

Figure 5.7: Recorded current density, brightness and efficiency as function of voltage as well as the voltage dependent EL spectrum for an OLED made out of a blend of 88 % of the blue/green emitter AW01 and 12 % of the red emitter SPK146.

At voltages below 9 V the device showed a weak red emission. After running the device above 11 V for several seconds the colour of the emission changed to white. This effect was not reversible and white emission was maintained for different voltages. The white OLED had a peak efficiency of about 0.2 cd A^{-1} and brightness of 350 cd m^{-2}. The two emission peaks were at 463 and 600 nm. Figure 5.8 shows the CIE coordinates for different voltages obtained from an OLED made from the same blend ratio as well as a photo from the running device.

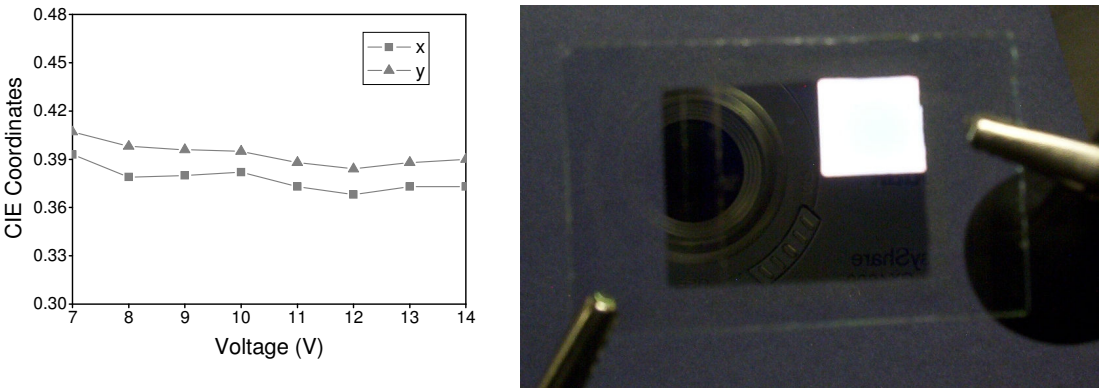

Figure 5.8: Left; measured CIE coordinates from an OLED made out of 88% AW01 and 12% SPK146 for different drive voltages. Right; photo of an OLED with on electrode running at 12 V, showing white EL emission from a blend of 88 % AW01 and 12 % SPK146.

The CIE coordinates for an ideal white light source are x = 0.33 and y = 0.33 but an artificial light source like a fluorescent lamp (warm white) shows coordinates of x = 0.44 and y = 0.40.[92] The measured coordinates for the device were x = 0.38 ± 0.01 and y = 0.39 ± 0.01 at 12 V. The white emission varied very little between 7 and 14 V. This

colour stability is an important aspect for white light sources. It is especially important for laptop displays, which work with colour filters and where the brightness can be adjusted to save power. A change in the hue of background light would result in an overall colour shift in the display.

Several white devices with the two compounds were made using also the blend ratio 7:1. A maximum brightness of about 850 cd m^{-2} with an efficiency of 0.40 cd A^{-1} and satisfying CIE coordinates with values between 0.32 and 0.40 were obtained, see results in Table 5.1.

Table 5.1: Results from different OLEDs made from 88 % AW01 and 12 % SPK146 (7:1).

Device number	Peak Brightness (cd m^2)	Peak Efficiency (cd A^{-1})	CIE Coordinates at 10-12 V		Crosslinked
			x	y	
Al63.2	280	0.21	0.35	0.38	no
Al64.1	850	0.40	0.40	0.40	yes
Al65.1	470	0.42	0.36	0.40	no
Al66.1	560	0.21	0.32	0.39	yes

The emission for the brightest device achieved (Al64 1) was closer to the yellow region. This red shift was caused through weighing errors as the scale used had a resolution of 0.1 mg and very small quantities of 0.5 mg (red) - 4 mg (blue/green) were weighed. White emission was also obtained from crosslinked films with the devices AL64.1 and Al66.1. Crosslinking renders the films insoluble so that multilayered structures can be built without any problems. In Figure 5.9 the EL spectra of the OLEDs characterised before are shown in the left graph. The two peaks of the spectrum of the blend don't coincide with the peaks of the neat compounds. Both peaks experienced a blue/green shift of about 50 nm. This rearrangement of the energy levels might be due to the interaction of the different molecule and orbitals as discussed in section 2.4.5.

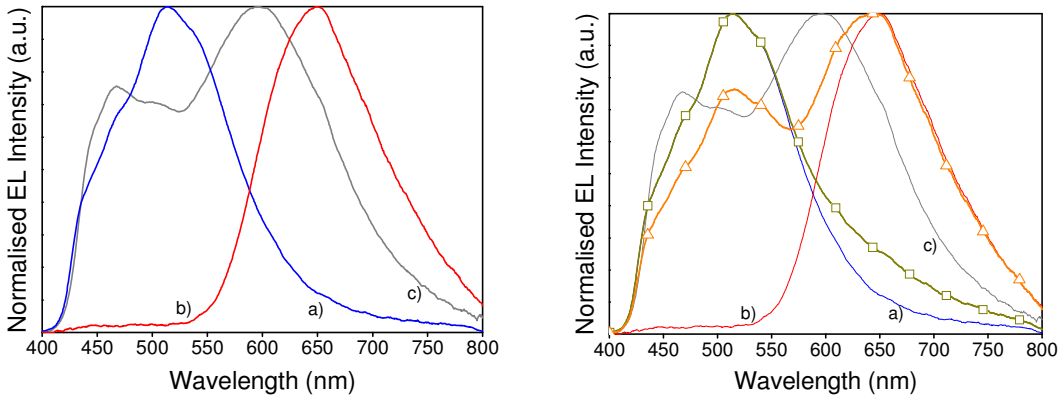

Figure 5.9: The left graph shows the normalised EL spectra from OLEDs made from a) AW01 and b) SPK146 and c) their blend with a ratio of 88 % AW01 and 12 % SPK146. The right graph shows the same spectra again with two additional plots. Squares presenting the resultant normalised graph if 88 % of the normalised AW01 graph and 12 % of the normalised SPK146 graph are added together mathematically. Triangles show the result when 45 % AW01 and 55 % SPK146 are added together.

The right graph superimposes EL curves of pure AW01 and SPK146 added together in different ratios (graphs with symbols). The squares show the result for the actual mixture, which was 88 % AW01 with 12 % SPK146. This spectrum is not very different to the one obtained using the pure AW01 device. The triangles show the combined EL spectrum from 45 % AW01 and 55 % SPK146. This ratio was chosen to reproduce the relative heights of the two peaks in the actual emission spectrum. Both of these simulations suggest that some energy is transferred from AW01 to SPK146. The recorded PL and EL spectra from the OLED AL64 are shown in Figure 5.10. The EL spectrum was recorded when the device was switched on the first time at a low voltage (9 V) and after running for a few seconds at 12 V. The PL spectra were recorded before and after the device was switched on.

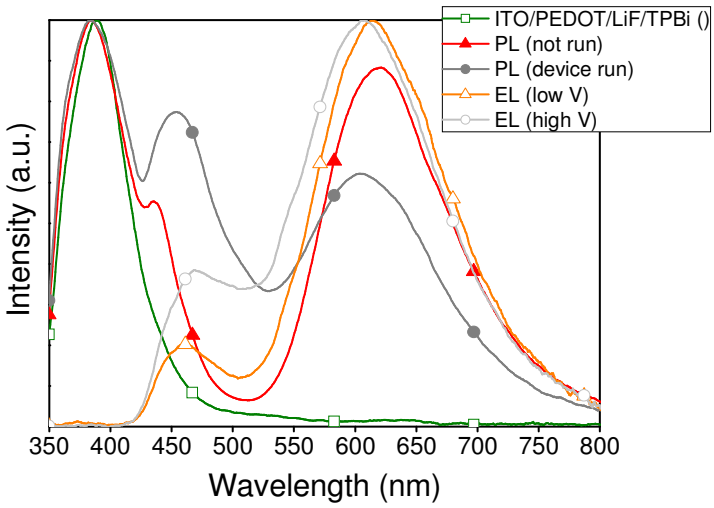

Figure 5.10: PL and EL spectra from the OLED Al64. For the PL the film was excited with a HeCd laser at 325 nm. As a reference the PL spectrum of an ITO/PEDOT/TPBi/LiF layer is included to show that the peak at 388 nm is due to those materials.

The peak in the PL curves at 388 nm originates from other layers in the device. The PL spectrum recorded before switching and the low voltage EL spectrum are similar; emission is mostly from the red SPK146 following energy transfer. However the red OLED emission is shifted to 614 nm opposed to the 619 nm PL peak. (We cannot comment on the shift in the peak emission wavelength near 450 nm because of the overlap with emission from other layers.) After operation at 12 V the blue/green emission increases in both EL and PL with the same red peak wavelength of 605 nm.

5.3.2 Results for GJR130 and SPK107 with SPK146

In Figure 5.11 characteristics of an OLED made of 88 % GJR130 and 12 % SPK146 taken two weeks after the OLED was fabricated are presented. Figure 5.12 shows a device from 88 % SPK107 and 12 % SPK146.

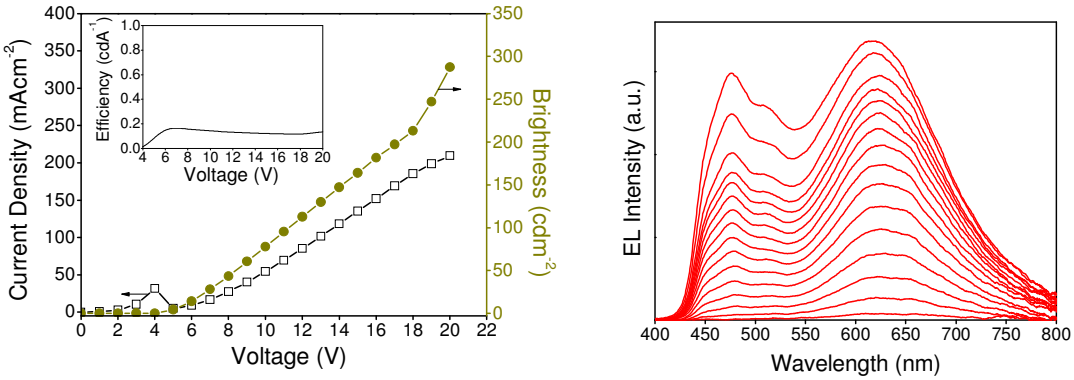

Figure 5.11: Recorded current density, brightness and efficiency as function of voltage as well as the voltage dependent EL spectrum for an OLED made out of a blend of 88 % of the blue/green emitter GJR130 and 12 % of the red emitter SPK146.

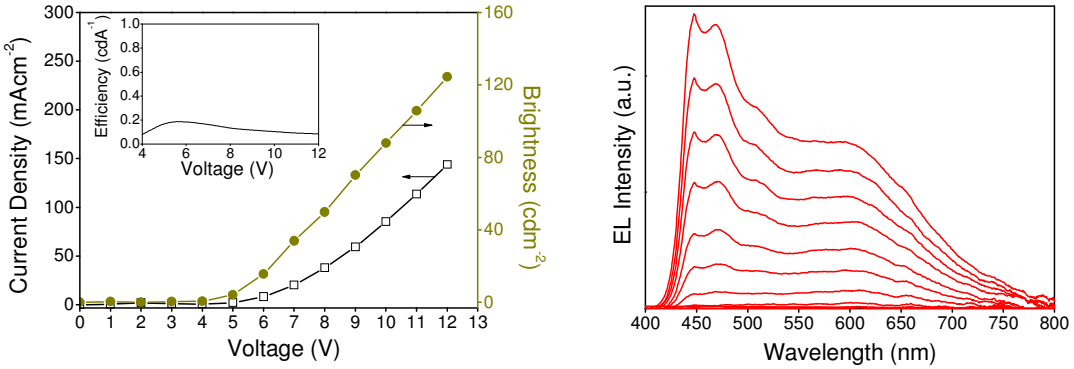

Figure 5.12: Recorded current density, brightness and efficiency as function of voltage as well as the voltage dependent EL spectrum for an OLED made out of a blend of 88 % of the blue/green emitter SPK107 and 12 % of the red emitter SPK146.

The same effect took place for both devices as already observed with the AW01/SPK146 device (Figure 5.7). The OLEDs emitted a weak red emission at lower voltages and after running the device above 11V for several seconds the colour of the emission changed to white. This effect was also not reversible. The for all devices observed change in the spectrum at higher voltages might be due to the degradation of SPK146 and needs further investigation. The GJR130 device showed an efficiency of about 0.18 cd A^{-1} and brightness of 290 cd m^{-2} and the SPK107 device showed and efficiency of about 0.18 cd A^{-1} and brightness of 125 cd m^{-2}.

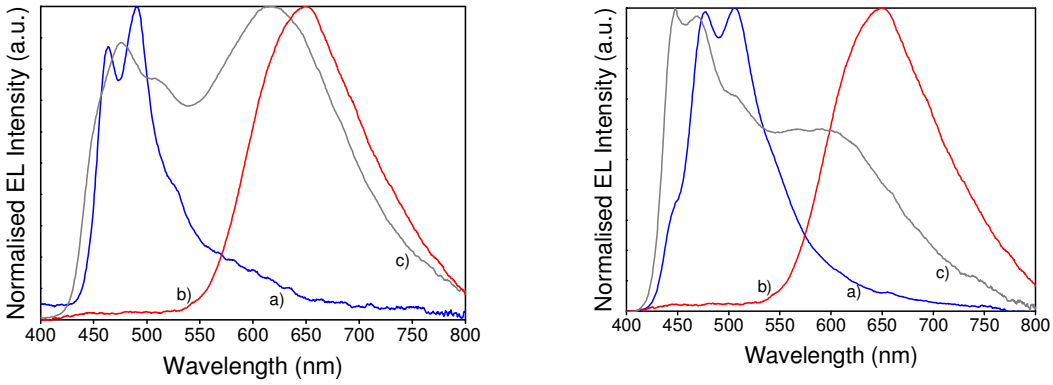

Figure 5.13: Left; normalised EL spectra from OLEDs made from a) GJR130 and b) SPK146 and c) their blend with a ratio of 88 % GJR130 and 12 % SPK146. Right; normalised EL spectra from OLEDs made from a) SPK107 and b) SPK146 and c) their blend with a ratio of 88 % SPK107 and 12 % SPK146.

In Figure 5.13 the EL spectra of the before characterised OLEDs made with GJR130/ SPK146 (left) and SPK107/SPK146 (right) and the spectra obtained from neat devices are shown. The two peaks of the spectrum of the blend don't coincide with the peaks of the neat compounds. The red peaks experienced a hypsochromic shift of about 30 nm and 50 - 60 nm for GJR130 and SPK107 respectively.

In Figure 5.14 the measured CIE coordinates for the different OLED results discussed are shown within a colour triangle. For comparison two reference points are inserted; the coordinates for an ideal white light and from a real light source in the laboratory, a fluorescent tube.

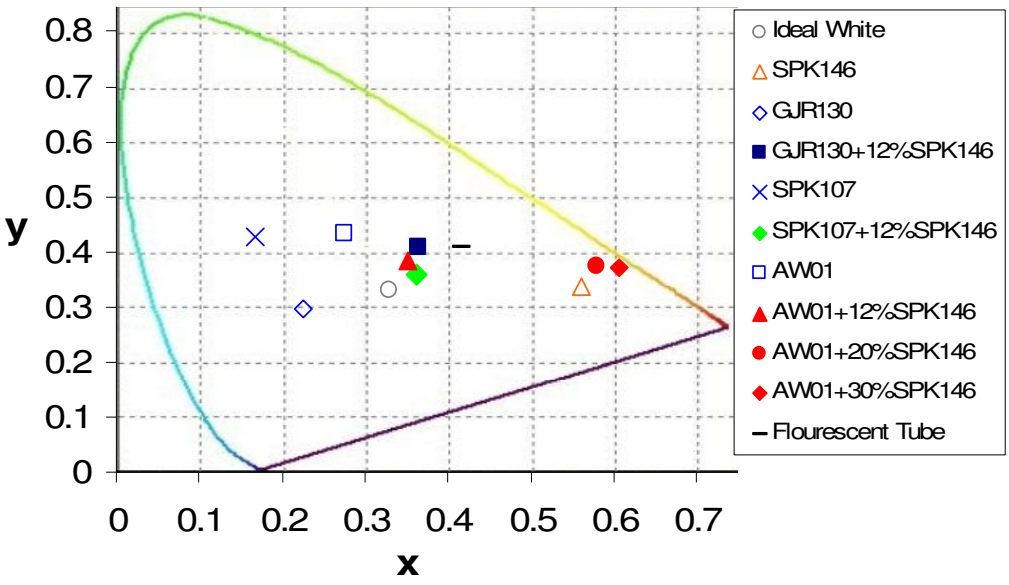

Figure 5.14: The CIE colour coordinates of the characterised OLEDs. GJR130, AW01, SPK107 and AW01 + 30 % SPK146 were recorded at a device voltage of 10 V, SPK107 + 12 % SPK146 at 7 V, SPK146 at 8 V, AW01 + 12 % SPK146 at 12 V, AW01 + 20 % SPK146 at 14 V and GJR130 + 12 % SPK146 at 17 V.

The CIE coordinates of the white devices with the 12 % SPK146 contribution lie between the ideal white and the measured fluorescent tube. This shows that the mixing of the red SPK146 with all three blue/green components delivered satisfying white emission. Furthermore the measured coordinates for two AW01 OLEDs with a 20 and 30 % SPK146 contribution are shown. Their measured coordinates are close to the result from the neat SPK146 OLED. The orange-reddish emission was even and stayed stable over several test runs and at higher voltages. The CIE coordinates of the 30 % OLED for example were x = 0.627 ± 0.006 and y = 0.358 ± 0.008 for drive voltages of 6 – 12 V. The device efficiency of the blend compared to the neat device increased by a factor of about 10 and the brightness by a factor of about 3. The measured maximum efficiency and brightness for 20 % SPK146 were 0.1 cd A^{-1} and 79 cd m^{-2} and for 30 % SPK146 0.09 cd $A^{-1}$and 89 cd m^{-2}. This shows that the blend with the more efficient blue/green compound AW01 increases the performance of the red emitter SPK146. Unfortunately the efficiency of all devices is disappointingly low compared with monochrome Hull OLEDs (≤ 12 cd A^{-1}) and more particularly with white phosphorescent OLEDs with 1000 cd m^{-2} at 3.6 V).[109] This is probably due to the unsuitable red dopant, SPK146, which may degenerate on operation.

5.3.3 Polarised White Light Emission

Having shown in sections 5.3.1 and 5.3.2 that the blend of our blue/green and a red light emitting LCs gives white emission in an OLED it is of interest whether the liquid crystalline properties can be used to produce polarised white emission. Therefore the PEDOT layer on which the LC is spin-coated, was rubbed with a cloth according to the procedure described in section 3.2.5. The deposited LC then aligns itself parallel to the rubbing direction. The EL was measured through a polariser, which was turned for 90° for a second measurement to obtain the polarisation ratio EL(ǁ)/EL(-). EL(ǁ) corresponds to the polariser being parallel to the alignment direction of the LCs and EL(-) being perpendicular to it.

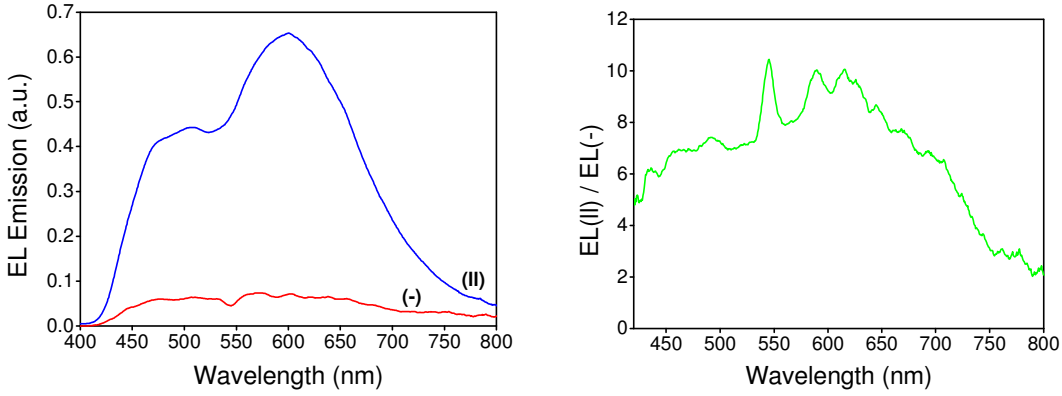

Figure 5.15: Left; emission spectrum from a WOLED at 10 V made from a crosslinked blend of 88 % AW01 +12 % SPK146 with the polariser being parallel (ll) being and perpendicular (-) to the LC alignment direction. Right; the resultant polarisation ratio EL(ll)/EL(-)

The average polarisation ratio between 450 – 700 nm is 8:1 with a maximum of 10.5:1 at 545 nm. Though the polarisation ratios are not very high they are large enough to achieve ratios of 100:1 with an additional clean up polariser. We reached a polarisation ratio of 30:1 with the same alignment procedure for neat PV316 films, so that improvement can be expected.[6]

5.4 Summary Chapter 5

To conclude, we have shown that blending our liquid crystals does not result in phase separation. A nematic structure frozen in a glassy phase at room temperature was observed for all for all investigated blends of three different blue/greens and a red

compound with mixture ratios of 7:1. OLEDs built from these blends showed white EL with CIE coordinates close to the ideal white. Crosslinking of the emissive layer rendered the film insoluble. Polarised EL was obtained from one of the blends upon LC alignment with a rubbed PEDOT layer beneath. The ability to form homogeneous blends and thus homogeneous white emission over the whole electrode makes our LCs candidates for room lighting and backlight sources for LCDs. They are solution processable, which is a much cheaper production technique than those required for conventional semiconductors. The possibility to create linear polarised white emission is an important aspect for LCDs, as the loss due to the required polarisers is lower, when the emission is already polarised. Work is required to significantly improve the efficiency of the OLEDs.

6 Surface Relief Gratings

Surface relief gratings (SRGs) can be used for different purposes in organic thin film devices, e.g. to enhance the outcoupling efficiency or to act as feedback structures for DFB lasers. The outcoupling efficiency in organic LEDs is limited due to the high refractive index of the organic materials, see section 2.6.2.[110] Several approaches have been made to improve the outcoupling efficiency. Techniques already applied in common semiconductor diodes can be used to extract trapped modes; e.g. the roughening of the glass surface, where the light is extracted, changes the critical angle.[56] Light that is normally reflected back due to total internal reflection is scattered at different angles and can leave the device. With this method an increased efficiency of about 50 % was observed in inorganic LEDs.[56] Microlenses or additional coating layers on top of the glass surface, are further options to enhance the outcoupling of substrate modes.[56] These techniques however are an additional cost factor. The advantage of an organic thin film device is that the layers involved are easily patternable. This gives an opportunity to redirect modes trapped in the ITO/emissive layer. Bragg gratings are a common method to scatter specific modes out of a layer. Most often a grating structure is induced on the layer below, so that the emissive layer deposited on top adopts the pattern. The change in film thickness due to the corrugation below changes the effective refractive index, as the latter depends on the thickness. The periodic index change acts as a grating and the modes are diffracted out at different angles, see section 2.6.3. Using corrugated structures below the outcoupling efficiency of the emissive layer has been improoved.[110,111] However, they add additional processing steps or even an extra layer and complicate the device structure. The incorporation of the SRG directly onto the emissive layer is an alternative approach and could also be used for the feedback structures of organic DFB lasers.

In early work we noted that a surface relief grating (SRG) was spontaneously induced on irradiation of thin films of our light-emitting nematic LC with patterned UV light.[6] In this chapter we investigate this intriguing phenomenon in detail. The liquid crystal PV237 was chosen for the SRG experiments as it has a very low glass transition temperature of 0° and hence may be able to move at room temperature (RT). Between the glass transition and the melting point, the material crystallises but this may occur over very long timescales. Thin films were exposed with a laser through a phase mask. Different film thicknesses and crosslinking conditions were tested to maximise the grating depth and to control its period. An AFM was used to characterise the surface morphology. The compound PV318 was also investigated. Its molecular structure and transition temperatures are given in Chapter 4. The most interesting results obtained are presented and discussed with reference to a numerical model of the transmitted light through the phase mask. The origin of the SRG is also discussed.

6.1 Unexposed and Crosslinked Surfaces

Firstly AFM scans on an uncrosslinked area and areas crosslinked at RT and 65°C were conducted to ensure that the observed surface changes were not just due to the crosslinking process itself.

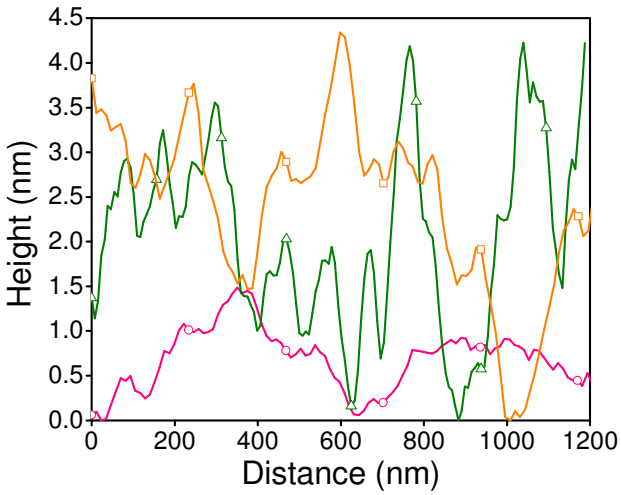

Figure 6.1: Surface roughness of an uncrosslinked PV237 layer (circles) and films crosslinked at RT (triangles) and at 65°C (squares).

In Figure 6.1 the surface morphology of areas crosslinked at RT and 65°C and an uncrosslinked area is shown. The crosslinked areas show a significant increase in roughness. The sample temperature during crosslinking has no great influence on the roughness. This increase in roughness is not typical. Other photopolymerisable LCs e.g. PV318 show a much smaller increase in roughness following crosslinking.[112]

With the help of the optical profiling system WYKO NT1100 by Vecco, which employs a non-contact white light interferometry, a 3D measurement of the surface profile up to several mm on the films is possible. Absolute measurements with the surface profiler made on soft surfaces like polymer - or LC films are unreliable as the profiler is designed to investigate thicker films made from harder substances like ceramics. The machine provides however an opportunity to directly compare uncrosslinked and crosslinked areas on the same film visually. A PV237 layer was crosslinked through a small slit at 65°C. A fluence of 1200 J/cm^2, which is twice the fluence required, was used to crosslink the stripe. Figure 6.2 shows a 3D picture of the films surface.

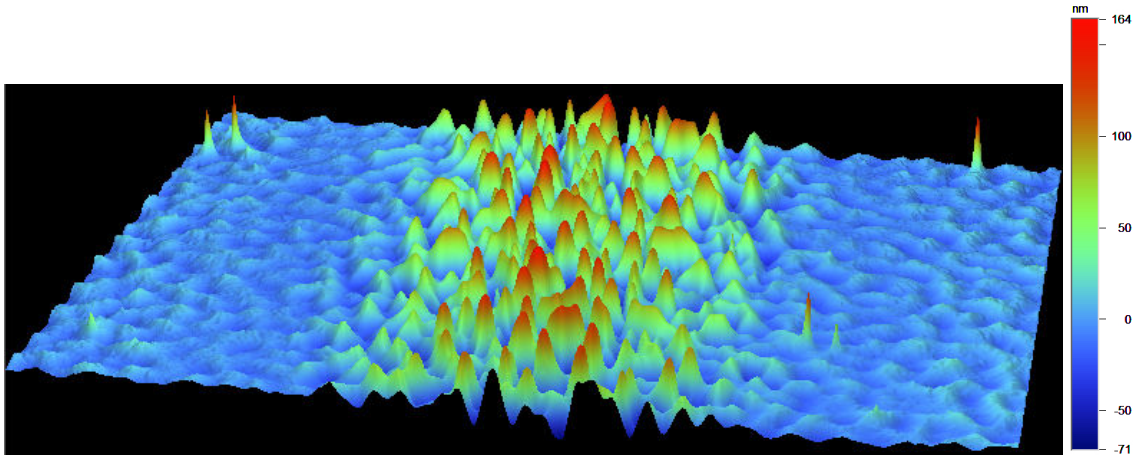

Figure 6.2: A 3D picture from a crosslinked stripe (middle) on an otherwise uncrosslinked (blue/green area) PV237 film. A glass slide with a PEDOT layer on top was used. as substrate. The picture was recorded with the optical profiler WYKO NT1100.

The crosslinked stripe in the middle is much rougher than the uncrosslinked area on the right and left. The random distribution of the peaks looks like a typical speckle pattern, which appears when light is reflected by a rough surface, thus is redirected in different directions and then interferes constructively or destructively.[113] A representative cross-section from left to right across the sample is plotted in Figure 6.3.

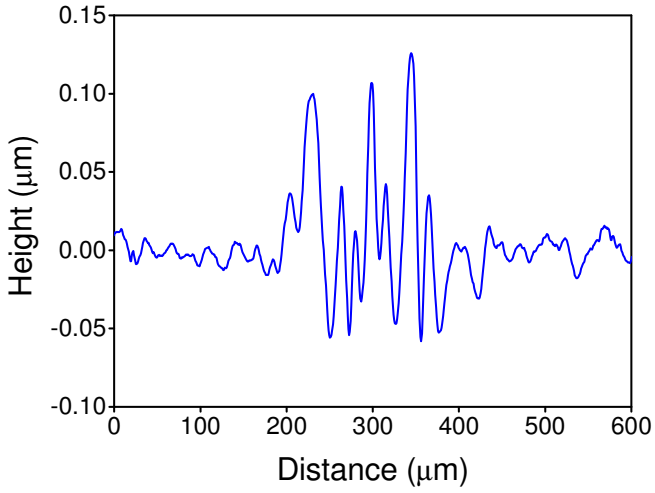

Figure 6.3: Horizontal cross-section of the surface shown in Figure 6.2. The crosslinked and much rougher area in the middle is about 200 µm wide.

The crosslinked stripe is about 200 µm wide. Its troughs are about 50 nm deep and its peaks between 40 and 120 nm high. The measured thickness of a PV237 film, which was prepared with the same settings, was about 80 nm ± 5 nm. The troughs and peaks possibly arise from the movement of the molecules from the trough area to form the peaks. The measured values are not reliable but it is clear that crosslinking changes the surface texture of the PV237 film. Furthermore no clear periodicity was visible. The induced roughness was random.

6.2 Photoinduced Surface Relief Gratings

Having ensured that the crosslinking procedure itself does not induce a periodic structure in the LC films, AFM measurements on the films crosslinked by irradiation through the two phase masks were carried out. For simplification a few abbreviations, summarised in Table 6.1, are used.

Table 6.1: Abbreviations used in Chapter 6.

Expression	Abbreviation
surface relief grating	SRG
revolutions per minute	rpm
room temperature	RT
phase mask	PM
PM grating vector is parallel to the polarisation of the crosslinking laser	∥ PM
PM grating vector is perpendicular to the polarisation of the crosslinking laser	⊥ PM
PM period	Λ_{pm}
crosslinked	X
uncrosslinked	UnX
cross-section	CS

The sample preparation and crosslinking settings are described in section 3.5 and background information on phase masks can be found in section 2.6.4. To avoid repetitions of the sample preparation the sample number S01, S02 etc. are referred to when discussing graphs and AFM pictures. The processing conditions for each sample as well as the main results obtained, are summarised in Table 6.2 towards the end of the grating section. As described in the experimental section, "∥ PM setting" means that the polarisation of the crosslinking laser was parallel to the grating vector of the phase mask. For the "⊥ PM setting", the polarisation was perpendicular to the PM vector. The (peak to peak) amplitude will be stated, which is the distance from peak to valley as a measure for the depth of any features.

The AFM scans are presented in two perspectives. The 2D view from the top allows a good judgement on the roughness of the surface structures. The 3D picture provides a better impression on the depth and smoothness of surface periodicities. To improve their presentation the 3D pictures were often rotated and hence might not match the direction of the 2D profile. Measured distances in graphs are normalised to Λ_{pm}. Two different PMs were employed. One was made to fit the wavelength of the laser that was used for the irradiation of the films and had a period of 530 nm. The other had a period of 1000 nm but was not designed for the irradiation wavelength and hence had a very large zero order contribution. For each PM two different alignments, ⊥ PM and ∥ PM were investigated.

6.2.1 Surface Relief Gratings with the 530 nm Phase Mask

The results obtained using the ⊥ PM setting are discussed first and then the results from the ∥ PM setting are given. Figure 6.4 shows an AFM scan from a LC film that was crosslinked through the 530 nm PM with ⊥ PM setting. The periodic corrugation of the surface is clearly visible.

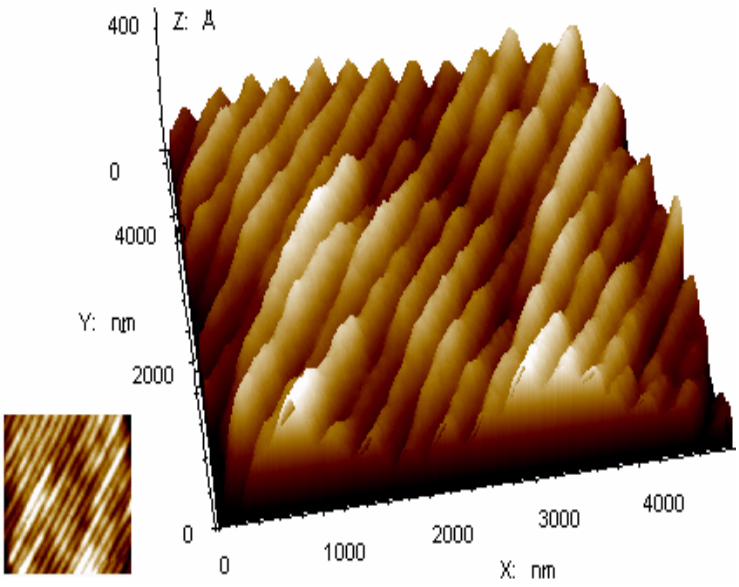

Figure 6.4: The inset shows the surface scan of a PV237 layer crosslinked by irradiation through the 530 nm period PM with ⊥ PM setting. The larger picture shows the same measurement in 3D. S09

From previous experiments it is known that the laser power is insufficient to ablate parts of the surface. It was therefore presumed that the LC molecules diffuse to illuminated regions during exposure. This presumption will be addressed again later in this section. The measured period was 291 ± 40 nm with a maximum amplitude of 10 nm. Including the error, the period corresponds to the expected value; half the period ($\Lambda_{pm}/2$) of the PM used, see Chapter 2.6. The sinusoidal interference pattern created by the PM hence was directly translated onto the surface. The large uncertainty range of ± 40 nm might be due to environmental influences like the vibrations in the glove box. Several different spots on the same perpendicular exposed area were measured giving a period of 520 ± 12 nm and amplitude of 28 nm. We will discuss later how these full periods can be accounted for. To ensure that the observed periods were correct the sample (S09) was also scanned with a scanning electron microscope (SEM), see Figure 6.5.

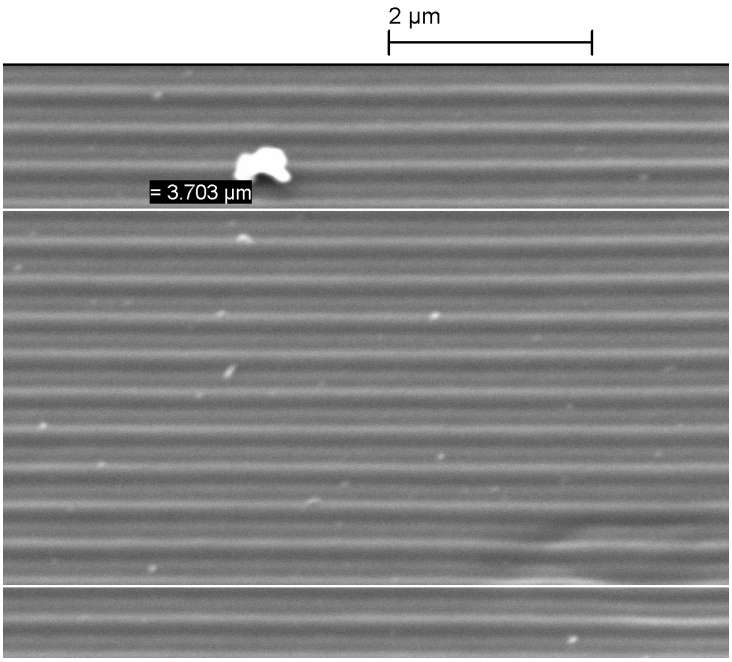

Figure 6.5: SEM scan of the surface scan of a PV237 layer crosslinked by irradiation through the 530 nm period PM with ⊥ PM setting. S09

The distance over 10 periods, indicated by the two white lines, was measured to be 3703 nm, hence 370.3 nm per period. The SEM beam hit the surface under an angle of 45° so with trigonometry the actual period is 370.3 nm/cos 45° = 523.68 nm. This corresponds to the value of 520 ± 12 nm measured with the AFM.

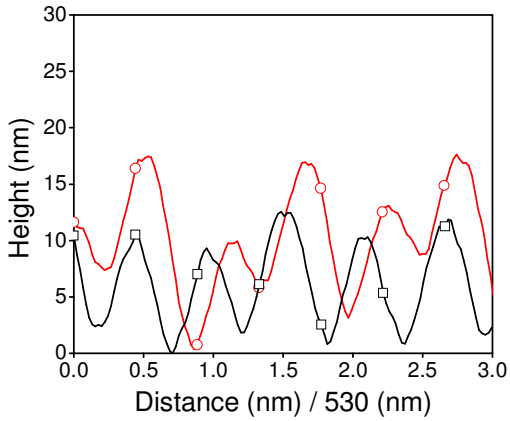

Figure 6.6: CSs of surface corrugations on PV237 layers crosslinked at 65°C by irradiation through the 530 nm PM with ⊥ PM setting. Both CSs were taken from sample S09. The squares show a CS directly taken from the AFM scan in Figure 6.4. The distance along the CS was normalised to the PM period.

A CS taken from Figure 6.4 (squares) is shown in Figure 6.6. The profile shows a relatively uniform corrugation of half the PM period and depth of about 10 nm. The

circles represent a profile with a sequence of smaller and larger peaks. The difference in peak height of 5 – 7 nm, which is almost a third of the tallest peak, is too great to neglect. Although small and large peaks vary with a periodicity of $\Lambda_{pm}/2$, this pattern overall was a period of Λ_{pm}. Figure 6.7 shows another example obtained with the ⊥ PM set up.

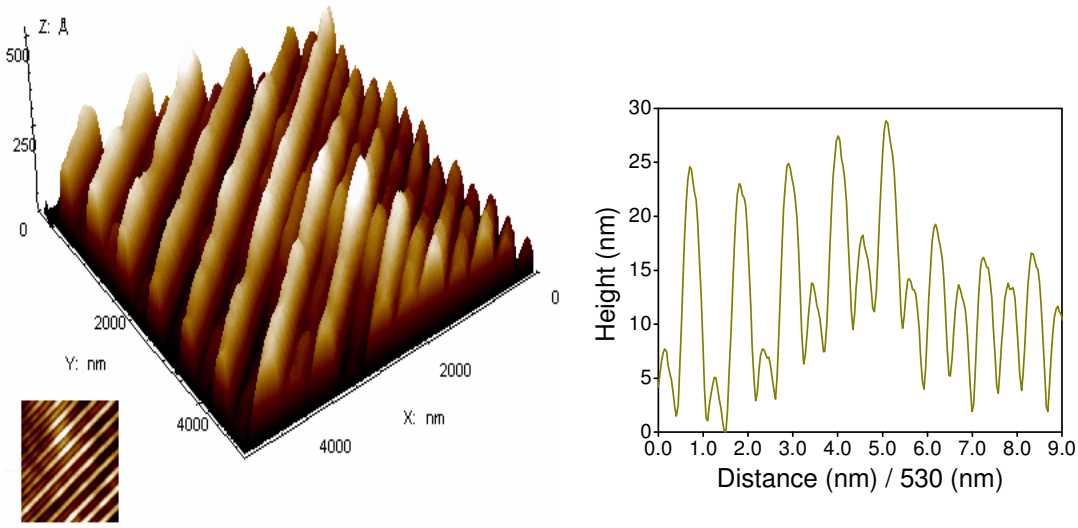

Figure 6.7: Left, an AFM scan of a PV237 layer crosslinked by irradiation through the 530 nm period PM with ⊥ PM setting. Inset shows the top view. Right, a CS taken from the AFM picture shows that the corrugation period changed from $\Lambda_{pm}/2$ to Λ_{pm}. S06

The 2D profile from a CS taken from the AFM picture is also shown. The corrugation period changes abruptly from Λ_{pm} (values 0 – 6) to $\Lambda_{pm}/2$ (values 6 – 9). This is a commonly known PM effect, which can occur when a tilt between PM and sample is present. [62]

The half period corrugation was measured to be 285 ± 15 nm with an average amplitude of 19 nm. The larger amplitude of 30 nm was measured on another spot, which showed a period of about 560 ± 30 nm. It is noticed that when the grating period doubles the peak height increases as well. This phenomenon was observed also with the parallel setting and the 1000 nm PM and will be addressed again later in this section. In Figure 6.8 the results obtained with the ∥ PM setting are presented.

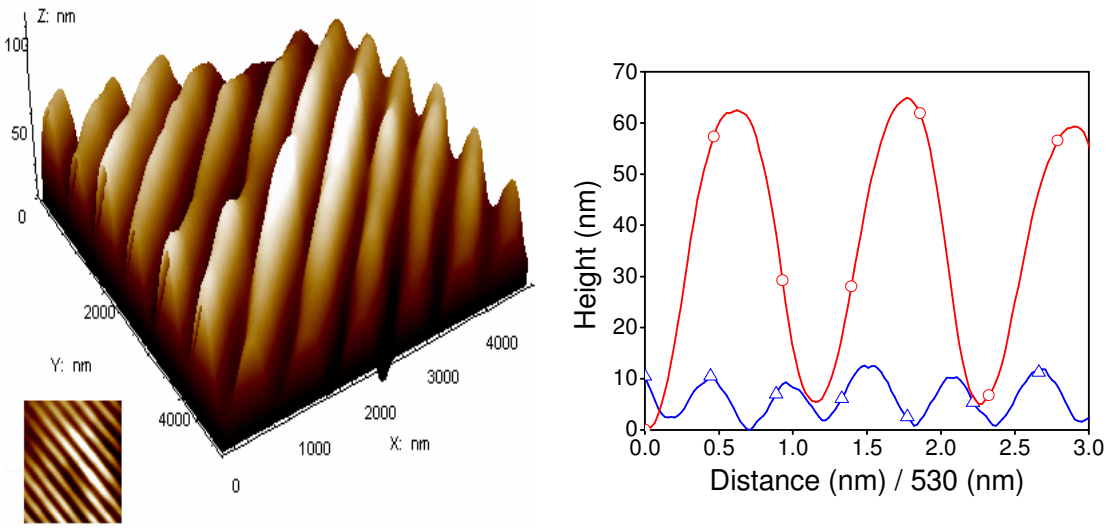

Figure 6.8: Left; an AFM scan of a PV237 layer crosslinked using the 530 nm PM with ∥PM setting. The inset shows the top view. Right; a CS taken from the AFM scan (circles) is plotted. For comparison the perpendicular CS from Figure 6.6 is shown as well (triangles). AFM scan and CSs are both from sample S09.

The corrugation obtained with the ∥ PM setting (circles) has a period of 591 ± 27 nm with an amplitude of 55 ± 5 nm. In most experiments with the parallel setting only full PM periods were achieved. This is due to the imperfect superposition of the two interfering beams (± 1st order) as their polarisation is at an angle and not parallel to each other. This matter will be addressed again in the simulation section of this chapter. For comparison the CS shown in Figure 6.6, obtained with the ⊥ PM setting, is also plotted (triangles). Here the observation that the larger the period the larger the peak height is very distinct. Both results are from the same film but the corrugation from the ∥ PM set up is 5 times deeper than the one from the ⊥ PM setting. The deepest grating obtained with the parallel setting was also measured on S09 and was 70 nm. In this case the period was found to be 385 ± 55 nm. This value is neither close to half the period nor to the full period of the PM. Its possible origin will be discussed at the end of the simulation section. The corresponding AFM scan is the one on the left in Figure 6.9.

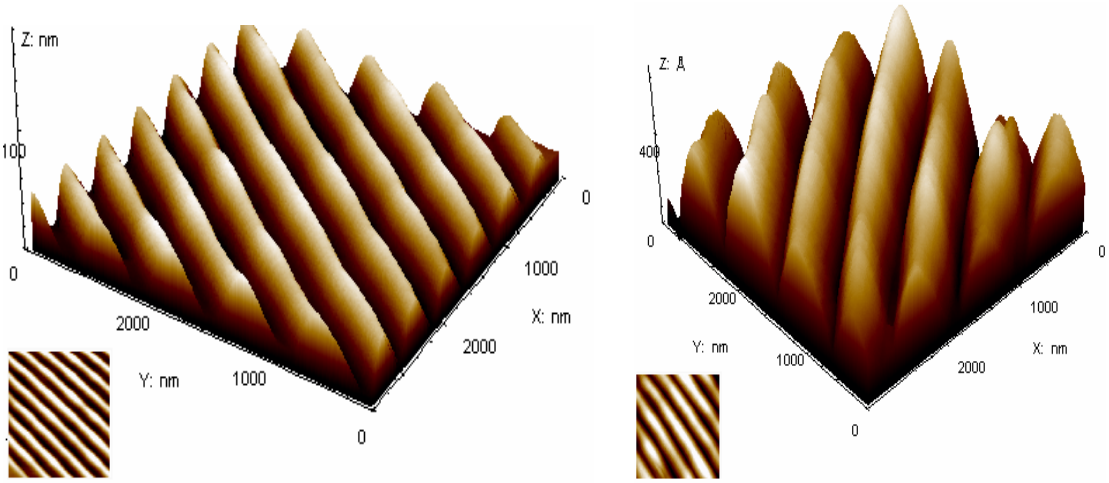

Figure 6.9: AFM scans of a PV237 layer crosslinked using the 530 nm PM with ‖ setting. On the left sample S09 and on the right S17 is shown.

On the right in Figure 6.9 a scan from sample S17 with a measured period of 570 ± 20 nm and amplitude of 56 nm is shown. As observed before and taking the error into account the grating period is significantly larger than the 530 nm period of the PM.

S08 was crosslinked at RT to determine whether the formation of the corrugation is temperature dependent. Furthermore this film was cured at 65° afterwards and then also washed to ensure that it was fully crosslinked by irradiation. The smallness of the AFM scan area (max. 10 µm x 10 µm) made it impossible to investigate the same spot twice after a treatment, so the grating depth before and after washing could not be compared. Figure 6.10 shows the results for the three different surface conditions. The slight curvature is most likely due to dragging of the AFM tip during the scan. This effect is often observed when soft surfaces are investigated and is therefore not considered further. The SRG was obtained with crosslinking at RT, which shows that an elevated temperature of 65°C is not essential to create a grating. Multiple experiments however show that uniformity and depth of the corrugation is improved when the film was heated during crosslinking. Regarding the 3D picture one can see that some of the corrugation peaks, almost every second row, are about 3 – 5 nm lower than the others. This is often observed and is due to imperfect PM alignment with respect of the laser polarisation as will be shown in the simulated section.

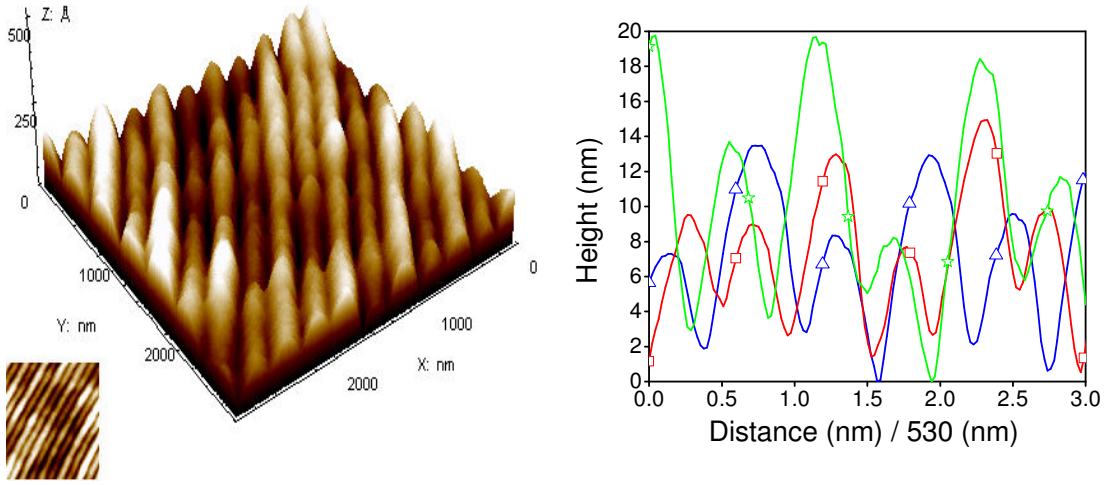

Figure 6.10: Left; AFM scan from the sample S08. The area was crosslinked at RT using the 530 nm PM aligned perpendicular. Right; CSs from the same area (not the same spot) after crosslinking (triangles), after curing at 65°C for 5 h (squares) and thereafter washing in toluene (stars).

As the CSs show no large difference in height could be found between the area crosslinked at RT and the area scanned after curing. A maximum amplitude of 22 and 24 nm respectively was found overall. The washing seems to increase the grating depth to 33 nm. The latter scan also shows that most of the film was crosslinked and rendered insoluble, as the corrugation itself remained. Similar results with the 530 nm PM (∥ and ⊥ PM setting) were also obtained with sample S11 concerning the curing after crosslinking.

6.2.2 Modelling of the 530 nm Phase Mask

As discussed in section 2.6.4 an ideal PM produces a sinusoidal irradiance pattern of period $\Lambda_{pm}/2$. The sinusoidal interference pattern behind the real PM was simulated using the software MathCad Professional 2001. In the model many different parameters like the distance between the mask and the substrate, the polarisation of the laser and the incomplete 0^{th} order suppression have to be considered. In 1995 Dyer et al. published an algorithm to calculate and visualise these dependencies.[62] A modified version of this model was produced by Dyer and by us to simulate our case concerning the laser polarisation direction with respect to the grating vector. The laser wavelength was set to be 325 nm with 1 mrad beam divergence and infinite coherence. The PM period was set to 530 nm. The refractive index behind the mask was equal to 1. The mask is assumed to be perfectly aligned so that no tilt was present. Experimental values for the power of the zero and ± 1 orders (5 mW and 22 mW respectively) were measured with a power

meter behind the PM and used in the simulation. For comparison simulations with a full 0^{th} order suppression were carried out as well. There the 0^{th} order was set to 0 and the ± 1 orders were kept equal to 22 mW. The axes were defined as displayed in Figure 6.11.

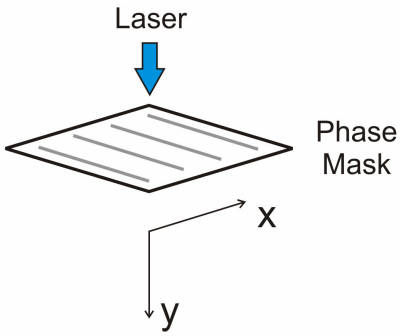

Figure 6.11: Axes definition used for the simulations.

In all presented results the values along the x and y axes were normalised to the PM period. The z axis represents the light intensity (in arbitrary units) behind the mask. One thus has to be careful when comparing experimental and simulated results as their axis definitions are not the same.

In Figure 6.12 the simulation results obtained with the laser polarisation perpendicular to the grating vector are shown. The interference pattern on the left was achieved with the experimental settings, the one on the right with full 0^{th} order suppression.

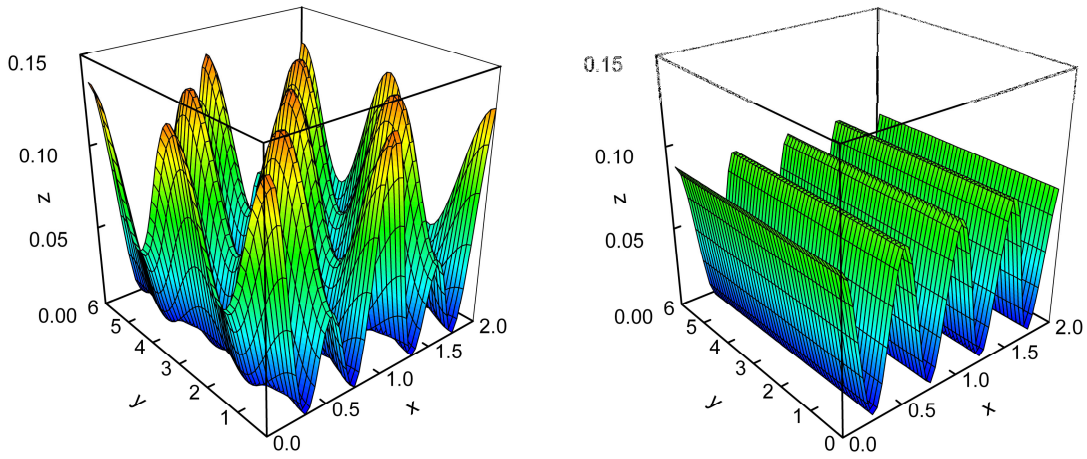

Figure 6.12: Power distribution (z) of light transmitted through the 530 nm mask with ⊥ PM setting, where x is parallel to the PM and y is the distance from the mask. Left: Experimental conditions. Right: Ideal case with complete 0^{th} order suppression. All distances are normalised to the PM period.

As expected from theory the experimental model shows a corrugation along the x axis with intensity peaks every half period. The height of the power peaks however varies periodically with increased distance (y) between mask and sample surface. The period is

3 times the PM period. This periodicity is due to the large 0^{th} order contribution as it disappears when the 0^{th} order is fully suppressed, as can be seen on the right of Figure 6.12. From the experimental model representative CSs were plotted in Figure 6.13 for three different y values. The CS at larger y values shows a repetition of the same pattern and are therefore not plotted.

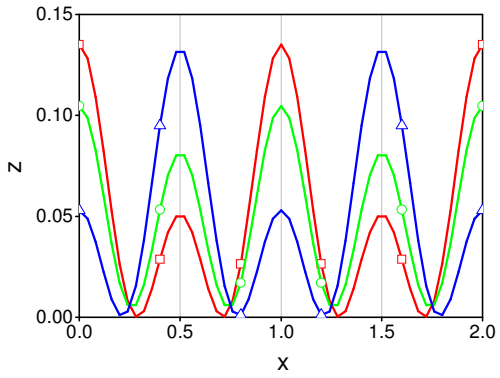

Figure 6.13: Cross-sections along the x-axis taken from the picture on the left of Figure 6.12 for three different distances. Red squares: y = 0, green circles: y = 0.75, blue triangles: y = 1.50.

The plots showed that a periodicity of half the PM period is maintained even with increasing sample – mask distance, but the relative peak heights change. For y = 0 every second peak is almost 3 times larger than the peaks in-between. For y = 0.75 the peaks heights were almost equal and for y = 1.5 the inverse case to y = 0 is observed. This explains the various gratings depths and periods obtained within the experiments, assuming that the grating profile reflects that of the laser power distribution. Depending on how close the sample was to the mask surface different power patterns were present. Great changes in the interference pattern are possible over a relative small change in distance. For example only 397.5 nm lie between y = 0 and y = 0.75. Considering that the LC films were not perfectly even and tilts between sample and mask, e.g. in Figure 6.7, were likely to be present the variations in grating amplitude found across the same crosslinked area also can be accounted for. Next the same simulations were carried out but with the ǁ PM setting. The results are displayed in Figure 6.14.

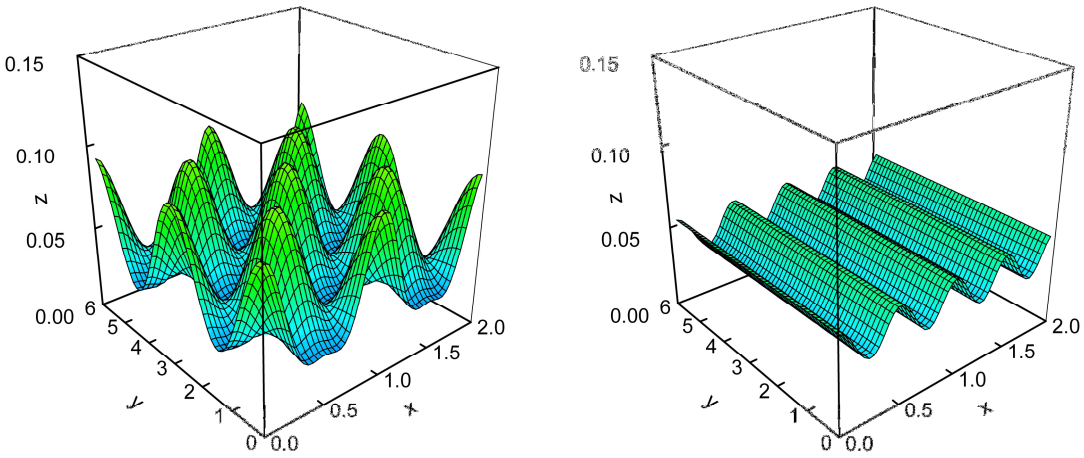

Figure 6.14:. Power distribution (z) of light transmitted through the 530 nm mask surface with ∥ PM setting, where x is parallel to the PM and y is the distance from the mask. Left: Experimental conditions. Right: Ideal case with complete 0^{th} order suppression. All distances are normalised to the PM period.

The contrast between the peaks and troughs of the power pattern is lower than for the perpendicular case. This makes sense as the two beams were not parallel polarised and partly cancelled each other out. The periodicity in the y direction is the same as for the perpendicular case but not in the x direction. From the experimental model representative CSs for three different y values are plotted in Figure 6.15.

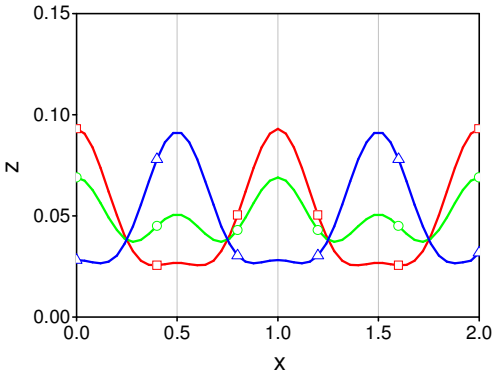

Figure 6.15: Cross-sections along the x-axis taken from the picture on the left of Figure 6.14 for three different distances. Red squares: y = 0, green circles: y = 0.75, blue triangles: y = 1.50.

Here the period is equal to Λ_{pm} for y values equal to 0 and 1.5. In-between these values the period halved, but the corresponding peaks are not very high. This explains why in most experiments with the ∥ PM setting only a full phase period could be measured with the AFM as it was much more likely that this pattern was present. The difference in peak height for the half period might also not have been big enough to create a distinctive surface corrugation.

The simulations give a good explanation why the AFM pictures often show a sequence of smaller and taller corrugation grooves for the ⊥ PM setting. Two out of the three CSs showed a distinctive height difference between alternate peaks; this corresponds to a spot behind the PM where the power distribution has the same profile. For the ∥ PM setting two out of three CSs showed a similar peak height with a period equal to Λ_{pm}, so it is much more likely to obtain an even corrugation of the same height with this setting. The simulations however cannot explain why deeper SRG are always obtained with the ∥ PM setting. This is unexpected as there is a smaller contrast between the peaks and troughs of the power distribution for the ∥ PM setting. Diffusion of monomer from troughs to peaks would reduce as the material viscosity is increased by crosslinking. We will discuss this issue in section 6.4. With the simulation the half and full periods observed could be accounted for. A number of possibilities were considered to explain the other periodicities, e.g. the 385 nm period from Figure 6.9, but the resultant change in the period was too small to explain the observed changes. For example an angular deviation when defining the cross-section perpendicular to the corrugation gives an error of less than a nm. An unintended tilt between sample and mask can cause jumps from full to half periods.[62] It may also give very small changes of about 1 - 3 nm in the period.[114] A 0^{th} order contribution creates a periodicity along the corrugation as shown above. The laser coherence only affects the aspect ratio of the sinusoidal power pattern behind the mask.[62] A false calibration of the AFM can be ruled out as well as then the periods observed would be consistently smaller or larger those predicted by the theory. Our results however showed both larger and smaller periods of different deviations. Based on this the experimental deviations from $\Lambda_{pm}/2$ or Λ_{pm} are more likely to be due to the LC material.

6.2.3 Surface Relief Gratings with the 1 μm Phase Mask

Similar experiments and simulations were carried out with a 1 μm PM as with the 530 nm PM. When evaluating the results one needs to consider that the PM was not made for the 325 nm laser wavelength and that the 0^{th} order was more than 6 times stronger than the ± 1^{st} orders. Furthermore weak ± 2^{nd} orders were also present. The perpendicular PM alignment did not deliver surface corrugations as promising as the parallel PM setting and was therefore not investigated further. For completeness one of the AFM measurements for the ⊥ PM configuration is shown in Figure 6.16.

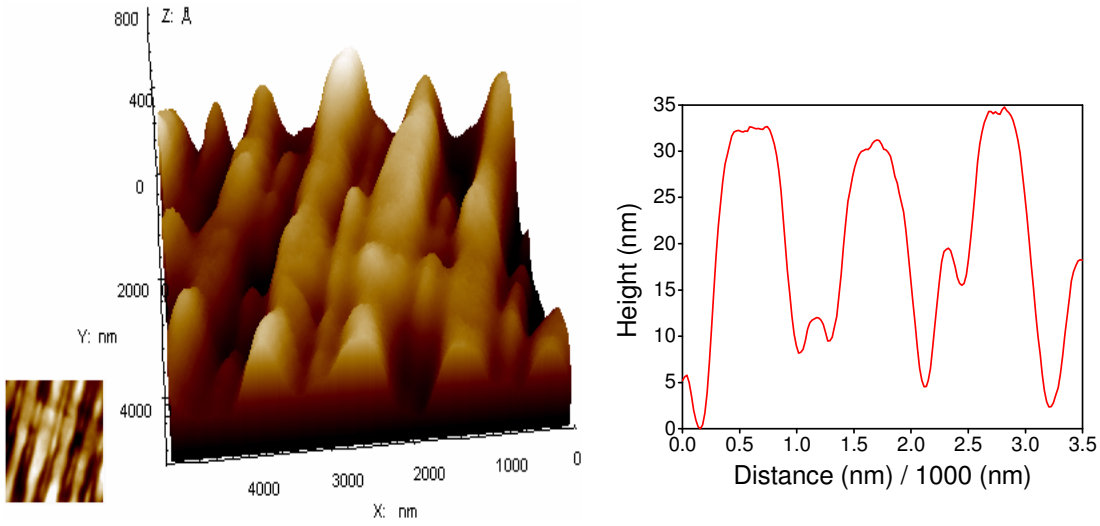

Figure 6.16: Left; AFM scan from a PV237 film crosslinked using a 1 µm PM at RT with the ⊥ PM setting. The inset shows the top view. Right; CS from the AFM scan. S11.

The average period measured was 1155 ± 45 nm with a maximum depth of 37 nm. The grating morphology is not very even in both directions along and perpendicular to the corrugation. The experiment was carried out at RT, so that high viscosity may explain the unevenness and the flatness of the peaks. A period of $\Lambda_{pm}/2$ is not clearly measurable, but a few smaller peaks in-between the larger peaks were visible. As reported for the 530 nm PM work the period was always slightly larger than theory predicted. Very even and deep corrugations were achieved with the PM grating vector aligned parallel to the laser polarisation. One example is shown in Figure 6.17.

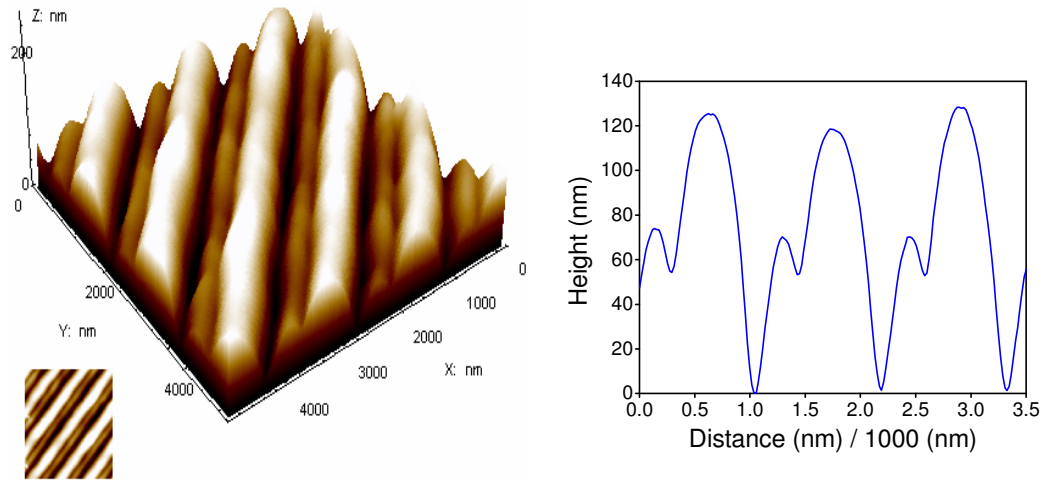

Figure 6.17: Left; AFM scan from a PV237 film crosslinked using a 1 µm PM with ∥ PM setting. The inset shows the top view. Right; CS from the AFM scan. S03.

This double peak, where a small peak is very close to a large peak, was observed in most of the experiments. The average period measured over several areas was 1190 ± 45 with a maximum peak to peak amplitude of 140 nm. It is interesting that the height

of the corrugation is 60 nm larger than the approximate film thickness of 80 nm. This is further proof that the corrugation definitely is not formed due to ablation. There must be mass transport of LCs from trough regions to the peaks.

Figure 6.18 shows another corrugation obtained with the 1 µm PM and ‖ setting.

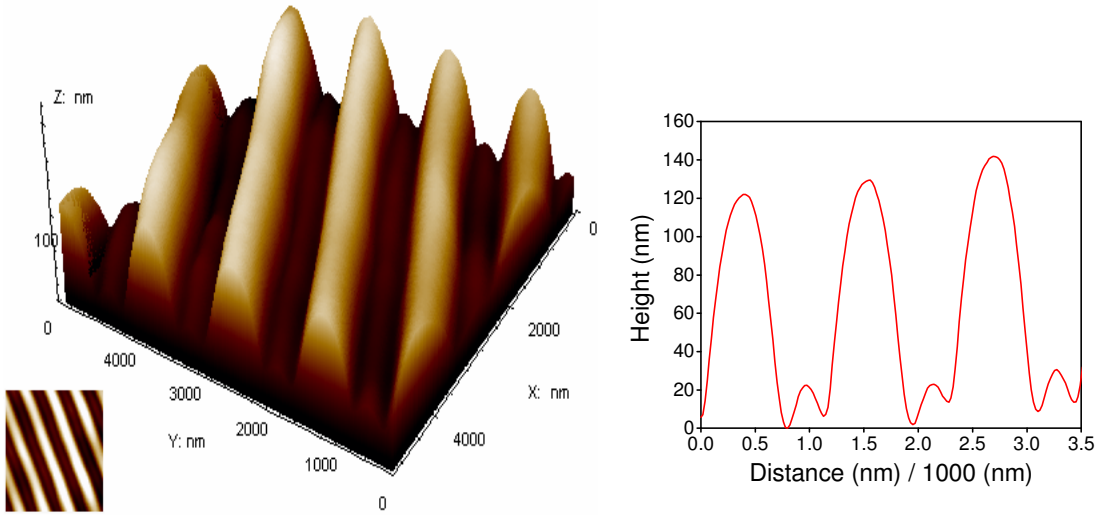

Figure 6.18: Left; AFM scan from a PV237 film crosslinked using a 1 µm PM with ‖ PM setting. The inset shows the top view. Right: CS from the AFM scan. S09

Again the period is larger than 1 µm. The average measured is 1216 ± 54 nm with a maximum amplitude of 140 nm. Here the double peak is not present but a small peak is still visible between the heights. In general the corrugations obtained with the 1 µm PM were deeper and much more even and smoother than the ones from the 530 nm PM.

Looking at all results presented in Table 6.2 and despite the variation in amplitude, we can conclude that the larger the period the deeper the corrugation. The film thickness itself, which is determined by concentration, solvent and spin speed, also influenced the grating amplitude. Concentrations of 0.03 mg/µl seemed to deliver the best results. Lower concentrations produced gratings of lower amplitude probably because the layer was too thin. Higher concentrations were tried but caused problems during film preparation, since the low glass transition temperature of PV237 results in recrystallisation. The solvent did not significantly influence the formation of the corrugation. Sample S03 was prepared with chloroform and showed similar results to sample S09, which was prepared with chlorobenzene. The latter was chosen as the solvent mainly used as it evaporates at a much higher temperature. Residual solvent present after the first heating cycle might increase the mobility of the LCs and so form higher gratings. This would be especially important for film exposures carried out at RT.

So far the grating formation seemed to be very insensitive to precise set up and imperfect phase masks since the 1 µm PM was not designed for the laser wavelength. A PV237 film was crosslinked using the 1 µm PM and a circularly polarised laser beam to check the influence of the polarisation.

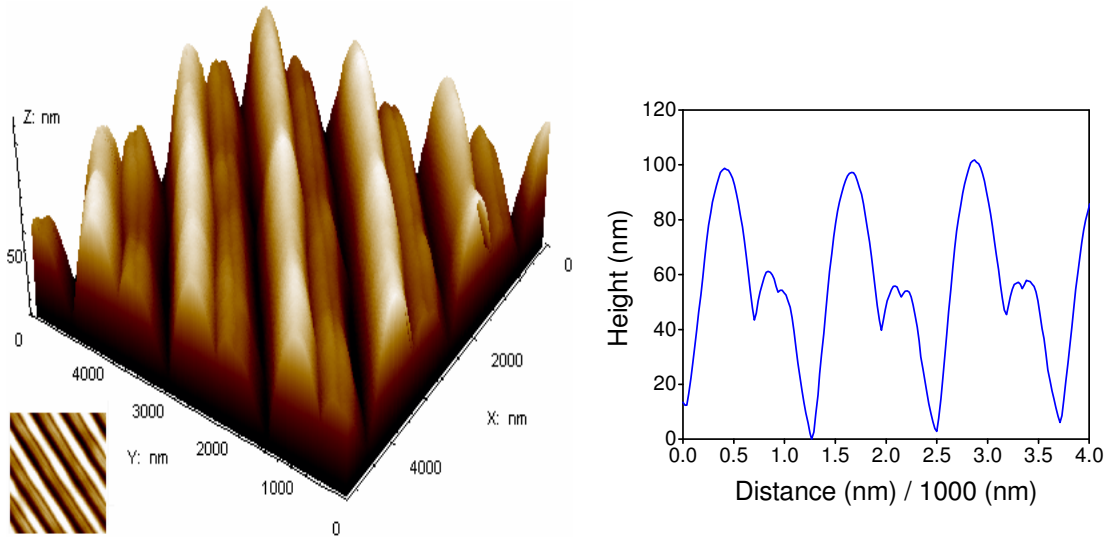

Figure 6.19: Left; AFM scan of a PV237 film crosslinked with a circularly polarised laser using a 1 µm PM. Right: CS across the AFM scan. S24

The periods measured varied greatly over the sample area, 1030 ± 220 nm with a maximum amplitude of 100 nm. It is however very promising that a linearly polarised laser is not necessary to pattern our liquid crystal films.

6.2.4 Modelling of the 1 µm Phase Mask

The interference patterns behind the mask for different substrate - mask distances were modelled for the 1 µm PM. One has to consider that the model does not consider that the 1000 nm PM was not made for the laser wavelength used. The contrast of the interference pattern behind the mask was therefore much lower in the experiments than in the model. However, the model can be used to check the influence of the large 0^{th} order contribution. The PM period was set to 1000 nm. The refractive index behind the mask was set equal to 1 and no tilt was present. Since the PM was larger the 2^{nd} orders were present and considered in the model. For the 0^{th} order 32 mW, for the ± 1 orders 5 mW and for the ± 2^{nd} orders 1 mW were used. The 2^{nd} order values were assumed as their exact measurement was difficult. In Figure 6.20 the simulation results for perpendicular and parallel PM alignment are shown.

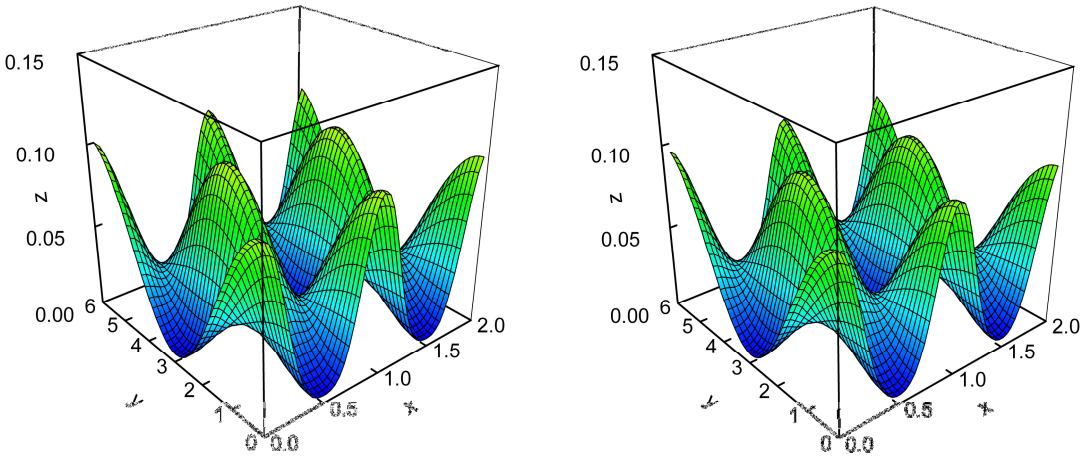

Figure 6.20: Power distribution (z) of light transmitted through the 1 µm PM surface with ∥ (left) and ⊥ (right) PM setting, where x is parallel to the PM and y is the distance from the mask. All distances are normalised to the PM period.

For the 1 µm PM there is hardly any difference in the calculated power distribution for parallel or perpendicular alignment. The periodicity of the interference pattern is equal to the Λ_{pm}. The position of the peaks varies with distance (y) from the PM. The same pattern was obtained for the circularly polarised beam. This is due to the weak 0^{th} order suppression. The 0^{th} order is about 6 times stronger than the $\pm 1^{st}$ orders. In Figure 6.21 CSs along the x-axis are taken from both simulations in Figure 6.20 at y = 0 are shown.

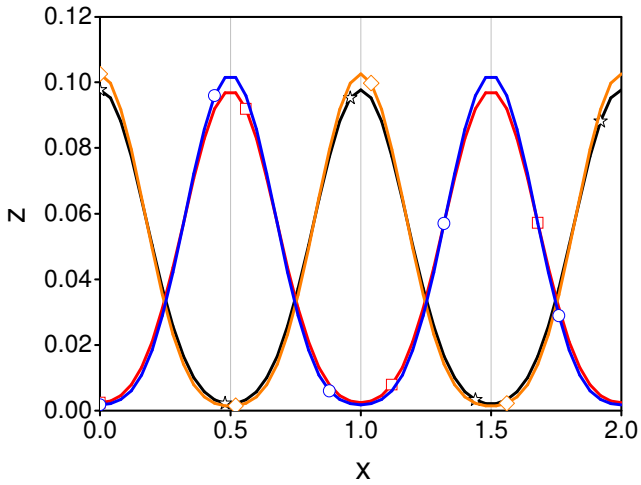

Figure 6.21: CSs along the x-axis from the pictures shown in Figure 6.21. Black stars (y = 0) and red squares (y = 3) show the parallel and orange rhombi (y = 0) and blue circles (y = 3) the perpendicular simulations.

Except for a minimal variation in the peak height there is no significant difference between the two PM settings. It is however notable that no $\Lambda_{pm}/2$ periodicity is observed, because of the large 0^{th} order contribution. It is noted that the peaks are displaced by

$\Lambda_{pm}/2$ in the x direction when y is changed, see Figure 6.20 and also CSs in Figure 6.21. Vibrations in the system may change the PM/surface displacement by 3 or more μm, which would account for double peaks seen in some surface profiles.

In Table 6.2 the processing conditions of the samples and their measured periods and maximum peak to peak amplitude are summarised.

Table 6.2: Sample processing conditions for PV237 films with measured grating periods and maximum peak to peak amplitudes.

Sample number	Film	Mask and Crosslink Conditions	Max. Amplitude (Max-Min) [nm]	Period of Surface Corrugation [nm]
S03	0.02 mg/µl chloroform 2000 rpm 30 s	1 µm PM, ∥to pol., X 400 J/cm^2 at 65°C	140	1190 ± 45
		cured at 65°C for 3h then 530 nm PM, ⊥ to pol. X 300 J/cm^2	11	286 ± 18
S06	0.02 mg/µl chlorobenzene 2000 rpm 30 s,	530 nm PM, ⊥ to pol. X 250 J/cm^2 at RT, then cured at 65°C for 4 h	8	305 ± 45
		cured at 65°C for 4 h then 530 nm PM, ⊥ to pol. X 250 J/cm^2 at 65°C	25 30	285 ± 15 560 ± 30
S08	0.03 mg/µl chlorobenzene 900 rpm 30 s	530 nm PM, ∥ to pol. X 600 J/cm^2 at RT	38	572 ± 15 624 ± 26
		530 nm PM, ⊥ to pol. X 600 J/cm^2 at RT	22	251 ± 32 324 ± 9
S08H	cured at 65°C for 5 h	530 nm PM, ∥ to pol. X 600 J/cm^2 at RT	42	589 ± 9
		530 nm PM, ⊥ to pol. 600 J/cm^2 at RT	24	282 ± 28
S08HW	washed after curing	530 nm, ∥ to pol. X 600 J/cm^2 at RT	42	487 ± 23 602 ± 6
		530 nm PM, ⊥ to pol. X 600 J/cm^2 at RT	33	325 ± 32
S09	0.03 mg/µl chlorobenzene 900 rpm 30 s	530 nm PM, ∥ to pol. X 600 J/cm^2 at 65°C	66 70	591 ± 27 385 ± 55
		cured 5 h at 65°C then 530 nm PM, ⊥ to pol. X 600 J/cm^2 at 65°C	28 10	520 ± 12 291 ± 40
		cured 10 h at 65°C then 1 µm PM, ∥to pol. X 600 J/cm^2 at 65°C	140	1216 ± 54
S11	0.02 mg/µl chlorobenzene 900 rpm 30 s	1 µm PM,∥ to pol. X 600 J/cm^2 at RT	75	861 ± 31 1212 ± 12

		530 nm PM, ⊥ to pol. X 600 J/cm^2 at RT	18	279 ± 11
		530 nm PM, ∥ to pol. X 600 J/cm^2 at RT	30	292 ± 20
		1 μm PM, ⊥ to pol X 600 J/cm^2 at RT	37	1155 ± 45
S11H	cured at 65°C for 12 h	1 μm PM, ∥ to pol.	50	616 ± 60
		530 nm PM, ⊥ to pol	21	220 ± 3 293 ± 10
		530 nm, ∥ to pol.	27	220 ± 10 280 ± 10
S12	0.02 mg/μl chlorobenzene 900 rpm 30 s	1 μm PM, ∥ to pol. X 600 J/cm^2 at 65°C	85	606 ± 40 1242 ± 50
S12H	cured at 65°C for 12 h	1 μm PM, ∥ to pol. X 600 J/cm^2 at 65°C	60	1083 ± 40
S17	0.03 mg/μl chlorobenzene 900 rpm 30 s	530 nm PM, ∥ to pol. X 600 J/cm^2 at 65°C	56	570 ± 20
		1 μm PM, ∥ to pol. X 600 J/cm^2 at 65°C	78	633 ± 25 1185 ± 15
		530 nm PM, ⊥ to pol. X 600 J/cm^2 at 65°C	30	290 ± 15
		1 μm PM, ⊥ to pol. X 600 J/cm^2 at 65°C	64	1252 ± 35
S24	0.03 mg/μl chlorobenzene 900 rpm 30 s	1 μm PM, circularly polarised X 600 J/cm^2 at 65°C	100	1030 ± 220

6.3 Grating with PV318

The compound PV237 was found to be very efficient to introduce surface relief gratings. Another material named PV318 was also tested. It is similar to PV237 in terms of its core and its green emissive colour. It is a monotropic LC with a high clearing temperature of 187°C and cools to a nematic glass. Its T_g is 25°C but the glassy phase is maintained indefinitely at RT in a thin film. The same compound/solvent ratio (0.03 mg/μl), type of solvent (chlorobenzene) and spin speed (900 rpm, 30 s), like for most of the PV237 films, were used to prepare the thin film, see Table 6.3.

Table 6.3: Processing conditions of a PV318 film for surface corrugation test.

Sample number	Film	Mask and Crosslink Conditions	Max. Amplitude (Max-Min) [nm]	Period of Surface Corrugation [nm]
S19	0.03 mg/µl, PV318 5°C/min to 65°C for 15 min	530 nm PM, ⊥ to pol. X 750 J/cm^2 at 65°C	5 - 10	580 ± 40

In Figure 6.22 the AFM scan of the PV318 film is shown. It shows a periodic structure although the corrugations were not very deep (average of 5 – 10 nm) or regular.

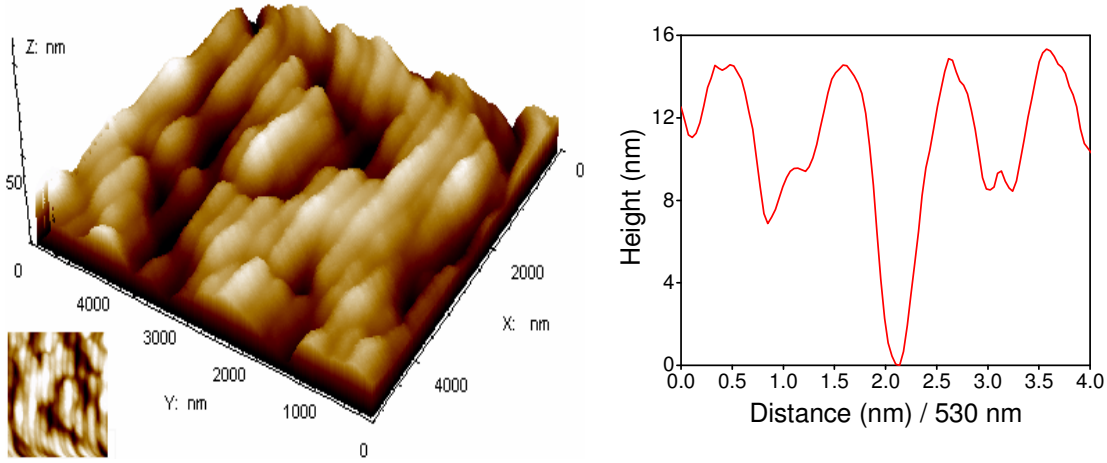

Figure 6.22: Left; AFM scan of a PV318 layer crosslinked using a 530 nm PM with ⊥ PM setting. Right; CSs of the AFM scan. (S19)

The compound PV318 is much longer than the PV237 molecule and has much higher transition temperature. The latter is much more mobile and needs less energy to move and form a grating. The film was also investigated with the optical beam profiler. There was no significant difference between un- and crosslinked area unlike the PV237 layer. Further investigations will be necessary to determine why the compound is photopatternable and which processes leads to the LC aggregation.

6.4 Absorption of Corrugated Films

We have shown that deeper SRGs are always obtained with the ∥ PM setting despite a low contrast in the spatial power distribution. Here we propose an explanation for this unexpected result. To investigate the effect of the induced surface relief grating on the

absorption spectrum, the polarisation ratio = (Absorbance ∥ / Absorbance ⊥) was measured for crosslinked and a non-crosslinked area and crosslinked corrugated areas with parallel and perpendicular PM settings. AFM first confirmed that a SRG was present. The normalised absorption spectra of these four areas are plotted in Figure 6.23.

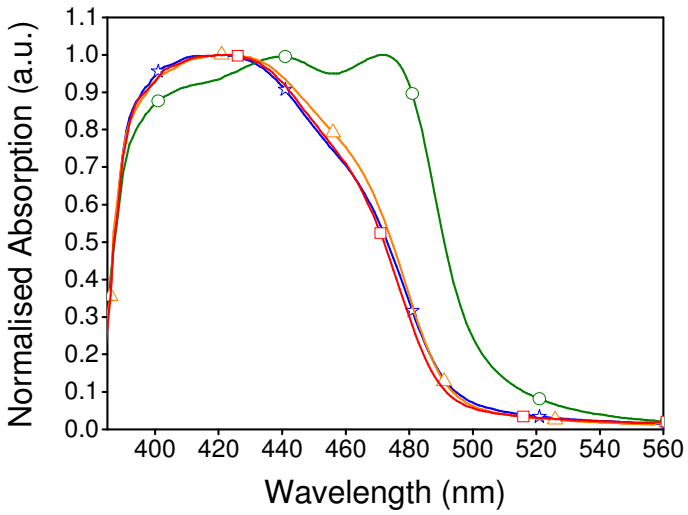

Figure 6.23: Normalised absorption spectra of a PV237 film. Areas; uncrosslinked (green circle), crosslinked (red square), crosslinked using the 530 nm PM aligned ∥ (orange triangle) and ⊥ (blue star).

The shape of the absorption curve changes significantly when the film was crosslinked. The peaks at 440 and 473 nm in the spectrum of the uncrosslinked area (circle) vanish and a new maximum around 418 nm arose when the film was crosslinked. The spectra of the crosslinked areas were very similar whether or not the PM was used, recalling the discussion in section 3.4.2 how dimerisation significantly changes the absorption spectrum. This suggests that the crosslinking process itself changes the arrangement of the LC molecules. Solvent effects could be another explanation, as during crosslinking any residual solvent could be evaporated. However this is unlikely since the films were cured at 65°C for a minimum of 12 h before the spectra were measured. A new molecular conformation is the more likely reason.

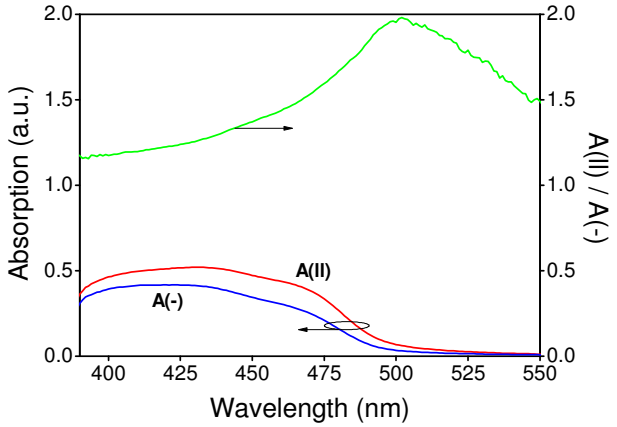

Figure 6.24: Absorption spectrum of a PV237 film crosslinked using a 530 nm PM with ∥ PM setting. The spectra were measured with a polarised beam, where the beam was either parallel A(ll) or perpendicular A(-) set up. The resultant polarisation ratio A(ll)/A(-) is also plotted.

Figure 6.24 shows the absorbance spectrum both parallel, denoted as A(∥), and perpendicular, denoted as A(-), to the polarisation direction of the incident beam for the area crosslinked through the PM with ∥ PM setting. A small anisotropy is obtained and the polarisation ratio increases with wavelength. The absorbance peaks at 430 nm and at this wavelength the polarisation ratio is 1.25.

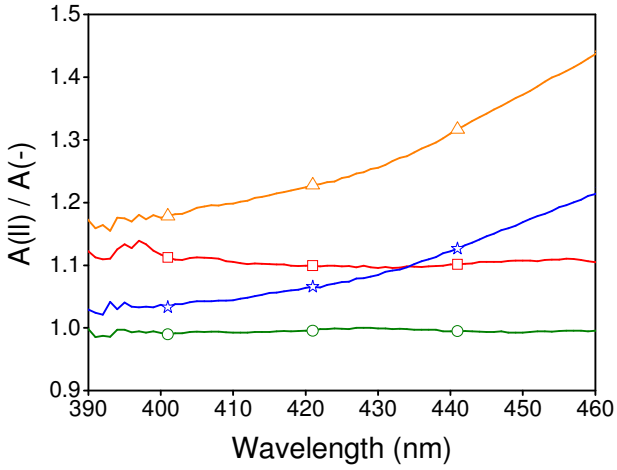

Figure 6.25: Polarised absorption ratio A(ll) / A(-) of a PV237 film. Areas; uncrosslinked (circle), crosslinked (square), crosslinked with the PM aligned parallel (triangle) and perpendicular (star).

Figure 6.25 shows the polarisation ratio as a function of wavelength for the four areas. The ratio values at 430 nm, the absorbance peaks, are used for comparison. No anisotropy could be detected for the uncrosslinked area (circle). Crosslinking itself introduced a small anisotropy as the ratio increased to 1.1 (squares). For the ⊥ PM

setting the polarisation ratio slightly decreases to 1.08 and increases to 1.25 for the ∥ PM setting. We also note that the polarisation of the crosslinking laser influences the alignment of PV237, aligned using an underlying PEDOT layer. This effect is unique to PV237.

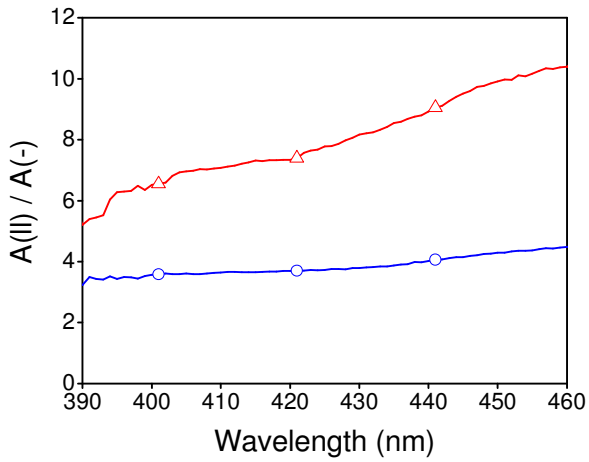

Figure 6.26: Polarised absorption ratio from an area that was crosslinked with the laser polarisation perpendicular (circles) and parallel (triangles) to the alignment direction. Both measurements were done on the same film (PV237/MPA153 blend ratio 1:1) on rubbed PEDOT.

Figure 6.26 shows that when the laser polarisation is perpendicular to the rubbing direction, the polarisation ratio is lower than the ratio obtained with the polarisation parallel to the rubbing direction. Assuming that the LCs aligned parallel to the rubbing direction one can conclude that they also preferably align parallel to the laser polarisation. Our polarised absorbance results show that crosslinking through the PM with polarised light partially reorients the film in the direction of the incident polarisation. The effect is larger for the ∥ PM setting, which also produces deeper groves, than for the ⊥ PM setting. We suggest a mechanism to explain both phenomena based on anisotropic photopolymerisation. No photo-initiator is present in the LC film suggesting that the crosslinking process is self-initiated by the chromophore. We have shown elsewhere that the self-initiation does not proceed by fragmentation of the aromatic core and suggested instead that it may occur via thermally assisted energy transfer from the excited state of the aromatic core to the crosslinking group.[9] Chromophores parallel to the polarisation direction of the incident beam are preferentially excited. Assuming a short range energy transfer to the diene group of the excited mesogen, their alignment will be locked in by crosslinking with neighbouring monomers. The alignment is enhanced by the cooperative reorientation of nearest

neighbours resulting from the self-assembly properties of nematics. The shear viscosity of nematic LCs is anisotropic and is minimised for translation parallel to the director.[115] Hence monomers aligned perpendicular to the grating grooves can flow more easily into the more highly crosslinked regions of the film than those oriented parallel to the grooves. Therefore the photoinduced polarisation is larger and the grating depth larger for irradiation with the ∥ rather than the ⊥ PM setting. As illustrated in Figure 6.27, mass diffusion towards the peaks is easier for the former.

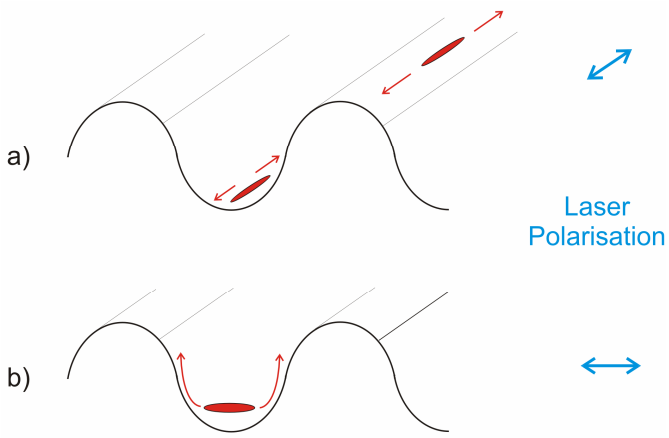

Figure 6.27: Preferred LC monomer movement for a) ⊥ PM alignment, where the laser polarisation is parallel to the grooves and for b) ∥ PM alignment, where the laser polarisation is perpendicular to the grooves.

In conclusion we have demonstrated for the first time the imprinting of semiconducting organics by photoinduced mass transfer. This non-contact method is highly desirable as organic layers are very sensitive to physical contact. Photoembossed surface relief structures have previously been formed in non-semiconducting photopolymers used for holography.[116, 117, 118] The photopolymer layer is irradiated with spatially modulated UV light, creating radicals in the illuminated areas. The free radicals are captured in the glassy matrix but monomer diffusion to the reactive sites is restricted. After exposure the sample is heated above a threshold temperature, where the sample changes from a solid to a more mobile, liquid-like state. The polymerisation of the monomer in the exposed areas changes the chemical potential and provides a driving force for the monomers to diffuse from the unexposed to the exposed areas. A similar effect is seen here but no curing step is required. The mass transport creates a volume increase and, consequently, a surface relief structure. The photoembossing of surface relief structures has also been demonstrated by polymerization of a dielectric nematic liquid crystals monomer blend.[119] The material was locally irradiated in the nematic phase to produce a latent image which developed into a topological feature by annealing above the clearing

point. Our material moves at room temperature, which is much lower than the clearing point of 103°C. Surface structures can also be reversibly formed in materials containing azobenzene moieties or other photoisomerisable groups.[120, 121] Indeed an azo-containing polymer was deposited on top of a dye doped organic gain media to provide feedback in a distributed feedback laser.[122] The laser characteristics were poor because of the poor overlap with the grating. The azo-group has a major disadvantage in that it quenched luminescence and so could not be incorporated in the gain medium.

Several approaches have been made to pattern the polymers directly to provide distributed feedback for organic lasers. A soft lithography technique, called hot embossing is one option. The polymer is spin coated on a substrate and heated above its glass transition temperature. Then a master with the desired periodic pattern is pressed onto the polymer film. The polymer flows around the master and adopts its shape and is then cooled down so that the structure is maintained when the master is removed afterwards.[123] With this technique a period of 400 nm with a depth of 20 nm was embossed into a polymer film made of poly[2-methoxy-5-(3',7'-dimethyloctyloxy)1,4 paraphenylenevilylene] (OC_1C_{10}-PPV).[123] The disadvantage here is that the polymer film gets into contact with the master. Photolithography was used to directly pattern a polymer layer. P. Visconti et al. applied the photoresist directly on a thick poly(p-phenylenevinylene) (PPV) layer and removed parts of the PPV via plasma etching. Depths of at least 120 nm with a period of 500 nm could be achieved.[124] Again however the organic layer gets into contact with another material and additional processing steps as spin coating, photolithography, developing, etching and cleaning are involved. SRG can also be created via a corrugated layer beneath the actual semiconducting layer.[4] Additional layers however might affect the device performance and require additional processing steps. A SRG with a period of 288nm and a depth of 30 nm with the conducting polymer spin-coated on top was found to provide sufficient feedback for an optically pumped organic laser.[125] The highest corrugation depth of 30 nm achieved with our material for the small period of 290 nm is therefore deep enough to act as a feedback structure.

6.5 Summary Chapter 6

In conclusion our semiconducting LC PV237 proved to be highly suitable for photopatterning. Periodic structures could be formed when the films were irradiated

with sinusoidal intensity pattern, which was created by a phase mask. Surface relief grating (SRG) depths of 140 nm for periods of about 1200 nm, 25 nm for periods around 280 nm and 66 nm for periods around 580 nm were achieved. The gratings were formed through photoinduced mass transfer of the molecules to the illuminated areas on the exposed LC film. The anisotropic properties of the nematic phase enhance mass transfer when the incident beam is polarised parallel to the direction of motions. Our light emitting LC PV237 crosslinks when exposed with ultraviolet light and films made from it are rendered insoluble. This makes our LC an excellent candidate for feedback structures in organic lasers and multilayered devices.

7 Conclusion and Outlook

We have carried out semiempirical quantum mechanical simulations on monomer and anti-cofacial dimer configurations of our molecules. The former represents the molecules is solution and the latter those in a thin film. The oscillator strengths in a dimer increases by a factor of 2 compared to the monomer for longitudinal offsets larger than 20 Å. For smaller shifts the transition from ground to excited state is forbidden so that quenching of luminescence can be expected for this configuration. This agrees with the optical quantum efficiency results obtained that show a decrease in efficiency in the solid state, taking into account that the material is nematic with a range of offsets present. The dimer simulations give an insight on how molecular energies and transitions are affected when molecules are brought closely together. The simulations however only represent one of many possible dimer configurations. Further calculations on different dimer arrangements with e.g. a larger separation or trimer configurations could be carried out to get an improved perspective.

Mixtures of our LCs showed nematic phases at room temperature frozen in a glassy state. Hence no phase separation occurred and a homogeneous blend was obtained. We have shown that white electroluminescence (EL) could be achieved from homogeneous blends of blue/green and red liquid crystalline (LC) emitters. Furthermore polarised white EL with an average polarisation ratio of 8:1 and a maximum of 12.5:1 was realised. The low device efficiency is probably due the poor performance of the red emitter. The design of new red emitters with improved efficiency is necessary before further investigation on the white light can be carried out. Commercial applications require long term stability in colour, brightness and efficiency. Our materials are sensitive to air and humidity, hence the purity of the materials and the encapsulation of OLEDs are important factors. OLED production under clean room conditions would deliver a much better insight in terms of the stability of the devices made from our LCs.

Thin films made from the semiconducting LC PV237 spontaneously formed surface relief gratings upon UV irradiation with a sinusoidal intensity pattern. Depths of 140 nm for periods in the μm-range, 25 nm for periods around 280 nm and 66 nm for periods around 580 nm were achieved. The corrugation was formed through photoinduced and anisotropic mass transport from the dark to the illuminated regions. PV237 crosslinkes upon exposure and is therefore rendered insoluble. The material is therefore suitable to form feedback structures for organic lasers and to enhance the outcoupling of trapped modes in OLEDs. Though another LC with a similar core could also be photopatterned the result showed a much lower aspect ratio. Therefore further investigations on PV237 and on different LCs are necessary to determine why the mass transport is so efficient in PV237 films. A holographic set up is preferable to form the SRG to eliminate problems with phase mask, such as low contrast, tilt and polarisation sensitivity, contact and lack of control of the grating period. Derivatives of PV237 with different side and end chains could be synthesised to compare their ability to form corrugations. A surface investigation on crosslinked and non-crosslinked areas of new material with a beam profiler offers a quick method to determine whether mass transport takes place during irradiation or not. A scanning electron microscope allows larger scan areas so that the grating formation over a longer range can be investigated. OLEDs made from corrugated films can be examined for changes in the emission spectrum and an enhanced outcoupling efficiency can be observed. Similarly the SRG can be optically pumped with a laser to record photoluminescence under different angles to check its suitability as a distributed feedback structure in organic lasers.

8 References

[1] U. Mitschke and P. Bauerle, "The electroluminescence of organic materials," J. Mater. Chem. **10** (7), 1471-1507 (2000).

[2] R.H. Friend, "Electroluminescence in conjugated polymers," Nature **397**, 121-128 (1999).

[3] IOP, "LED Quarterly Insights: Cost and Manufacture," TechnologyTracking (2007).

[4] B. Matterson and I.D.W Samuel, "Increased Efficiency and Controlled Light Output from a Microstructured Light-Emitting Diode," Advanced Materials **13** (2), 123-127 (2001).

[5] B. M. Medina, A. Van Vooren, P. Brocorens et al., "Electronic structure and charge-transport properties of polythiophene chains containing thienothiophene units: A joint experimental and theoretical study," Chemistry Of Materials **19**, 4949-4956 (2007).

[6] K. L. Woon, A. E. A. Contoret, S. R. Farrar et al., "Material and device properties of highly birefringent nematic glasses and polymer networks for organic electroluminescence," J. Soc. Inf. Disp. **14** (6), 557-563 (2006).

[7] M. P. Aldred, R. Hudson, S.P. Kitney et al., "Electroluminescent Segmented Liquid Crystalline Trimers," Liquid Crystals (2008).

[8] A. Liedtke, M. O'Neill, A. Wertmoller et al., "White-light OLEDs using liquid crystal polymer networks," Chem. Mat. **20** (11), 3579-3586 (2008).

[9] K. L. Woon, A. Liedtke, M. O'Neill et al., "Photopolymerization studies of a light-emitting liquid crystal with methacrylate reactive groups for electroluminescence," SPIE **7050**, E500-E500 (2008).

[10] M. Pope, H. P. Kallmann, and P. Magnante, "Electroluminescence in Organic Crystals," Chemical Physics **38**, 2042 (1963).

[11] C. W. Tang and S. A. VanSlyke, "Organic electroluminescent diodes," Applied Physics Letters **51** (12), 913-915 (1987).

[12] http://komar.cs.stthomas.edu/qm425/01s/Tollefsrud2.htm.

[13] D. P. Medialdea, N. Bennis, B. Cerrolaza et al., "PEDOT as an alignment layer and electrode in AFLC devices," Opto-Electron. Rev. **17** (1), 78-83 (2009).

[14] Y.D. Jin, "Role of LiF in polymer light-emitting diodes with LiF-modified cathodes," Organic Electronics **5** (6), 271-281 (2004).

[15] L.S. Hung, "Enhanced electron injection in organic electroluminescence devices using an Al/LiF electrode," Applied Physics Letters **70** (2), 152 (1997).

[16] M. O'Neill and S. M. Kelly, "Liquid Crystals for Charge Transport, Luminescence, and Photonics," Advanced Materials **15** (14), 1135-1146 (2003).

[17] P. Yeh and C. Gu, *Optics Of Liquid Crystal Displays*. (John Wiley & Sons, Inc., Wiley, 1999).

[18] SHARP, *http://www.sharpsma.com/lcd/lcdguide/Primer/crystal-intro.php*.

[19] A. A. Collyer, *Liquid Crystal Polymers: From Structures to Applications*. (Elsevier Science Publishers LTD, 1992).

[20] A.M. Donald and A.H. Windle, *Liquid crystalline polymers*. (Cambridge University Press, 1992).

[21] http://plc.cwru.edu/tutorial/enhanced/files/lc/phase/phase.htm.

[22] S. Singh and D.A. Dunmur, *Liquid Crystals: Fundamentals*. (World Scientific Publishing Co. Pte. Ltd., 2002).

[23] http://www.3dlens.com/shop/polarizer.php.

[24] M. P. Aldred, A. J. Eastwood, S. M. Kelly et al., "Light-emitting fluorene photoreactive liquid crystals for organic electroluminescence," Chemistry Of Materials **16** (24), 4928-4936 (2004).

[25] A. E. A. Contoret, S. R. Farrar, M. O'Neill et al., "The photopolymerization and cross-linking of electroluminescent liquid crystals containing methacrylate and diene photopolymerizable end groups for multilayer organic light-emitting diodes," Chemistry Of Materials **14** (4), 1477-1487 (2002).

[26] A. E. A. Contoret, S. R. Farrar, P. O. Jackson et al., "Polarized electroluminescence from an anisotropic nematic network on a non-contact photoalignment layer," Advanced Materials **12** (13), 971-+ (2000).

[27] M. P. Aldred, A. E. A. Contoret, S. R. Farrar et al., "A full-color electroluminescent device and patterned photoalignment using light-emitting liquid crystals," Advanced Materials **17** (11), 1368-+ (2005).

[28] C. D. Muller, A. Falcou, N. Reckefuss et al., "Multi-colour organic light-emitting displays by solution processing," Nature **421** (6925), 829-833 (2003).

[29] K. L. Woon, M. P. Aldred, P. Vlachos et al., "Electronic charge transport in extended nematic liquid crystals," Chemistry Of Materials **18** (9), 2311-2317 (2006).

[30] M. Carrasco-Orozco, W. C. Tsoi, M. O'Neill et al., "New photovoltaic concept: Liquid-crystal solar cells using a nematic gel template," Advanced Materials **18** (13), 1754-+ (2006).

[31] J.C. deMello and R.H. Friend, "An improved experimental determination of external photoluminescence quantum efficiency," Advanced Materials **9** (3), 230-232 (1997).

[32] W. B. Smith, Introduction to Theoretical Organic Chemistry and Molecular Modeling. (VCH Publishers, Inc., 1996).

[33] D. O. Hayward, *Quantum Mechanics for Chemists*. (The Royal Society of Chemistry, Cambridge, 2002).

[34] P.W. Atkins, *Physical Chemistry*. (Oxford University Press, 1998).

[35] F.J. Keller, W.E. Gettys, and M.J. Skove, *Physics: Classical and Modern*, 2 ed. (McGraw-Hill, Inc., 1993).

[36] T.W. Graham Solomons, *Organic Chemistry*. (John Wiley & Sons, Inc., 1996).

[37] E. Hückel, "Quantentheoretische Beiträge zum Benzolproblem," Zeitschrift für Physik A Hadrons and Nuclei **70** (3-4), 204-286 (1931).

[38] E. Hückel, "Quantentheoretische Beiträge zum Problem der aromatischen und ungesättigten Verbindungen. III," Zeitschrift für Physik A Hadrons and Nuclei **76** (9-10), 628-648 (1932).

[39] J. L. Bredas, J. P. Calbert, D. A. da Silva et al., "Organic semiconductors: A theoretical characterization of the basic parameters governing charge transport," Proceedings Of The National Academy Of Sciences Of The United States Of America **99** (9), 5804-5809 (2002).

[40] J. L. Bredas, D. Beljonne, V. Coropceanu et al., "Charge-transfer and energy-transfer processes in pi-conjugated oligomers and polymers: A molecular picture," Chemical Reviews **104** (11), 4971-5003 (2004).

[41] J. Cornil, I. Gueli, A. Dkhissi et al., "Electronic and optical properties of polyfluorene and fluorene-based copolymers: A quantum-chemical characterization," Journal Of Chemical Physics **118** (14), 6615-6623 (2003).

[42] Z. B. Maksić and G. Alagona, Theoretical Models of Chemical Bonding Part 3: Molecular spectroscopy, electronic structure, and intramolecular interactions. (Springer Science & Business, 1991).

[43] B. Van Averbeke, D. Beljonne, and E. Hennebicq, "Energy transport along conjugated polymer chains: Through-space or through-bond?" Advanced Functional Materials **18**, 492-498 (2008).

[44] A. Van Vooren, V. Lemaur, A. J. Ye et al., "Impact of bridging units on the dynamics of photoinduced charge generation and charge recombination in donor-acceptor dyads," Chemphyschem **8** (8), 1240-1249 (2007).

[45] M. J. S. Dewar, E. G. Zoebisch, E. F. Healy et al., "The Development And Use Of Quantum-Mechanical Molecular-Models.76. Am1 - A New General-Purpose Quantum-Mechanical Molecular-Model," Journal Of The American Chemical Society **107** (13), 3902-3909 (1985).

[46] J. J. P. Stewart, "Optimization Of Parameters For Semiempirical Methods.1. Method," Journal Of Computational Chemistry **10** (2), 209-220 (1989).

[47] J. J. P. Stewart, "Optimization Of Parameters For Semiempirical Methods.2. Applications," Journal Of Computational Chemistry **10** (2), 221-264 (1989).

[48] Reviews in Computational Chemistry. (John Wiley & Sons, 1991).

[49] W. Bludau, *Halbleiter-Optoelektronik*, 2 ed. (Carl Nanser Verlag München Wien, 1995).

[50] M. Schwoerer and H.C. Wolf, *Organic Molecular Solids*. (Wiley-VCH, 2007).

[51] J. M. Hollas, *Modern Spectroscopy*, 4 ed. (John Wiley & Sons, Ltd, 2007).

[52] N.J. Turro, *Modern Molecular Photochemistry*. (University Science Books, 1991).

[53] T.A. Skotheim, R.L. Elsenbaumer, and J.R. Reynolds, *Handbook of conducting polymers*, 2 ed. (Marcel Dekker Inc., 1998).

[54] E.R. Menzel, *Fingerprint detection with lasers*, 2 ed. (Marcel Dekker Inc., 1999).

[55] V. Cleave, G. Yahioglu, P. Le Barny et al., "Harvesting singlet and triplet energy in polymer LEDs," Advanced Materials **11** (4), 285-288 (1999).

[56] N.K. Patel, "High-efficiency organic light-emitting diodes," IEEE Journal on selected topics in Quantum Electronics **8** (2), 346 (2002).

[57] T. Förster, "Zwischenmolekulare Energiewanderung und Fluoreszenz," Annalen der Physik **437** (1-2), 55-75 (1948).

[58] P. Atkins, *The Elements of Physical Chemistry*, 3 ed. (Oxford University Press, 2001).

[59] D.L. Dexter, "A Theory of Sensitized Luminescence in Solids," The Journal of Chemical Physics **21** (5), 767-962 (1953).

[60] J.R. Lakowicz, "Principles of Fluorescence Spectroscopy," (1999).

[61] J. B. Birks, *Photophysics of Aromatic Molecules*. (Wiley-Interscience, 1970).

[62] P.E. Dyer, "Analysis of grating formation with excimer laser irradiated phase masks," Opt. Commun. **115**, 327-334 (1995).

[63] E. Hecht, *Optics*. (Addison Wesley, 2002).

[64] J.M. Ziebath and M.D. McGehee, "Extracting Light from Polymer LEDs using stamped Bragg Gratings," Advanced Functional Materials **14** (5), 451-456 (2004).

[65] F. Fitrilawati, M. O. Tjia, S. Pfeiffer et al., "Planar waveguides of PPV derivatives: attenuation loss, third-harmonic generation and photostability," Optical Materials **21** (1-3), 511-519 (2003).

[66] J. M. Ziebarth and M. D. McGehee, "A theoretical and experimental investigation of light extraction from polymer light-emitting diodes," J. Appl. Phys. **97** (6) (2005).

[67] M.D. McGehee, "Semiconducting polymer distributed feedback lasers," Appl. Phys. Lett. **72** (13), 1536 (1998).

[68] R. Kashyap, *Fibre Bragg Gratings*. (Academic Press, 1999).

[69] T. Kavc, G.A. Turnbull, and I.D.W Samuel, "Index and Relief Gratings in Polymer Films for Organic Distributed Feedback Lasers," Chemistry of Materials **14** (10), 4178-4185 (2002).

[70] L. Rocha, V. Dumarcher, C. Denis et al., "Laser emission in periodically modulated polymer films," J. Appl. Phys. **89** (5), 3067-3069 (2001).

[71] A. Yariv, "Periodic structures for integrated optics," IEEE Journal of Quantum Electronics **13** (4), 233-253 (1977).

[72] S.C. Kitson, "The fabrication of submicron hexagonal arrays using multiple-exposure optical interferometry," IEEE Photonics Techology Letters **8** (12), 1662-1664 (1996).

[73] S. Morita and R. Wiesendanger, *Noncontact Atomic Force Microscopy*. (Springer-Verlag, 2002).

[74] NanoscienceInstruments; Nanoscience Instruments Inc., "http://www.nanoscience.com/education/AFM.html."

[75] G. Jones, W. R. Jackson, C. Choi et al., "Solvent Effects On Emission Yield And Lifetime For Coumarin Laser-Dyes - Requirements For A Rotatory Decay Mechanism," Journal Of Physical Chemistry **89** (2), 294-300 (1985).

[76] H. T. Lu and M. Yokoyama, "Plasma preparation on indium-tin-oxide anode surface for organic light emitting diodes," J. Cryst. Growth **260** (1-2), 186-190 (2004).

[77] *http://www.oe-chemicals.com/dictionary-N.html*.

[78] R. A. Marcus and N. Sutin, "Electron Transfers In Chemistry And Biology," Biochimica Et Biophysica Acta **811** (3), 265-322 (1985).

[79] J. Ridley and M. Zerner, "Intermediate Neglect Of Differential Overlap Technique For Spectroscopy - Pyrrole And Azines," Theoretica Chimica Acta **32** (2), 111-134 (1973).

[80] M. C. Zerner, G. H. Loew, R. F. Kirchner et al., "Intermediate Neglect Of Differential-Overlap Technique For Spectroscopy Of Transition-Metal Complexes - Ferrocene," Journal Of The American Chemical Society **102** (2), 589-599 (1980).

[81] J. P. Calbert, "Zoa v3.0," Service de Chimie Matériaux Nouveaux, Université de Mons-Hainaut, Mons (Belgium) - http://zoa.freeservers.com.

[82] S. Droge, M. S. Al Khalifah, M. O'Neill et al., "Grazing Incidence X-ray Diffraction of a Photoaligned Nematic Semiconductor," J. Phys. Chem. B **113** (1), 49-53 (2009).

[83] J. Cornil, D. Beljonne, D. A. dos Santos et al., "Intermolecular interactions in electroluminescent conjugated materials," Thin Solid Films **363** (1-2), 72-75 (2000).

[84] T. Huser and M. Yan, "Aggregation quenching in thin films of MEH-PPV studied by near-field scanning optical microscopy and spectroscopy," Synthetic Metals **116** (1-3), 333-337 (2001).

[85] R. Jakubiak, C. J. Collison, W. C. Wan et al., "Aggregation quenching of luminescence in electroluminescent conjugated polymers," J. Phys. Chem. A **103** (14), 2394-2398 (1999).

[86] J. Peet, N. S. Cho, S. K. Lee et al., "Transition from Solution to the Solid State in Polymer Solar Cells Cast from Mixed Solvents," Macromolecules **41** (22), 8655-8659 (2008).

[87] G. D. Scholes and G. Rumbles, "Excitons in nanoscale systems," Nat. Mater. **5** (9), 683-696 (2006).

[88] J.-H. Fuhrhop and C. Endisch, Molecular and Supramolecular Chemistry of Natural Products and Their Model Compounds. (CRC Press, 2000).

[89] V. Coropceanu, J. Cornil, D. A. da Silva et al., "Charge transport in organic semiconductors," Chemical Reviews **107** (4), 926-952 (2007).

[90] R. H. Friend, R. W. Gymer, A. B. Holmes et al., "Electroluminescence in conjugated polymers," Nature **397** (6715), 121-128 (1999).

[91] X. Gong, D. Moses, and A. J. Heeger, in *Organic Light-Emitting Materials And Devices Viii* (2004), Vol. 5519, pp. 82-88.

[92] B. W. D'Andrade and S. R. Forrest, "White organic light-emitting devices for solid-state lighting," Adv. Mater. **16** (18), 1585-1595 (2004).

[93] R. Lineback, in *Solid State Technol.* (2006), Vol. 49, pp. 36-+.

[94] Y. Hamada, T. Sano, H. Fujii et al., "White-Light-Emitting Material for Organic Electroluminescent Devices," Japanese Journal Of Applied Physics **35**, L1339-L1341 (1996).

[95] B. W. D'Andrade, R. J. Holmes, and S. R. Forrest, "Efficient organic electrophosphorescent white-light-emitting device with a triple doped emissive layer," Adv. Mater. **16** (7), 624-+ (2004).

[96] C. W. Ko and Y. T. Tao, "Bright white organic light-emitting diode," Appl. Phys. Lett. **79** (25), 4234-4236 (2001).

[97] B. W. D'Andrade, M. E. Thompson, and S. R. Forrest, "Controlling exciton diffusion in multilayer white phosphorescent organic light emitting devices," Adv. Mater. **14** (2), 147-+ (2002).

[98] C. H. Kim and J. Shinar, "Bright small molecular white organic light-emitting devices with two emission zones," Appl. Phys. Lett. **80** (12), 2201-2203 (2002).

[99] G. Gu, G. Parthasarathy, P. E. Burrows et al., "Transparent stacked organic light emitting devices. I. Design principles and transparent compound electrodes," J. Appl. Phys. **86** (8), 4067-4075 (1999).

[100] K. Müllen and U. Scherf, Organic light-emitting devices: Synthesis, properties, and applications. (John Wiley and Sons, 2006).

[101] S. A. Chen, K. R. Chuang, C. I. Chao et al., "White-light emission from electroluminescence diode with polyaniline as the emitting layer," Synth. Met. **82** (3), 207-210 (1996).

[102] S. Tasch, E. J. W. List, O. Ekstrom et al., "Efficient white light-emitting diodes realized with new processable blends of conjugated polymers," Appl. Phys. Lett. **71** (20), 2883-2885 (1997).

[103] M. Granstrom and O. Inganas, "White light emission from a polymer blend light emitting diode," Appl. Phys. Lett. **68** (2), 147-149 (1996).

[104] H. C. Lin, C. M. Tsai, J. T. Lin et al., "Novel red and white PLED devices consisting of PVK blended with blue-emitting fluorene derivatives and carbazole dopants," Synth. Met. **156** (18-20), 1155-1160 (2006).

[105] S. J. Bai, C. C. Wu, T. D. Dang et al., "Tunable and white light-emitting diodes of monolayer fluorinated benzoxazole graft copolymers," Appl. Phys. Lett. **84** (10), 1656-1658 (2004).

[106] S. Tokito, M. Suzuki, F. Sato et al., "High-efficiency phosphorescent polymer light-emitting devices," Org. Electron. **4** (2-3), 105-111 (2003).

[107] A. C. A. Chen, S. W. Culligan, Y. H. Geng et al., "Organic polarized light-emitting diodes via Forster energy transfer using monodisperse conjugated oligomers," Adv. Mater. **16** (9-10), 783-+ (2004).

[108] J. P. J. Markham, E. B. Namdas, T. D. Anthopoulos et al., "Tuning of emission color for blue dendrimer blend light-emitting diodes," Appl. Phys. Lett. **85** (9), 1463-1465 (2004).

[109] T. Nakayama and K Hiyama, 2008.

[110] A.N. Safonov, B. Matterson, J.M. Lupton et al., "Modification of polymer light emission by lateral microstructure," Synth. Met. **116**, 145-148 (2001).

[111] J.M. Lupton and I.D.W Samuel, "Bragg scattering from periodically microstructured light emitting diodes," Appl. Phys. Lett. **77** (21), 3340-3342 (2000).

[112] W. C. Tsoi, University of Hull, 2006.

[113] W. Staude, Laser-Strophometry: High-Resolution Techniques for Velocity Gradient Measurements in Fluid Flows, 1 ed. (Springer, Berlin, 2001).

[114] A. Othonos and K. Kalli, Fiber Bragg Gratings: Fundametals and Applications in Telecommunications and Sensing. (Artech House Inc., 1999).

[115] P.G. De Gennes and J. Prost, *The Physics of Liquid Crystals*. (Oxford University Press, 1993).

[116] Y. B. Boiko, V. S. Solovjev, S. Calixto et al., "Dry Photopolymer Films For Computer-Generated Infrared Radiation Focusing Elements," Appl. Optics **33** (5), 787-793 (1994).

[117] J. R. Lawrence, F. T. O'Neill, and J. T. Sheridan, "Photopolymer holographic recording material," Optik **112** (10), 449-463 (2001).

[118] J. Perelaer, K. Hermans, C. W. M. Bastiaansen et al., "Photo-embossed surface relief structures with an increased aspect ratios by addition of a reversible

addition-fragmentation chain transfer agent," Advanced Materials **20** (16), 3117-3121 (2008).

[119] B. M. I. van der Zande, J. Steenbakkers, J. Lub et al., "Mass transport phenomena during lithographic polymerization of nematic monomers monitored with interferometry," J. Appl. Phys. **97** (12) (2005).

[120] D. Y. Kim, S. K. Tripathy, L. Li et al., "Laser-Induced Holographic Surface-Relief Gratings On Nonlinear-Optical Polymer-Films," Appl. Phys. Lett. **66** (10), 1166-1168 (1995).

[121] P. Rochon, E. Batalla, and A. Natansohn, "Optically Induced Surface Gratings On Azoaromatic Polymer-Films," Appl. Phys. Lett. **66** (2), 136-138 (1995).

[122] T. Ubukata, T. Isoshima, and M. Hara, "Wavelength-programmable organic distributed-feedback laser based on a photoassisted polymer-migration system," Advanced Materials **17** (13), 1630-+ (2005).

[123] J.R. Lawrence, G.A. Turnbull, and I.D.W Samuel, "Optical properties of a light-emitting polymer directly patterned by soft lithography," Appl. Phys. Lett. **81** (11), 1955 (2002).

[124] P. Visconti, "Nanopatterning of organic and inorganic materials by holographic lithography and plasma etching," Microelectronic Engineering **53**, 391-394 (2000).

[125] G. Heliotis and I.D.W Samuel, "Blue, surface-emitting, distributed feedback polyfluorene lasers," Appl. Phys. Lett. **83** (11), 2118 (2003).